MODELING OF GASEOUS REACTING FLOW AND THERMAL ENVIRONMENT OF LIQUID ROCKET INJECTORS

by

Emre Sozer

A dissertation submitted in partial fulfillment
of the requirements for the degree of
Doctor of Philosophy
(Aerospace Engineering)
in The University of Michigan
2010

Doctoral Committee:

Professor Wei Shyy, Co-Chair
Assistant Professor Matthias Ihme, Co-Chair
Professor James F. Driscoll
Associate Professor Hong G. Im

To Meltem

ACKNOWLEDGEMENTS

I would like to thank my committee co-chairs Dr. Wei Shyy and Dr. Matthias Ihme, my committee members Dr. James Driscoll and Dr. Hong Im and my coworkers Ezeldin Hassan and Seokjun Yun for their invaluable support, guidance and contributions toward completion of this thesis.

In addition, I have benefited from collaboration with Dr. Siddharth Thakur and Dr. Jeff Wright of Streamline Numerics, Dr. Edward A. Luke of Mississippi State University, Mr. Kevin Tucker of NASA Marshall Space Flight Center, Dr. Corin Segal, Dr. Bruce Carroll and Dr. Jacob Chung of the University of Florida, Dr. Jack Hu and Dr. Guosong Lin of the University of Michigan.

This work was supported by the NASA Constellation University Institute Program (CUIP), Claudia Meyer and Jeff Rybak program managers.

TABLE OF CONTENTS

CHAPTER

LIST OF FIGURES

LIST OF TABLES

Table

LIST OF ABBREVIATIONS

BSL Baseline

CFD Computational Fluid Dynamics

CMC Conditional Moment Closure

CSEM Conserved Scalar Equilibrium Model

DNS Direct Numerical Simulation

DOE Design of Experiments

FCCD Face-centered Central Composite Design

FPV Flamelet/Progress Variable

GMRES Generalized Minimal Residual Method

LES Large Eddy Simulation

LFRC Laminar Finite-Rate Chemistry

LPRE Liquid Propellant Rocket Engine

LTE Local Thermodynamic Equilibrium

PDF Probability Density Function

PRS Polynomial Response Surface

RANS Reynolds/Favre averaged Navier-Stokes

REV Representative Elementary Volume

RMS Root Mean Square

RSM Response Surface Methodology

SLFM Steady Laminar Flamelet Model

SSME Space Shuttle Main Engine

SST Shear Stress Transport

TCI Turbulence-Chemistry Interactions

GLOSSARY

A : Cross-sectional area

A_{sf} : Solid-fluid interfacial area

C_E : Ergun coefficient

c_p : Specific heat

D : Diameter, *or* diffusivity

D_k : kth species mass diffusivity into mixture

D_t : Turbulent diffusivity

Da : Damköhler number

e : Specific internal energy

h : Specific enthalpy

H : Total specific enthalpy $\left(H = h + \frac{1}{2}u_i u_i = e + \frac{p}{\rho} + \frac{1}{2}u_i u_i\right)$

k : Turbulent kinetic energy

K : Permeability

k_b : Backward reaction rate

K_e : Equilibrium constant

k_f : Forward reaction rate

ℓ : Length scale

Le : Lewis number $\left(\frac{\lambda/c_p}{\rho D}\right)$

Le_t : Turbulent Lewis number $\left(\frac{\lambda_t/c_p}{\rho D_t}\right)$

M : Molecular weight

$\dot{m}$: Mass flow rate

n_i : Surface normal vector

NR : Number of reactions

NS : Number of species

p : Pressure

Pr : Prandtl number $\left(\frac{c_p\mu}{\lambda}\right)$

Pr_t : Turbulent Prandtl number $\left(\frac{c_p\mu_t}{\lambda_t}\right)$

q_i : Heat flux vector

R : Gas constant

R_{ij} : Reynolds stress tensor

Re_D : Reynolds number based on pore diameter

$Re_{\sqrt{K}}$: Reynolds number based on permeability

Sc : Schmidt number $\left(\frac{\mu}{\rho D}\right)$

Sc_t : Turbulent Schmidt number $\left(\frac{\mu}{\rho D_t}\right)$

t : Time

T : Temperature

T_{ij} : Stress tensor

T_w : Wall temperature

u : Velocity scale

u^+ : Inner scaled velocity $\left(\frac{u}{u_\tau}\right)$

u_D : Filter velocity

u_i : Velocity

u_τ : Shear velocity $\left(\sqrt{\frac{\tau_w}{\rho_w}}\right)$

x_i : Position vector

V : Volume

V_f : Volume of the fluid phase

$V_{k,j}$: Diffusion velocity vector of species k

y^+ : Inner scaled normal distance $\left(\frac{u_\tau y}{\nu_w}\right)$

Y_k : kth species mass fraction

Z : Mixture fraction

δ_{ij} : Kronecker delta

ε : Turbulent specific dissipation rate, *or* porosity

λ : Thermal conductivity

μ : Dynamic viscosity

μ_t : Eddy viscosity

ν : Kinematic viscosity

ν_t : Kinematic eddy viscosity

ρ : Density

τ : Time scale

τ_c : Convective time scale

τ_d : Diffusive time scale

τ_{ij} : Shear stress tensor

τ_w : Wall shear stress

χ : Scalar dissipation rate

ω : Turbulent specific dissipation rate per turbulent kinetic energy

Ω : Vorticity

$\dot{\omega}_k$: Mass production rate of species k

$\overline{(\quad)}$: Ensemble averaged quantity

$\widetilde{(\quad)}$: Ensemble averaged quantity

$(\quad)'$: Deviation from ensemble (or local volume) averaged quantity

$(\quad)''$: Deviation from Favre averaged quantity

$(\quad)_f$: Quantity for fluid phase

$(\quad)_s$: Quantity for solid phase

$(\quad)_{st}$: Quantity at stoichiometric conditions

$<\quad>$: Superficial volume averaged quantity

$< \quad >^f$: Intrinsic volume averaged quantity

ABSTRACT

MODELING OF GASEOUS REACTING FLOW AND THERMAL ENVIRONMENT OF LIQUID ROCKET INJECTORS

by

Emre Sozer

Co-Chairs: Wei Shyy and Matthias Ihme

Reacting flow and thermal fields around the injector critically affect the performance and life of liquid rocket engines. The performance gain by enhanced mixing is often countered by increased heat flux to the chamber wall, which can result in material failure. A CFD based design approach can aid in optimization of competing objectives by providing detailed flow field data and an ability to feasibly evaluate a large number of design configurations. To address issues related to the CFD analysis of such flows, various turbulence and combustion modeling aspects are assessed.

Laminar finite-rate chemistry and steady laminar flamelet combustion models are adopted to facilitate individual assessments of turbulence-chemistry interactions (TCI) and chemical non-equilibrium. Besides the experimental wall heat transfer information, assessments are aided by evaluations of time scales, grid sensitivity, wall treatments and kinetic schemes. Several multi-element injector configurations are considered to study element-to-element interactions. Under the conditions considered, chemical non-equilibrium effect is found to be unimportant. TCI is found to noticeably alter the flow and thermal fields near the injector and the flame surface. In the multi-element injector case, due to proximity of the outer row injector elements to the wall, wall heat flux distribution is also significantly affected by TCI. The near wall treatment is found to critically affect wall heat flux predictions. A zonal treatment, blending the low-Reynolds number model and the law-of-the-wall approach is shown to improve the accuracy significantly.

Porous materials such as Rigimesh are often used as the injector face plate of liquid rocket engines. A multi-scale model, which eliminates the empirical dependence of conventional analysis methods, is developed. The resulting model is tested using experimental information showing excellent agreement.

The model development and assessment presented for both injector flows and transport in porous materials will be valuable for advancement of computational tools aiding design and analysis of liquid rocket engine flows. Towards this end, further challenges such as the modeling of liquid propellants and the atomization process, detailed characterization of the Rigimesh material and more rigorous validation need to be addressed.

CHAPTER I

Introduction

In high thrust liquid propellant rocket engines such as the Space Shuttle Main Engine (SSME), the harsh thermal environment in the combustion chamber and the prolonged exposure of the engine components to these conditions hinder the reliability and re-usability of the engine. Traditional design practices for liquid rocket injectors are based on past experience, simplified analytical and empirical calculations, intuition and limited experimental data. The limited understanding of the flow field and thermal environment is liable to result in suboptimal designs with unexpected performance and reliability characteristics, driving up the design, operation and maintenance costs. With the advancements in modeling approaches over the past few decades and with the far greater availability of computational resources, Computational Fluid Dynamics (CFD) is promising to become a viable option for aiding the design process by offering extensive data and ease of evaluating alternative design choices. However, significant issues related to CFD analysis of such flows still exist, e.g. turbulence modeling, reduction of chemistry mechanisms, determination of reaction rate constants and modeling of turbulence-chemistry interactions.

In this chapter, brief background information on liquid rockets is provided. The motivations of the current work are then discussed and finally an outline of the following chapters is presented.

1.1 Background on Liquid Propellant Rocket Engines

A schematic of a typical Liquid Propellant Rocket Engine (LPRE) thrust chamber is shown in Figure 1.1. In an LPRE, pressurized propellants, such as O_2 and H_2 in the case of SSME, are injected into the combustion chamber where they are burned and subsequently expanded through the nozzle. The injector typically consists of multiple injector elements mounted on the face plate. The face plate itself may contribute to the injection via utilization of porous materials in which case, the propellants also provide active cooling of the plate. The role of the injector is to mix the propellants as fast and uniformly as possible while avoiding a destructive thermal environment for the combustion chamber walls. Fast mixing implies a shorther combustion chamber and hence more allowance for nozzle length for a more efficient expansion. LPRE's can be classified according to the method of pressurizing the propellants for injection. A brief introduction to common LPRE cycles and injector elements is provided in the following summary [1; 2].

In the simplest form of an LPRE, propellants are stored in pressurized tanks and fed directly into the combustion chamber. This pressure-fed engine has few components and hence it offers low cost [3] and good reliability [4]. However, for large scale applications, heavy propellant tanks needed to sustain the pressure render this setup impractical. Alternatively, turbo-pumps are used to achieve necessary injection pressures. Three common engine cycles are depicted in Figure 1.2.

In all three cycles, all or part of the fuel is first directed into the cooling channels surrounding the combustion chamber and the nozzle.

In the gas generator cycle, a portion of the fuel and the oxidizer is burned in a separate combustor to drive the turbine powering the propellant pumps. The fuel stream exiting the cooling channels is injected directly into the combustion chamber while the exhaust from the gas generator is dumped (open-cycle) after the turbine stage.

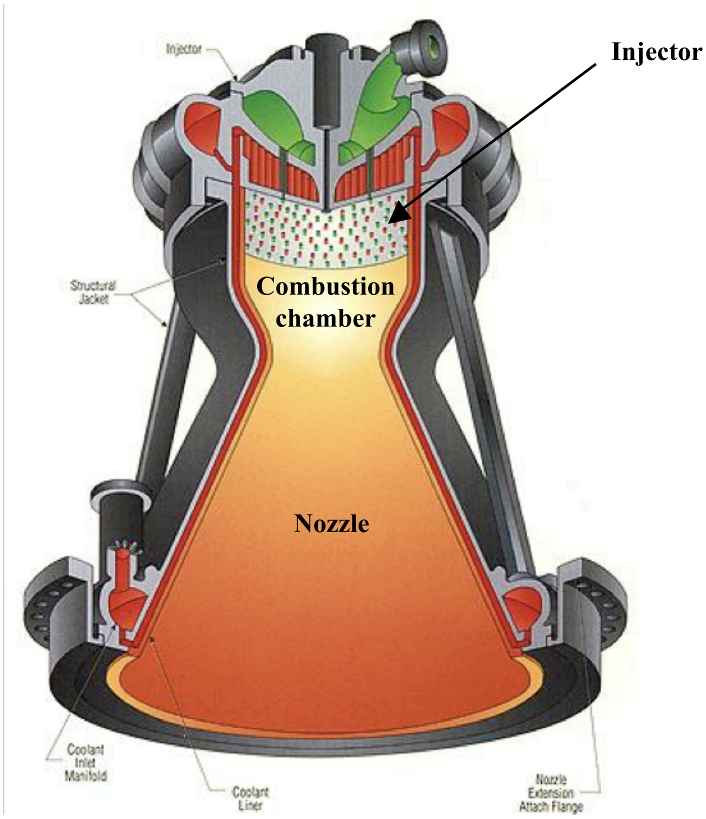

Figure 1.1: Liquid propellant rocket engine thrust chamber schematic. (Image source: www.engineeringatboeing.com)

The simplest of the turbo-pump engine cycles is the expander cycle which uses the heat that the fuel stream gains during cooling to drive the turbine. The elimination of the gas generator and, as a consequence, the lower temperature gases the turbine is exposed to, improves turbine reliability at the expense of limited turbine power [5; 6].

In the staged combustion cycle, all of the fuel, upon exiting the coolant ducts, is directed to a pre-burner. Only a portion of the oxidizer is fed into the pre-burner while the rest is directly injected into the main combustion chamber. As opposed to the gas generator, the hot, fuel rich exhaust from the pre-burner is used to drive the turbine and subsequently injected into the main chamber (closed-cycle).

In the SSME, as depicted in Figure 1.3, a variant of the staged combustion cycle is used. The SSME has two separate pre-burners powering two high pressure pumps for

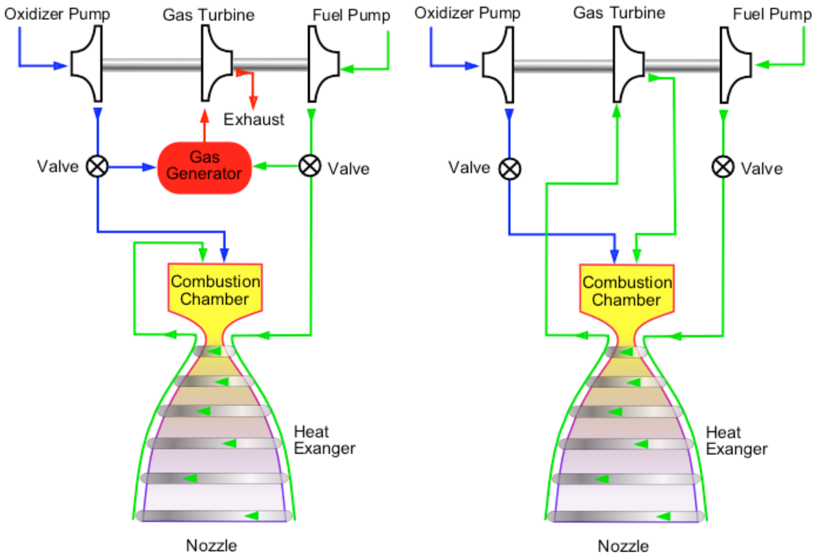

(a) Gas generator (b) Expander

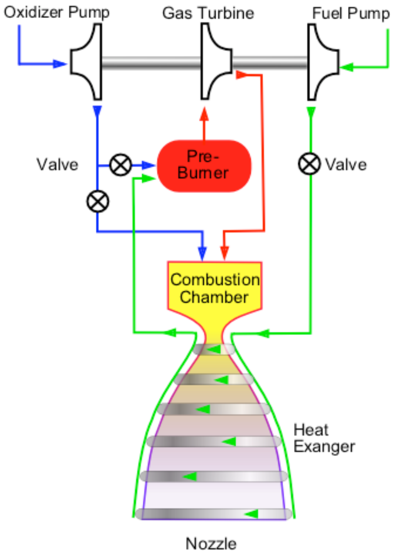

(c) Staged combustion

Figure 1.2: Liquid propellant rocket engine cycles. (Image source: www.wikipedia.com)

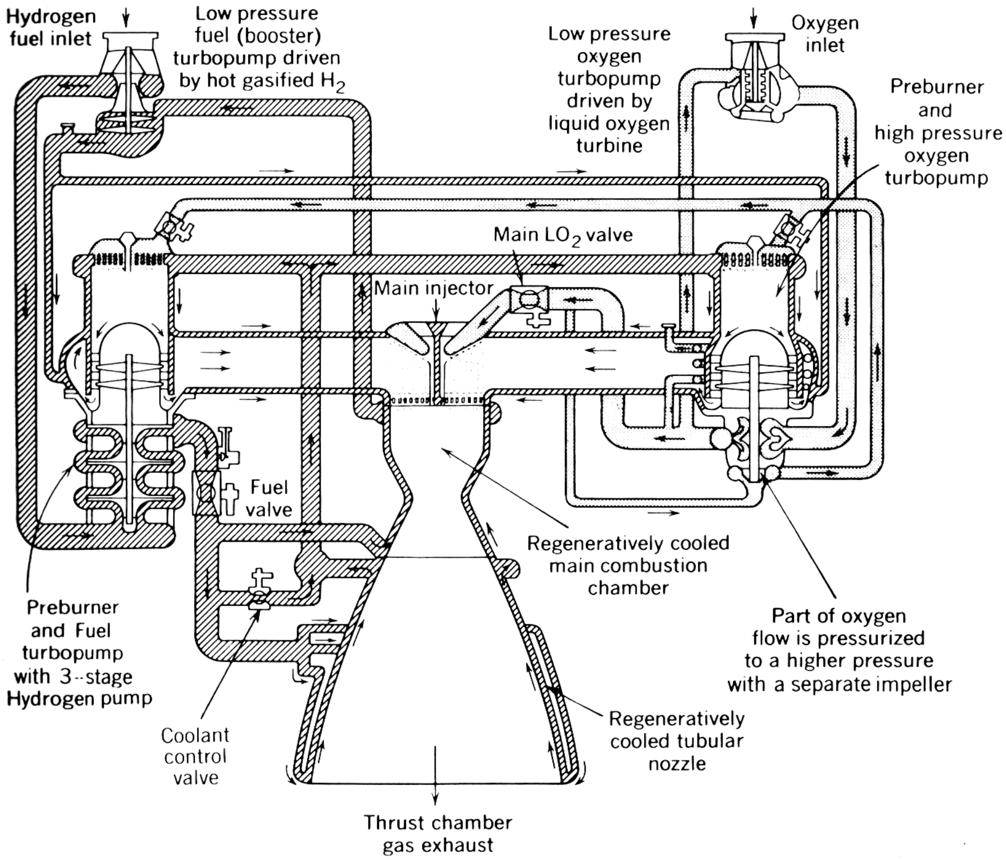

Figure 1.3: SSME flow diagram (from [7]).

the oxygen and the hydrogen. Initial version of the SSME main injector assembly is shown in Figure 1.4. Each of the 525 individual injector elements is of shear co-axial type, i.e., two concentric tubes with oxidizer fed through the center tube and fuel fed though the outer annulus. A dense metallic porous material called Rigimesh is used for the injector face plate through which a portion of the fuel is fed to aid in cooling.

1.2 Current and Past Injector Design Practices

Injector design is a key factor affecting the performance and robustness of the entire combustor [8; 9]. Examples of traditional approaches that are still widely used for injector design are briefly summarized in Table 1.1. Some of the relevant commentary of Gill [9] and the analytical tools and insight offered by Bittker [10] and

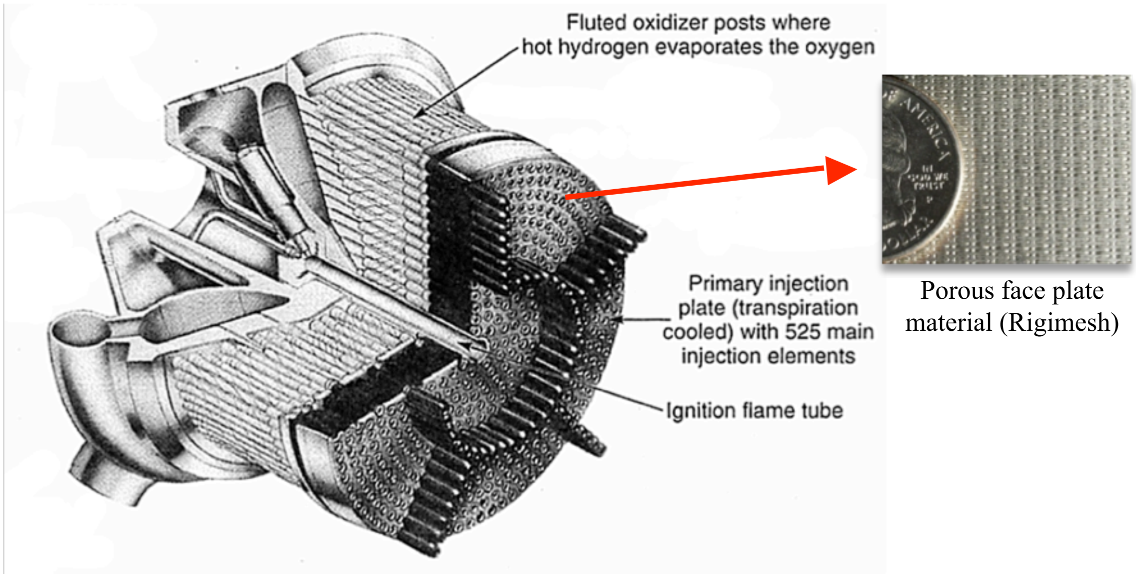

Figure 1.4: Main injector assembly of SSME (initial version, from [7]).

Priem and Heidmann [11] are expanded upon in more detail below.

Gill [9] compiles past experiences and provides general guidelines for the injector and combustion chamber design. He notes:

- Hardware durability is affected strongly by local mixture ratio near the injector face or chamber walls. Impingement of highly reactive propellants on the chamber wall can cause failure of the chamber due to the high rate of chemical reactions or erosion of the material.

- Propellant mixing, atomization and the mixture ratio of the propellants near the chamber walls are controlled by the injector element and its location and orientation on the injector face.

- Large variations in the mixture ratio occur within a spray produced by an element. Placement of elements and hence the inter-element mixing play an important role in determining the performance and material durability. The shear coaxial element produces most of its performance as a result of the individual element configuration and its performance is insensitive to inter-element

Table 1.1: Examples of traditional injector design approaches.

Reference	**Description**
Gill [9]	A comprehensive compilation of past experiences and general guidelines for the injector and combustion chamber design.
Bittker [10]	Simplified models in which one gaseous propellant diffuses from several point sources into a uniform stream of the second gaseous propellant. Combustion process effects were not considered (cold-flow analysis).
Priem and Heidmann [11]	1D steady state calculations assuming that droplet vaporization is the rate controlling step.
Pavli [12]	Experimental study of multi-element injectors with several different element types and heavy hydrocarbon fuels. The Priem-Heidmann vaporization model predictions are compared to the experiments and are found to be adequate except for injectors that were mixing limited.
Knuth et. al. [13]	Large number of subscale hot-firing experiments (over 300) to search for a premixing H_2/O_2 injector design that operates without flashback at high pressures.
Rupe [14]	Non-reacting spray properties of unlike impinging streams are used in design of multi-element injectors.
Burick [15]	A series of subscale single element cold-flow and hot-fire (reacting) experiments (using $FLOX/CH_4$ propellants) is used to design a multi-element injector through correlations for mixing and atomization characteristics.
Zinner et. al. [16]	Correlations are developed to apply cold-flow (water/air) test outcomes to hot-fire (reacting, LOX/H_2) cases.

placement. However, combustion chamber wall durability problems are usually corrected by altering the injector element arrangements.

- High combustion rates are desirable from a performance standpoint but they can produce high heat transfer rates to the wall and cause damage.
- A large portion of injector structural failures has been associated with the injector face. High temperature of the metal face in contact with the propellants considerably increases the likelihood of chemical attack.

Bittker [10] developed simplified cold-flow models in which one gaseous propellant diffuses from several point sources into a uniform stream of the second gaseous propellant. Estimations of the combustion chamber length required to mix propellants by turbulent and molecular gaseous diffusion were made. Boundary (wall) effects were neglected. Calculations showed that:

- Molecular diffusion is negligible next to turbulent mixing. Thus, the results were assumed independent of particular propellant combinations.
- Gaseous mixing is generally faster than spray evaporation. Thus, the former is not the limiting factor.

Priem and Heidmann [11] performed 1D steady state calculations assuming that droplet vaporization is the rate controlling step and that there is no interaction between droplets and no droplet shattering. They derived a generalized correlation for chamber length, length of nozzle convergent section, chamber contraction ratio, nozzle shape, chamber pressure, injection velocity, drop size and initial propellant temperature. Also a relation between propellant vaporized and combustor efficiency is derived. Combustor length requirements are found based on the correlations. Agreement of the model with experiments of oxygen, fluorine, ammonia and hydrocarbon fuels is demonstrated (e.g. see Figure 1.5). The combustor length required to vaporize a given percentage of propellant is found to increase with larger drop sizes and higher injection velocity. Note that while the Priem-Heidmann vaporization model offer predictions for injector performance, no information about combustion chamber wall or face plate thermal environments can be obtained. Furthermore, applicability of the model for new injector element designs or new propellants is questionable.

These relatively simple, analytical and empirical tools offer limited information about the detailed thermal environments of the injector and the combustion chamber, and their primary emphasis is on the performance (e.g. mixing and flame length) and stability characteristics. The lack of information and focus on the conditions that can reduce the combustor life can consequently drive up the initial development and maintenance costs. According to Tucker et al. [8], half of the SSME major combustion

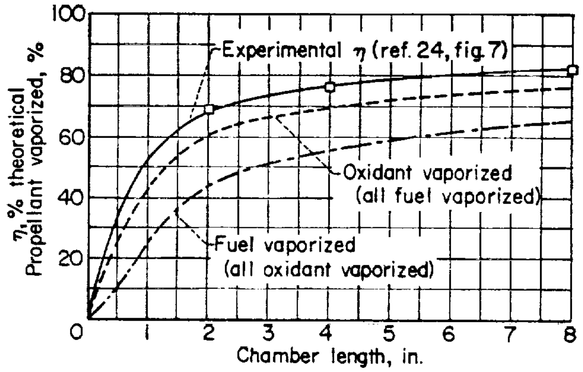

(a) Typical performance data for percentages of fuel and oxidant vaporized. Propellants, oxygen and JP-4; oxidant-fuel mass flow ratio, 2.2.

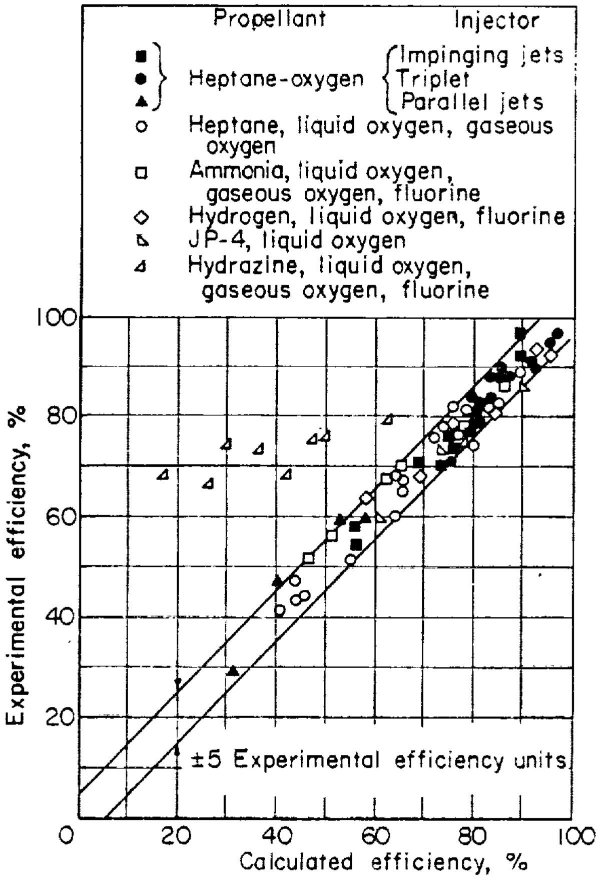

(b) Comparison of experimental and calculated efficiencies.

Figure 1.5: Example results from Priem and Heidmann [11].

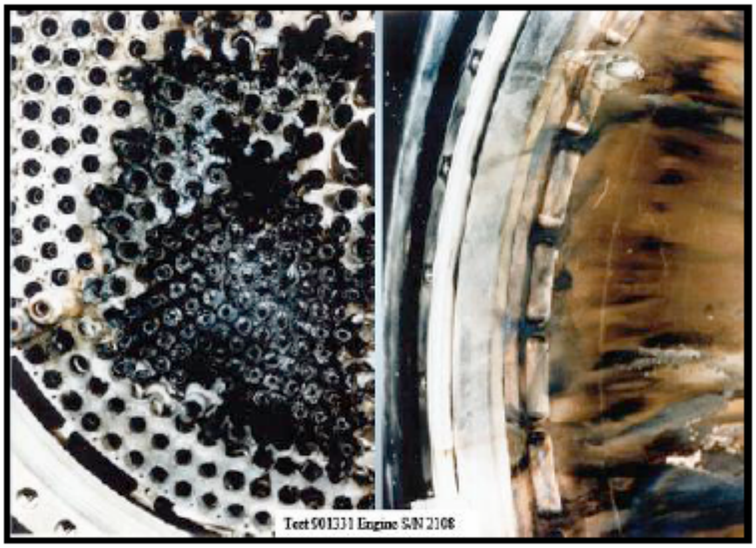

Figure 1.6: SSME main injector (left) and combustion chamber (right) damage (from [8]).

device failures occurred in the two year period following the first flight in 1981. And over 75% of the major failures occurred in either the main or pre-burner injectors. A typical failure from a 1981 engine test is shown in Figure 1.6. CFD predictions of the chamber wall and face plate thermal environments are central to the current study. New models and methodologies are proposed herein toward improving the prediction accuracy.

Computational Fluid Dynamics (CFD) can aid in the injector design process by enabling feasible evaluation of a large number of configurations and providing extensive multi-dimensional and transient data.

Vaidyanathan et al. [17] developed a CFD based design methodology for single element injectors utilizing Design of Experiments (DOE) techniques and Response Surface Methodology (RSM) [18]. The study was focused on the design/optimization methodology and it noted the need for rigorous validation of CFD models. Mack et al. [19] considered a model single element injector problem to assess the sensitivity of the peak chamber wall heat flux to variations in radial and circumferential element to element distances in the outer row of a multi-element injector.

1.3 Scope and Outline of the Thesis

Despite the demonstrated potential of a CFD based injector design approach, several criteria must be met to establish CFD as a viable design tool:

1. Fidelity and the geometrical complexity/resolution of the CFD model must yield sufficient representation of the physical phenomena affecting the combustor performance and reliability, such as the turbulent mixing, chemical reaction characteristics and combustor thermal environment.

2. CFD simulations must have a reasonable turn-around time to enable evaluation of a large number of design variations.

3. Accuracy of the simulations must be demonstrated and the regimes of applicability must be well understood through validation studies.

In order to contribute toward achievement of these goals, this study focuses on evaluating and improving the predictive capabilities of representative CFD modeling approaches via analysis of some of the key computational and modeling issues associated with flows surrounding single and multi-element injectors as well as their porous face plates. Specifically, issues including finite-rate kinetics and chemical non-equilibrium, turbulence-chemistry interactions, near wall turbulence treatment and numerical resolution are examined. Alternative combustion treatments, laminar finite-rate chemistry and steady laminar flamelet models, are adopted to facilitate the individual assessment of turbulence-chemistry interactions and chemical non-equilibrium through evaluation of multiple scenarios accounting for each effect. Near wall treatments including low Reynolds number and law-of-the-wall models are considered. For porous media flows, a multi-scale modeling framework is presented. Assessment is aided by available experimental wall heat transfer data as well as time scale evaluations, solution sensitivity to grid resolution, alternative wall treatments

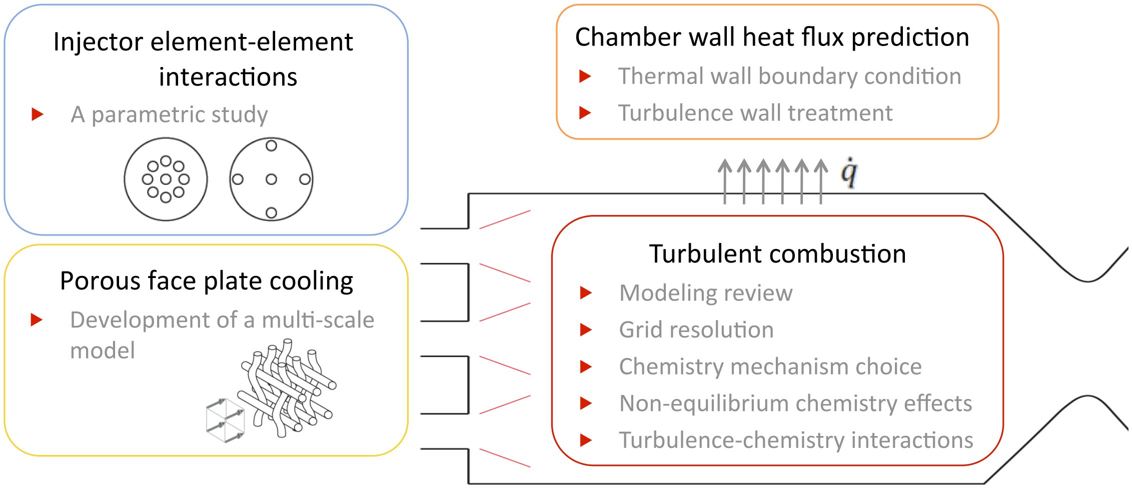

Figure 1.7: Schematic summary of the investigated topics.

and various kinetic schemes. A schematic summary of investigated topics is shown in Figure 1.7.

Two general purpose CFD codes, Loci-Chem [20; 21] and Loci-Stream [22; 23; 24], are used in this study. Both codes incorporate the laminar finite-rate chemistry model. The steady laminar flamelet model and the proposed porous media model are newly implemented in the Loci-Stream code.

In Chapter 2, existing non-premixed turbulent combustion modeling approaches are reviewed and their merits and limitations are discussed. Also, the numerical methods and codes utilized are described.

In Chapter 3, two different experimental H_2/O_2 single element injectors are analyzed with representative CFD models. Results are compared to the available experimental measurements. Sensitivity of the results to the following aspects are assessed:

- Physical phenomena such as chemical non-equilibrium and turbulence-chemistry interactions,
- Numerical choices such as grid resolution, wall thermal boundary conditions, alternative turbulence wall treatments and choice of the chemistry mechanism.

The turbulence wall treatment is identified to have a major impact on chamber wall heat flux prediction accuracy for the configuration investigated. A zonal treatment, blending the alternative wall treatments based on flow attachment to the wall, is proposed and demonstrated to improve the predictions significantly.

In Chapter 4, turbulence-chemistry interaction effect is further assessed for an experimentally characterized multi-element injector. Moreover, a parametric study for varying number of injector elements and element-to-element spacing is performed. The injector consists of a central element surrounded by a circular outer row of 6 elements. Injector configuration is parametrically altered to observe the effects of:

- Number of outer row injector elements,
- Radius of the outer row.

Corresponding changes in flame length and chamber wall temperature are discussed.

In the context of the multi-element injector problem, where only a small portion of the total heat generated by the reactions is lost through the chamber wall, a methodology for calculating the wall heat flux distribution as a post processing step to normally adiabatic-wall flamelet model (see Chapter 2) simulations is proposed.

In Chapter 5, a modeling technique for fluid flow and heat transfer through porous media is proposed. Current methodologies for prediction of such flows largely rely on experimentally determined characteristics often expressed in terms of two constants, namely permeability and Ergun coefficient, which are then considered constant properties for a specific material. In this study, a multi-scale methodology for empiricism-free prediction of fluid flow and heat transfer through porous media is developed. The method is devised with the motivation of simulating the fuel flow and heat transfer through a porous injector face plate (see Figure 1.4). The method is validated for an experimental setup of isothermal flow through a porous plate.

CHAPTER II

Non-premixed Turbulent Combustion Modeling

2.1 Governing Equations

2.1.1 Instantaneous Balance Equations

Instantaneous conservation equations for a chemically reacting mixture without body forces and external heating are given as [25]:

$$\frac{\partial \rho}{\partial t} + \frac{\partial \rho u_j}{\partial x_j} = 0 \tag{2.1}$$

$$\frac{\partial \rho u_i}{\partial t} + \frac{\partial \rho u_i u_j}{\partial x_j} = -\frac{\partial p}{\partial x_i} + \frac{\partial \tau_{ij}}{\partial x_j} \tag{2.2}$$

$$\frac{\partial \rho Y_k}{\partial t} + \frac{\partial \rho u_j Y_k}{\partial x_j} = -\frac{\partial}{\partial x_j}\left(\rho V_{k,j} Y_k\right) + \dot{\omega}_k \quad k = 1, \ldots, NS \tag{2.3}$$

$$\frac{\partial}{\partial t}\left(\rho H - p\right) + \frac{\partial}{\partial x_j}\left(\rho u_j H\right) = -\frac{\partial q_j}{\partial x_j} + \frac{\partial}{\partial x_j}\left(u_i \tau_{ij}\right) \tag{2.4}$$

For a Newtonian fluid, the viscous stress tensor is given by:

$$\tau_{ij} = \mu\left(\frac{\partial u_i}{\partial x_j} + \frac{\partial u_j}{\partial x_i}\right) - \frac{2}{3}\mu \frac{\partial u_k}{\partial x_k}\delta_{ij} \tag{2.5}$$

where the bulk viscosity is neglected. In Equation 2.3, the species diffusion velocities are given by Fick's Law as:

$$V_{k,j} Y_k = -D_k \frac{\partial Y_k}{\partial x_j} \tag{2.6}$$

Note that in Equation 2.4, the heat flux vector contains both the Fourier's Law component and the component due to the diffusion of species with different enthalpies:

$$q_j = -\lambda \frac{\partial T}{\partial x_j} + \rho \sum_{k=1}^{NS} h_k D_k \frac{\partial Y_k}{\partial x_j} \tag{2.7}$$

2.1.2 Equation of State

Assuming each species behaves as a thermally perfect gas, Dalton's law is used to determine the mixture pressure:

$$p = \sum_{k=1}^{NS} \rho_k R_k T \tag{2.8}$$

Note that an equation of state that supports thermally imperfect species such as cryogenic oxygen and hydrogen could be used. A general equation of state that has been widely used in combustion problems is developed by Hirshfelder et al. [26; 27].

Equation 2.8 relates mixture pressure to mixture temperature which is not readily available from the solution of the balance equations. Temperature is instead obtained via the internal energy of the mixture:

$$e = \sum_{k=1}^{NS} Y_k e_k \tag{2.9}$$

where the internal energy of each species is evaluated as:

$$e_k = \int_{T_{ref}}^{T} c_{p_k}(\tau) d\tau - R_k T \tag{2.10}$$

The species specific heats, c_{p_k}, are provided as 4^{th} order polynomials in terms of temperature. The polynomial coefficients can be obtained from references such as JANAF tables [28].

2.1.3 Transport Properties

For each species, transport properties (laminar viscosity, μ, thermal conductivity, λ, and species diffusivity, D) are obtained via CHEMKIN transport library [29] in the form of 4^{th} order polynomial fits as a function of temperature.

2.2 Favre Averaged Governing Equations

The instantaneous balance equations 2.1-2.7 govern both laminar and turbulent flow regimes. However turbulent flows exhibit flow structures covering a wide range of time and length scales [30]. Resolving all these scales numerically using Direct Numerical Simulation (DNS) remains extremely costly for virtually all engineering problems. However, for most engineering purposes, the main interest is the description of the mean flow field, which is the common aim of all turbulence models.

Favre Averaging

In the context of turbulent combustion, density fluctuations are significant. Each variable is decomposed into its density weighted ensemble average [31] and its instantaneous deviation from the averaged value as:

$$\phi = \widetilde{\phi} + \phi'', \quad \widetilde{\phi} = \frac{\overline{\rho\phi}}{\bar{\rho}}, \quad \widetilde{\phi''} = \frac{\overline{\rho\left(\phi - \widetilde{\phi}\right)}}{\bar{\rho}} = 0 \tag{2.11}$$

The balance equations are then derived for the mean quantities, $\widetilde{\phi}$, resulting in unclosed terms such as $\widetilde{u'\phi'}$. Closure of these terms is treated by the turbulence model. The end result is that only the mean flow field information is solved for and the local turbulent fluctuations are filtered out.

Mass Continuity

$$\frac{\partial \bar{\rho}}{\partial t} + \frac{\partial \bar{\rho}\widetilde{u}_j}{\partial x_j} = 0 \tag{2.12}$$

Momentum

$$\frac{\partial \bar{\rho}\widetilde{u}_i}{\partial t} + \frac{\partial \bar{\rho}\widetilde{u}_j\widetilde{u}_i}{\partial x_j} = -\frac{\partial \bar{p}}{\partial x_i} + \frac{\partial}{\partial x_j}\left(\widetilde{\tau}_{ij} - \overline{\rho u_i'' u_j''}\right) \tag{2.13}$$

The shear stress term for a Newtonian fluid is written as:

$$\widetilde{\tau}_{ij} = \mu\left(\frac{\partial \widetilde{u}_i}{\partial x_j} + \frac{\partial \widetilde{u}_j}{\partial x_i}\right) - \frac{2}{3}\mu\frac{\partial \widetilde{u}_k}{\partial x_k}\delta_{ij} \tag{2.14}$$

where fluctuations in the dynamic viscosity are neglected. The second order single point correlation in Equation 2.13 is called the Reynolds stress:

$$R_{ij} = -\overline{\rho u_i'' u_j''} \tag{2.15}$$

Boussinesq's eddy viscosity hypothesis, in analogy to molecular transport, relates the turbulent flux of momentum to mean velocity gradient and turbulent kinetic energy by introducing the eddy viscosity, μ_t, as:

$$R_{ij} = -\overline{\rho u_i'' u_j''} = \mu_t\left(\frac{\partial \widetilde{u}_i}{\partial x_j} + \frac{\partial \widetilde{u}_j}{\partial x_i}\right) - \frac{2}{3}\mu_t\frac{\partial \widetilde{u}_k}{\partial x_k}\delta_{ij} - \frac{2}{3}\bar{\rho}k\delta_{ij} \tag{2.16}$$

where k is the turbulent kinetic energy:

$$\bar{\rho}k = \frac{1}{2}\overline{\rho u_i'' u_i''} \tag{2.17}$$

While the molecular viscosity is a fluid property, the eddy viscosity (or turbulent viscosity) varies with the turbulent flow characteristics. On dimensional grounds, kinematic eddy viscosity is:

$$\nu_t = \frac{\mu_t}{\rho} = \ell \times u \tag{2.18}$$

where ℓ and u are the characteristic length and velocity scales of turbulent fluctuations. The role of the turbulence model is then to model these two scales.

Species Mass Fraction

$$\frac{\partial \bar{\rho}\widetilde{Y}_k}{\partial t} + \frac{\partial \bar{\rho}\widetilde{u}_j\widetilde{Y}_k}{\partial x_j} = -\frac{\partial}{\partial x_j}\left(\bar{\rho}\widetilde{V}_{k,j}\widetilde{Y}_k + \bar{\rho}\widetilde{u_j''Y_k''}\right) + \bar{\dot{\omega}}_k, \quad k = 1, \ldots, NS \tag{2.19}$$

The turbulent species flux is related to the first order moments via gradient transport hypothesis as:

$$-\bar{\rho}\widetilde{u_j''Y_k''} = \frac{\mu_t}{Sc_{t,k}}\frac{\partial \widetilde{Y}_k}{\partial x_j} \tag{2.20}$$

which, in combination with Equation 2.6, results in:

$$\frac{\partial \bar{\rho}\widetilde{Y}_k}{\partial t} + \frac{\partial \bar{\rho}\widetilde{u}_j\widetilde{Y}_k}{\partial x_j} = \frac{\partial}{\partial x_j}\left[\left(\frac{\mu}{Sc_k} + \frac{\mu_t}{Sc_{k,t}}\right)\frac{\partial \widetilde{Y}_k}{\partial x_j}\right] + \bar{\dot{\omega}}_k, \quad k = 1, \ldots, NS \tag{2.21}$$

Energy

$$\begin{aligned}
\frac{\partial}{\partial t}\left(\bar{\rho}\widetilde{H} - \bar{p}\right) + \frac{\partial}{\partial x_j}\left(\bar{\rho}\widetilde{u}_j\widetilde{H}\right) = {} & \\
& - \frac{\partial}{\partial x_j}\left(\widetilde{q}_j + \underbrace{\overline{\rho u_j'' h''}}_{1}\right) \\
& + \frac{\partial}{\partial x_j}\left[\widetilde{u}_j\left(\widetilde{\tau}_{ij} - \overline{\rho u_i'' u_j''}\right)\right] \\
& + \underbrace{\frac{\partial}{\partial x_j}\left[\overline{u_i''\tau_{ij}} - \overline{\rho u_j''\left(\frac{1}{2}u_i''u_i''\right)}\right]}_{2}
\end{aligned} \tag{2.22}$$

Here, the total mean enthalpy contains the turbulent kinetic energy.

$$\widetilde{H} = \widetilde{h} + \frac{1}{2}\widetilde{u}_i\widetilde{u}_i + k \tag{2.23}$$

In analogy to the molecular heat diffusion, term 1 in Equation 2.22 is modeled as:

$$\overline{\rho u_j'' h''} = \frac{\mu_t}{Pr_t}\frac{\partial \widetilde{h}}{\partial x_j} \tag{2.24}$$

Term 2 in Equation 2.22 is commonly modeled as [32]:

$$\overline{u_i'' \tau_{ij}''} - \overline{\rho u_j'' \left(\frac{1}{2}u_i'' u_i''\right)} = \left(\mu + \mu_t \sigma_k\right)\frac{\partial k}{\partial x_j} \tag{2.25}$$

where σ_k is a modeling constant.

Combining Equations 2.7, 2.14-2.17 and 2.23-2.25, the final form of the averaged energy equation becomes:

$$\begin{aligned}
\frac{\partial}{\partial t}\left(\bar{\rho}\widetilde{H} - \bar{p}\right) + \frac{\partial}{\partial x_j}\left(\bar{\rho}\widetilde{u}_j\widetilde{H}\right) = \qquad & \\
\frac{\partial}{\partial x_j}\left[\left(\frac{\mu}{Pr} + \frac{\mu_t}{Pr_t}\right)\frac{\partial \widetilde{h}}{\partial x_j}\right] & \\
+ \frac{\partial}{\partial x_j}\left(\rho \sum_{k=1}^{NS} \widetilde{h}_k D_k \frac{\partial \widetilde{Y}_k}{\partial x_j}\right) & \\
+ \frac{\partial}{\partial x_j}\left[\widetilde{u}_j\left(\mu + \mu_t\right)\left(\frac{\partial \widetilde{u}_i}{\partial x_j} + \frac{\partial \widetilde{u}_j}{\partial x_i} - \frac{2}{3}\frac{\partial \widetilde{u}_k}{\partial x_k}\delta_{ij}\right)\right] & \\
+ \frac{\partial}{\partial x_j}\left[\left(\mu + \mu_t \sigma_k\right)\frac{\partial k}{\partial x_j}\right] &
\end{aligned} \tag{2.26}$$

2.3 Turbulence Model

Since the instantaneous flow properties can be represented as the sum of a mean and a fluctuating part (Equation 2.11), the resulting governing equations contain fluctuation correlation terms that can't readily be evaluated with the knowledge of the mean quantities. Closure of these terms is accounted for by the turbulence model. Detailed description of the various approaches to turbulent closure is an exhaustive subject and can be explored elsewhere [30; 33; 34; 35]. Among the most popular methods are the Reynolds/Favre averaged Navier-Stokes (RANS) models and, to a less extent, the Large Eddy Simulation (LES) [36; 37; 38].

The RANS models are solved for the entire domain along with additional equations or relations to calculate the eddy viscosity [33]. The most widely used RANS models solve two transport equations; to provide information of the time and length scales, which are then linked to the eddy viscosity via dimensional assessment. Derivation of these equations and relations are aided by numerous scaling arguments and empirical observations. Strictly speaking, only the small turbulent scales in the inertial and Kolmogorov ranges can be assumed universal and the larger scales will depend on the problem geometry [30]. The LES models take advantage of this property of turbulent flows by attempting to numerically resolve the larger, geometry dependent scales while modeling the rest with sub-grid scale models (SGS). The SGS models in LES have the advantage of incorporating the information from the resolved scales and hence pose less or no empirical dependence. While LES methods offer increased accuracy in most cases, they also introduce a significant increase in computational cost compared to RANS models. The additional cost is due to the need for finer, 3D grids and a fine temporal resolution. Note that the coupling between the reactions and molecular mixing still occurs in scales not resolved in LES [39] and hence still needs modeling.

Due to the substantial computational cost of LES, RANS models remain widely used in turbulent reacting flow simulations. This is especially true in the context of CFD based design optimization studies where a large number of design choices need to be simulated.

Two most widely used RANS turbulence models are $k - \varepsilon$ [40] and $k - \omega$ [41], where k is the turbulent kinetic energy, ε is the dissipation rate and ω is defined as the dissipation rate per turbulent kinetic energy. The latter model offers improved accuracy near wall layers in the presence of adverse pressure gradients but displays strong sensitivity to free stream values [42]. Menter's Shear Stress Transport (SST) model [43] uses the $k - \omega$ model near solid walls and transitions to the $k - \varepsilon$ model away from the walls with the help of a blending function, hence combining the strengths of each model. SST also incorporates an empirical dampening function for the eddy viscosity near the walls to mimic the suppression of turbulence near the walls. Due to the demonstrated enhancements [43] offered by the model without any additional computational cost, SST was used in the current study. Details of the model are given below.

Kinematic Eddy Viscosity

In the $k - \varepsilon$ model [40], transport equations for the turbulent kinetic energy and its dissipation rate are solved. The turbulent length and velocity scales in Equation 2.18 are then related to k and ε as:

$$u = k^{1/2}, \quad \ell = C_\mu \frac{k^{3/2}}{\varepsilon} \tag{2.27}$$

where $C_\mu = 0.09$ is the dissipation constant. The dissipation rate is defined as:

$$\varepsilon = \nu \overline{\frac{\partial u_i'}{\partial x_j} \frac{\partial u_i'}{\partial x_j}} \tag{2.28}$$

The kinematic eddy viscosity is defined as:

$$\nu_t = C_\mu \frac{k^2}{\varepsilon} \tag{2.29}$$

In the $k-\omega$ model [41], instead of ε, a transport equation is solved for turbulent dissipation rate per kinetic energy defined as:

$$\omega = \frac{\varepsilon}{C_\mu k} \tag{2.30}$$

hence, the eddy viscosity becomes:

$$\nu_t = \frac{k}{\omega} \tag{2.31}$$

In Menter's SST model [43], ε equation in the $k-\varepsilon$ model is cast in terms of ω. The $k-\varepsilon$ and $k-\omega$ models are blended based on the nearest wall distance. The eddy viscosity in SST is expressed as:

$$\nu_t = \frac{a_1 k}{\max(a_1\omega, \Omega F_2)} \tag{2.32}$$

where Ω is the absolute value of vorticity, $a_1 = 0.31$ and the blending function, F_2 is given as:

$$F_2 = \tanh(arg_2^2) \tag{2.33}$$

$$arg_2 = \max(2\frac{\sqrt{k}}{0.09\omega y}, \frac{500\nu}{y^2\omega}) \tag{2.34}$$

where y is the normal distance to the nearest wall. Near the wall, turbulent fluctuations are locally damped and the turbulent Reynolds number, $k^2/\varepsilon\nu$, approaches zero. The SST model incorporates this effect by limiting the eddy viscosity near the wall via the empirically derived damping as shown in Equation 2.32.

Equations for the Turbulent Kinetic Energy and the Dissipation Rate

Exact equations for the turbulent kinetic energy, k, and its dissipation rate, ε or ω, can be derived [30] based on the instantaneous and averaged momentum equations, 2.2 and 2.13, and the definitions given in Equations 2.17, 2.28 and 2.30. However both introduce additional unclosed terms.

Utilizing the gradient transport hypothesis and a turbulent Prandtl number ($1/\sigma_k$), the diffusion term is modeled and the following form of the k equation is obtained:

$$\underbrace{\frac{\partial}{\partial t}(\rho k) + u_l \frac{\partial}{\partial x_l}(\rho k)}_{\text{convection}} = \underbrace{R_{ij}\frac{\partial u_i}{\partial x_j}}_{\text{production}} - \underbrace{C_\mu \rho \omega k}_{\text{dissipation}} + \underbrace{\frac{\partial}{\partial x_j}\left[(\mu + \mu_t \sigma_k)\frac{\partial k}{\partial x_j}\right]}_{\text{diffusion}} \tag{2.35}$$

where R_{ij} is given in Equation 2.15. The exact equation for ω (or ε), however, is not as useful a starting point since several other fluctuation correlations and higher order moments are introduced. Hence an entirely empirical form is used. In SST formulation, ω and ε modeled equations are combined into a common form with a blending function which ensures a smooth switch based on the distance to the wall:

$$\begin{aligned}\underbrace{\frac{\partial}{\partial t}(\rho\omega) + u_l \frac{\partial}{\partial x_l}(\rho\omega)}_{\text{convection}} = {} & \underbrace{\frac{\gamma}{\nu_t} R_{ij}\frac{\partial u_i}{\partial x_j}}_{\text{production}} \\ & - \underbrace{\beta \rho \omega^2}_{\textit{dissipation}} \\ & + \underbrace{\frac{\partial}{\partial x_j}\left[(\mu + \mu_t \sigma_\omega)\frac{\partial \omega}{\partial x_j}\right]}_{\text{diffusion}} \\ & + \underbrace{2(1 - F_1)\rho\sigma_{\omega 2}\frac{1}{\omega}\frac{\partial k}{\partial x_j}\frac{\partial \omega}{\partial x_j}}_{\text{cross-diffusion}}\end{aligned} \tag{2.36}$$

where

$$F_1 = \tanh(arg_1^4) \tag{2.37}$$

$$arg_1 = \min\left(\max(\frac{\sqrt{k}}{0.09\omega y}, \frac{500\nu}{y^2\omega}), \frac{4\rho\sigma_{\omega 2}k}{CD_{k\omega}y^2}\right)$$

$$CD_{k\omega} = \max\left(2\rho\sigma_{\omega 2}\frac{1}{\omega}\frac{\partial k}{\partial x_j}\frac{\partial \omega}{\partial x_j}, 10^{-20}\right)$$

Note that the cross-diffusion term in Equation 2.36 is the only difference, besides the model constants, between the $k-\varepsilon$ and the $k-\omega$ models. F_1 term blends the two equations based on the distance to the wall. At the wall, F_1 becomes unity and the cross-diffusion term vanishes and hence the pure $k-\omega$ model is used. The $k-\omega$ and $k-\varepsilon$ model constants [34; 35] are also blended as:

$$\phi = F_1\phi_{k\omega} + (1-F_1)\phi_{k\varepsilon} \tag{2.38}$$

where $\phi_{k\omega}$ are:

$$\sigma_{k1} = 0.85, \quad \sigma_{\omega 1} = 0.5, \quad \beta_1 = 0.075, \quad C_\mu = 0.09 \tag{2.39}$$

$$\kappa = 0.41, \quad \gamma_1 = \beta_1/C_\mu - \sigma_{\omega 1}\kappa^2/\sqrt{C_\mu}$$

and $\phi_{k\varepsilon}$ are:

$$\sigma_{k2} = 1.0, \quad \sigma_{\omega 2} = 0.856, \quad \beta_2 = 0.0828, \quad C_\mu = 0.09 \tag{2.40}$$

$$\kappa = 0.41, \quad \gamma_2 = \beta_2/C_\mu - \sigma_{\omega 2}\kappa^2/\sqrt{C_\mu}$$

2.3.1 Wall Treatment

A difficulty in turbulent flow simulations arises due to the steep mean velocity and temperature gradients near solid walls. Direct resolution of these gradients requires a boundary layer grid that is sufficiently fine at least in the normal direction. This, in turn, introduces an increased computational cost. Perhaps more important is the fact that the wall dampens the turbulent fluctuations and the Reynolds number locally, requiring that the turbulence model be revised. This requires a good handling of the local flow structures and is not a straightforward task. In the SST turbulence model, this phenomenon is handled by an empirical damping function which acts to limit the eddy viscosity based on the proximity to the wall and the value of absolute vorticity as shown in Equation 2.32.

In an alternative approach for the near wall treatment of turbulence, the velocity and the temperature for the first cell off the wall is imposed directly via empirically obtained algebraic boundary layer profiles, hence avoiding the resolution requirement. As demonstrated by Kestin and Richardson [44], boundary layer velocity measurements for many different wall bounded turbulent flows (e.g. pipe flow, channel flow, flow over a flat plate) collapse into a universal profile such as shown in Figure 2.1 with:

$$u^+ = \frac{u}{u_\tau} \tag{2.41}$$

$$y^+ = \frac{u_\tau y}{\nu_w} \tag{2.42}$$

where $u_\tau = \sqrt{\frac{\tau_w}{\rho_w}}$ is called the shear velocity and τ_w represents the wall shear stress. Note that y^+ can be seen as a local Reynolds number.

A well known law-of-the-wall function due to Spalding [45] proposes a unified expression that is valid for the viscous sublayer, the buffer layer and the log law layer as:

$$y^+ = u^+ + e^{-\kappa B}\left[e^{-\kappa u^+} - 1 - \kappa u^+ - \frac{(\kappa u^+)^2}{2} - \frac{(\kappa u^+)^3}{6}\right] \tag{2.43}$$

$$\kappa = 0.41, \quad B = 5.5 \tag{2.44}$$

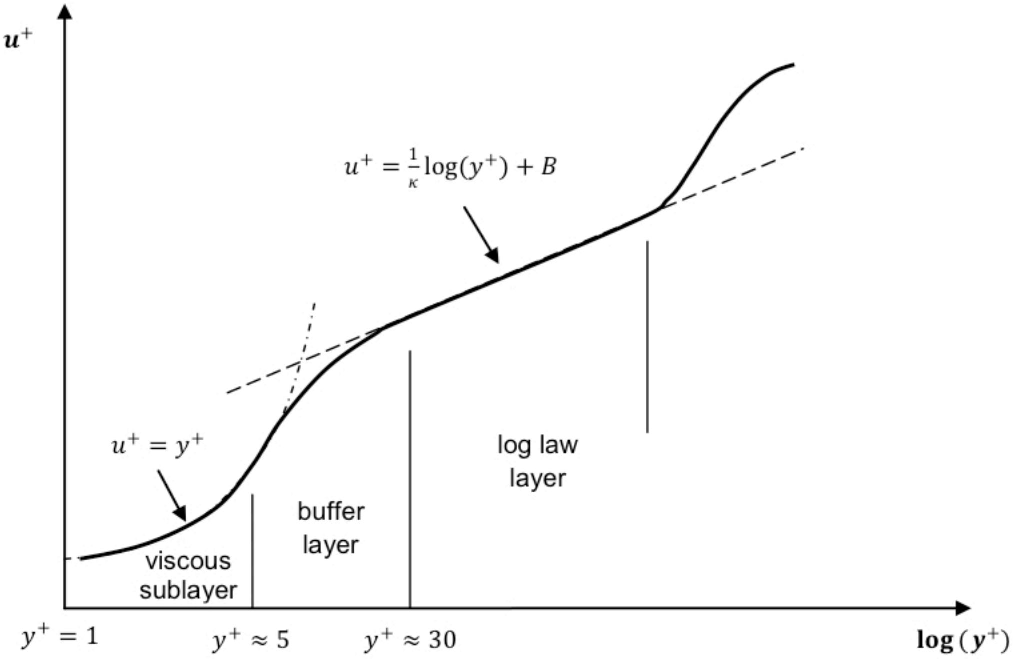

Figure 2.1: Turbulent velocity boundary layer profile schematic.

Nichols and Nelson [46] note that the term $e^{-\kappa B}e^{-\kappa u^+}$ is a restatement of the log law shown in Figure 2.1 and replace it with White and Christophs [47] outer velocity given as:

$$u^+ = \frac{1}{2\Gamma}\left[\beta + Q\sin\left(\Phi + \frac{\sqrt{\Gamma}}{\kappa}\ln\left(\frac{y^+}{y_0^+}\right)\right)\right] \tag{2.45}$$

where

$$\begin{aligned} &\Gamma = \frac{Pr_w^{1/3}u_\tau^2}{2C_pT_w}, \quad \beta = \frac{q_w\nu_w}{T_wk_wu_\tau} \\ &\Phi = \sin^{-1}\left(\frac{-\beta}{Q}\right), \quad Q = (\beta^2 + 4\Gamma)^{1/2}, \quad y_0^+ = e^{-\kappa B} \end{aligned} \tag{2.46}$$

Equation 2.43 is then rewritten [46] as:

$$y^+ = u^+ + y^+_{white} - e^{-\kappa B}\left[1 + \kappa u^+ + \frac{(\kappa u^+)^2}{2} + \frac{(\kappa u^+)^3}{6}\right] \tag{2.47}$$

$$y^+_{white} = \exp\left[\frac{\kappa}{\sqrt{\Gamma}}\left(\sin^{-1}\left(\frac{2\Gamma u^+ - \beta}{Q}\right) - \Phi\right)\right]\exp(-\kappa B) \tag{2.48}$$

Temperature distribution in the boundary layer is given as:

$$T = T_w \left(1 + \beta u^+ - \Gamma (u^+)^2\right) \tag{2.49}$$

The implementation details of this law-of-the-wall formulation as well as turbulence transport equations' boundary conditions are further detailed in Nichols and Nelson [46]. The empirical profiles used in the construction of the law-of-wall formulation are commonly based on a non-recirculating wall bounded flow structure. Therefore, their applicability to complex flow fields involving substantial flow curvatures, recirculation and pressure gradients is limited.

2.4 Chemistry Model

NR chemical reactions involving NS species can be written in general terms as:

$$\sum_{i=1}^{NS} \nu'_{i,r} A_i \rightleftharpoons \sum_{i=1}^{NS} \nu''_{i,r} A_i, \quad r = 1, \ldots, NR \tag{2.50}$$

The source term in Equation refeq:species can be expressed as:

$$\dot{\omega}_s = M_s \sum_{r=1}^{NR} (\nu''_{s,r} - \nu'_{s,r}) \times \left[k_{f,r} \prod_{l=1}^{NS} \left(\frac{\rho_l}{M_l}\right)^{\nu'_{l,r}} - k_{b,r} \prod_{l=1}^{NS} \left(\frac{\rho_l}{M_l}\right)^{\nu''_{l,r}} \right] \tag{2.51}$$

The forward reaction rates are determined with the Arrhenius relation:

$$k_{f,r} = C T^{\eta} e^{-\theta/T} \tag{2.52}$$

The backward reaction rates are determined using the equilibrium constant, $K_{e,r}$:

$$k_{b,r} = \frac{k_{f,r}}{K_{e,r}} \tag{2.53}$$

The equilibrium constant, $K_{e,r}$, is determined via minimization of Gibb's free energy as [48; 49]:

$$K_{e,r} = \left(\frac{p_{ref}}{R_s T}\right)^{\sum_{s=1}^{NS}(\nu''_{s,r}-\nu'_{s,r})} \exp\left[-\sum_{s=1}^{NS}\Omega_s(T)(\nu''_{s,r}-\nu'_{s,r})\right] \tag{2.54}$$

If the components of the species internal energy are assumed to be in thermodynamic equilibrium and a simple harmonic oscillator model is used for the vibrational mode [50], $\Omega_s(T)$ is given as:

$$\Omega_s(T) = 1 + n_s + \sum_{v=1}^{NVT_s} \ln\left(1 - e^{\frac{-\theta_{v,s}}{T}}\right) - (1-n_s)\ln T + \frac{h_{f,s}}{R_s T} - \frac{s_s^0}{R_s} \tag{2.55}$$

$$\begin{aligned} s_s^0 = {} & (s_{ref})_s - R_s(1+n_s)\ln(T_{ref}) - \\ & \sum_{v=1}^{NVT_s}\left(\frac{\theta_{v,s}}{\left(e^{\theta_{v,s}/T_{ref}}\right)T_{ref}}\ln\left(1 - e^{\theta_{v,s}/T_{ref}}\right)\right) \end{aligned} \tag{2.56}$$

where NVT_s are the number of vibrational modes, $\theta_{v,s}$ are the vibrational temperatures and s_{ref} are the entropy at reference temperature T_{ref} and pressure p_{ref}.

2.5 Turbulent Closure of Chemistry

A majority of practical combustion systems operate in the turbulent regime. Turbulence, in general, enhances the mixing of reactants and increases the reaction rate as illustrated by Lewis and Von Elbe [51] where a jet of fuel is injected into ambient air and the flame length is measured as a function of the Reynolds number (Re) based on the jet velocity and injector diameter. In the laminar regime, the flame length increases linearly with the Reynolds number whereas in the turbulent regime, it becomes independent of the Reynolds number, until a limit where flame lift-off occurs. Insensitivity of the flame length to increasing Re points to an enhanced reaction rate, i.e. as more fuel is introduced, more is consumed due to increased injector velocity and hence turbulence.

Accounting for the coupling between turbulence and the chemical reactions is one of the main difficulties in turbulent combustion modeling. The instantaneous form of the species source term is shown in Equation 2.51 whereas the mean values are needed for Equation 2.19.

Following the analysis of Poinsot and Veynante [25], consider a simple irreversible reaction:

$$A + B \rightarrow C \tag{2.57}$$

The rate of production of species A can be expressed as:

$$\dot{\omega}_A = -M_A C T^{\eta} Y_A Y_B e^{-\theta/T} \tag{2.58}$$

An expression for the mean reaction rate can be obtained using Taylor series expansion:

$$\exp\left(-\frac{\theta}{T}\right) = \exp\left(-\frac{\theta}{\widetilde{T}}\right)\left(1 + \sum_{n=1}^{+\infty} P_n \frac{T''^n}{\widetilde{T}^n}\right) \tag{2.59}$$

$$P_n = \sum_{k=1}^{n} (-1)^{n-k} \frac{(n-1)!}{(n-k)![(k-1)!]^2 k} \left(\frac{\theta}{\widetilde{T}}\right)^k \tag{2.60}$$

$$T^b = \widetilde{T}^b \left(1 + \sum_{n=1}^{+\infty} Q_n \frac{T''^n}{\widetilde{T}^n}\right), \quad Q_n = \frac{b(b+1)\cdots(b+n-1)}{n!} \tag{2.61}$$

$$\begin{aligned} \bar{\dot{\omega}}_A = -C\bar{\rho}^2 \widetilde{T}^{\eta} \widetilde{Y}_A \widetilde{Y}_B \exp\left(-\frac{\theta}{\widetilde{T}}\right) \times \\ \left[1 + \frac{\widetilde{Y''_A Y''_B}}{\widetilde{Y_A}\widetilde{Y_B}} + (P_1 + Q_1)\left(\frac{\widetilde{Y''_A T''}}{\widetilde{Y_A}\widetilde{T}} + \frac{\widetilde{Y''_B T''}}{\widetilde{Y_B}\widetilde{T}}\right)\right. \\ \left.(P_2 + Q_2 + P_1 Q_1)\left(\frac{\widetilde{Y''_A T''^2}}{\widetilde{Y_A}\widetilde{T}^2} + \frac{\widetilde{Y''_B T''^2}}{\widetilde{Y_B}\widetilde{T}^2}\right) + \cdots\right] \end{aligned} \tag{2.62}$$

Equation 2.62 introduces many new quantities to be closed. It is noted [52] that retaining only a few terms of the expansion may introduce large errors due to exponential dependence in temperature and hence a large number of moments need to be considered. Note that Equation 2.62 is derived only for a single step irreversible reaction. When a realistic multi-step chemistry mechanism is considered, this method quickly becomes intractable. Due to the complexity and the associated high computational cost, direct moment approaches are rarely used. Omission of all the fluctuation terms in Equation 2.62 and hence neglecting the effect of turbulence on reaction rates is adopted in the analysis presented in Chapters 3 and 4, and comparisons are provided with the results obtained via the Steady Laminar Flamelet Model (SLFM). The former approach is called the Laminar Finite-Rate Chemistry (LFRC) while the latter, as described in detail below, accounts for the turbulence-chemistry interactions via a presumed shape joint Probability Density Function (PDF).

With the direct moment closure approach ruled out due to its complexity, modeling efforts are mostly based on PDF description of turbulent statistics which can be achieved via;

- Solving a PDF transport equation,
- Presuming PDF shape.

The transported PDF models [53; 54; 55; 56; 57] rely on a derived transport equation of a joint PDF for reactive scalars and flow variables such as species mass fractions, velocity and gradients of these to achieve a closed form for the chemical source terms. However, each variable accounted via PDF introduces a new dimension to the transport equation, causing a high computational cost. In addition, the transport equation has unclosed terms and thus modeling of those is needed.

An attractive approach in terms of computational cost is to reduce the dimensionality of the problem by utilizing the concept of conserved scalars [58] which are convected and diffused by the fluid much like passive tracers. The statistics of the conserved scalar can be described with a PDF of presumed shape. For a conserved scalar such as mixture fraction, and its dissipation rate, this approach is shown to approximate the measured turbulent statistics satisfactorily [58; 25; 59; 60]. The mixture fraction as well as specific presumed PDF shapes adopted are explained in detail in the following text. With the utilization of conserved scalar/presumed PDF approach, the problem is transformed to the one of linking the conserved scalar to the reactive scalars such as the species mass fractions and temperature. This step is often associated with assumptions regarding the flame structure and chemistry speed and/or complexity. The focus of this review is restricted to RANS based non-premixed turbulent combustion models. An outlook into different venues for this context is provided in Table 2.1 along with brief descriptions and references for each modeling approach.

A spectrum of modeling approaches is available, ranging from greatest generality/accuracy and computational cost to the cheaper models restricted in generality and accuracy due to the simplifying assumptions.

At a basic level, an infinitely fast, global one-step reaction can be assumed. This mixed-and-burnt representation means that the flame is completely described by the mixing process. As proposed by Burke and Schuman [65] for a laminar cross-diffusion flame, reactive scalars are then piece-wise linear functions of a conserved scalar called the mixture fraction, denoted by Z. Turbulent closure can be achieved via a presumed shape PDF (typically β distribution [52]) defined by the mean mixture fraction and its mean variance both solved for via transport equations shown in the following section. A similar method can be used for multi-step equilibrium chemistry. The equilibrium state can be uniquely determined from the mixture fraction and minimization of Gibbs free-energy [32; 66]. Equilibrium assumption can be relaxed if, for a given chemistry mechanism, reactions that are relatively slow can be identified. In a system

Table 2.1: Modeling approaches for turbulent non-premixed flames.

<table>
<tr><td>No-model</td><td colspan="3"><i>Laminar finite-rate chemistry (LFRC)</i>:
The effect of turbulent fluctuations on reaction rates are simply ignored. (The fluctuation terms in Equation 2.62 are omitted). Averaged transport equations for each species mass fraction and the enthalpy are solved. Thus, complex, finite-rate reactions are handled but turbulence-chemistry interaction is not accounted for.</td></tr>
<tr><td>PDF Transport</td><td colspan="3">Based on a transport equation of a PDF for reactive scalars and velocity [53; 54; 55]. Many variations are proposed such as using a joint PDF of velocity, viscous dissipation and reactive scalars [56] or inclusion of gradients of velocity and the reactive scalars [57]. Unclosed terms appear in the PDF transport equation, requiring modeling. Otherwise exact description of the mean reaction rate is obtained. High dimensionality of the PDF equation is usually handled with Monte-Carlo methods.</td></tr>
<tr><td rowspan="4">Presumed PDF</td><td rowspan="3"></td><td rowspan="2"></td><td><i>One-step, infinitely fast reaction:</i>
A one-step, infinitely fast global reaction is assumed. Reaction zone is infinitely thin. Species mass fractions are piece-wise linear functions of mixture fraction $Y_i = Y_i(Z)$
Mean species mass fractions are obtained as:
$\widetilde{Y_i} = \int_0^1 Y_i(Z)P(Z)dZ$</td></tr>
<tr><td><i>Conserved Scalar Equilibrium Model (CSEM)</i>:
Solution of Z field provides elemental composition information. Via minimization of Gibbs free-energy, equilibrium state can be obtained [32].
Mean species mass fractions are obtained as:
$\widetilde{Y_i} = \int_0^1 Y_i(Z)P(Z)dZ$</td></tr>
<tr><td colspan="2"><i>Flamelet Model</i> [61; 62]:
Reaction zone is assumed to be thin compared to the smallest eddy size. Flame is seen as an ensemble of stretched laminar diffusion flames (flamelets). Species mass fractions are functions of the mixture fraction and the scalar dissipation rate: $Y_i = Y_i(Z, \chi)$
Mean species mass fractions are obtained as:
$\widetilde{Y_i} = \int_Z \int_\chi Y_i(Z, \chi)P(Z, \chi)d\chi dZ$</td></tr>
<tr><td colspan="3"><i>Conditional Moment Closure (CMC)</i> [63; 64]:
Solve for conditional means, $Y^C_{i,Z} = \overline{(Y_i|Z)}$, for M number of Z values. For N species, $N \times M$ balance equations are needed. Mean species mass fractions are obtained as: $\widetilde{Y_i} = \int_0^1 Y^C_{i,Z}P(Z)dZ$</td></tr>
<tr><td rowspan="2"></td><td></td><td>Fast Chemistry</td><td rowspan="2">Equilibrium Chemistry</td></tr>
<tr><td colspan="2">Non-equilibrium Chemistry</td></tr>
</table>

with S species, E elements and N_F fast reactions, E equations are provided by the mixture fraction and N_f equations are provided by the equilibrium condition of fast reactions. Then $S - E - N_f$ number of additional reaction progress variables are introduced. These variables are defined based on linear combinations of a pool of species concentrations so that the reaction source terms in their governing equations only involve rates of the slow reactions [67; 58; 68]. Then in these partial equilibrium models, a second transport equation governing the progress of a pool of intermediate species is solved.

On the other end of the spectrum (for presumed PDF methods), Conditional Moment Closure (CMC) method [63; 64] is a rigorous approach in which mean species mass fraction balance equations, conditioned at discrete values of the mixture fraction, are solved. This solution requires, for N species and M discrete values of Z, a solution of $M \times N$ number of transport equations. This is in addition to the two transport equations for the mean mixture fraction itself and its variance needed for determination of the PDF which then links the conditional averages of the reactive scalars to the Favre means. In CMC, no assumptions regarding the chemistry speed are made. However, it introduces significant computational cost.

In the following section, the basic concepts utilized in non-premixed turbulent combustion modeling are described. The simplifications in modeling brought forth by the conserved scalar approach and the assumptions of either equilibrium or fast chemistry are discussed.

Variations of most of the models mentioned here are available for premixed combustion problems and for LES sub-grid scale closure. For a comprehensive discussion, please see texts by Peters [52], Libby & Williams [69] and Poinsot & Veynante [25] or the review article by Veynante and Vervisch [70].

In the current study, steady state analysis of H_2/O_2 liquid propellant rocket engine injector performance and combustion chamber thermal environment is targeted. In addition, a parametric study of multi-element injector arrangements is conducted (Chapter 4) with the objective of understanding the impact of the injector arrangement on the combustion chamber wall thermal environment and mixing characteristics. The multi-element study, requiring many simulations corresponding to the domain of design choices, makes the numerical cost an important factor in the choice of the reaction closure model. As demonstrated in Chapter 3, high pressures/temperatures involved and the fast nature of H_2/O_2 chemistry warrant the assumption of fast chemistry. Taking advantage of this assumption, flamelet model allows tabulation of the laminar flamelet solutions parameterized by a conserved scalar and its dissipation rate. The species mass fraction transport equations, Equation 2.21, can be replaced by the transport equations for a single conserved scalar and its variance which is in turn used to determine the presumed PDF. Thus, the flamelet model offers significant savings in computational time while accounting for non-equilibrium chemistry effects and the effect of turbulence on reactions. The flamelet model is therefore chosen for the multi-element injector parametric study presented in Chapter 4. A detailed description of the flamelet models and the concepts utilized therein are provided in the following sections.

2.5.1 Concepts of Non-premixed Turbulent Combustion Modeling

Conserved Scalars and Mixture Fraction

A conserved scalar is a quantity that is unchanged by the chemical reactions. As a direct consequence, their balance equations do not involve chemical reaction source terms, and as such, the complexity of closing chemical source terms is avoided.

In a non-premixed flame, fuel and oxidizer are provided into the reactor in distinct streams of fixed composition. A normalized conserved scalar called the mixture fraction can be defined such that it takes the value of 0 in the oxidizer stream and 1 in the fuel stream. The precise definition of the mixture fraction is not unique. A review of the conserved scalar approaches can be found in Bilger [58] and various definitions of the mixture fraction are discussed by Peters [52]. A general way to define the mixture fraction is based on the elemental mass fractions which are unaltered by chemical reactions. Mass of element β can be written as:

$$m_\beta = \sum_\alpha \frac{n_{\alpha\beta} W_\beta}{W_\alpha} m_\alpha \tag{2.63}$$

with $n_{\alpha\beta}$ denoting the number of atoms of element β in molecule α, and W representing the molecular weight. Mass fraction of element β is then:

$$Z_\beta = \frac{m_\beta}{m} = \sum_\alpha \frac{n_{\alpha\beta} W_\beta}{W_\alpha} Y_\alpha \tag{2.64}$$

Combining Equations 2.3, 2.6 and 2.64, and assuming all species diffusivities to be equal, $D_\alpha = D$, a balance equation for the elemental mass fraction can be obtained as:

$$\frac{\partial \rho Z_\beta}{\partial t} + \frac{\partial \rho u_j Z_\beta}{\partial x_j} = \frac{\partial}{\partial x_j}\left(\rho D \frac{\partial Z_\beta}{\partial x_j}\right) \tag{2.65}$$

The elemental mass fraction can be normalized by defining the mixture fraction as:

$$Z = \frac{Z_\beta - Z_{\beta,O}}{Z_{\beta,F} - Z_{\beta,O}} \tag{2.66}$$

where F and O denote the fuel and oxidizer streams respectively. As a result, each elemental mass fraction balance equation and its boundary conditions become identical, yielding the mixture fraction balance equation:

$$\frac{\partial \rho Z}{\partial t} + \frac{\partial \rho u_j Z}{\partial x_j} = \frac{\partial}{\partial x_j}\left(\rho D \frac{\partial Z}{\partial x_j}\right) \tag{2.67}$$

The Favre averaged form of Equation 2.67 is:

$$\frac{\partial \bar{\rho}\widetilde{Z}}{\partial t} + \frac{\partial \bar{\rho}\widetilde{u}_j\widetilde{Z}}{\partial x_j} = \frac{\partial}{\partial x_j}\left(\bar{\rho}D\frac{\partial \widetilde{Z}}{\partial x_j} - \bar{\rho}\widetilde{u_j''Z''}\right) \tag{2.68}$$

The last term in Equation 2.68 is closed using the gradient transport theory:

$$-\bar{\rho}\widetilde{u_j''Z''} = \frac{\mu_t}{Sc_t}\frac{\partial \widetilde{Z}}{\partial x_j} \tag{2.69}$$

A key assumption in arriving at Equation 2.68 is the identical species molecular diffusivities. In turbulent diffusion flames with sufficiently large Reynolds numbers, turbulent fluxes dominate the molecular fluxes as discussed by Bilger [58]. It is common to neglect the molecular diffusion contribution in Equation 2.68 altogether.

A balance equation for the Favre variance of the mixture fraction, $\widetilde{Z''^2}$, can be derived [25] as:

$$\frac{\partial \bar{\rho}\widetilde{Z''^2}}{\partial t} + \frac{\partial \bar{\rho}\widetilde{u}_j\widetilde{Z''^2}}{\partial x_j} = \frac{\partial}{\partial x_j}\left(\frac{\mu_t}{Sc_t}\frac{\partial \widetilde{Z''^2}}{\partial x_j}\right) + 2\frac{\mu_t}{Sc_t}\frac{\partial \widetilde{Z}}{\partial x_j}\frac{\partial \widetilde{Z}}{\partial x_j} - 2\overline{\rho D\frac{\partial Z''}{\partial x_j}\frac{\partial Z''}{\partial x_j}} \tag{2.70}$$

Note that in derivation of Equation 2.70, turbulent transport term is closed via gradient transport theorem similarly to Equation 2.69. Also the molecular diffusion terms are neglected. The last term in Equation 2.70 is related to the turbulent dissipation of the mean mixture fraction variance and called as the scalar dissipation rate, χ:

$$\bar{\rho}\widetilde{\chi} = 2\overline{\rho D\frac{\partial Z''}{\partial x_j}\frac{\partial Z''}{\partial x_j}} \tag{2.71}$$

The conserved scalar mixture fraction has the distinct advantage of being unaltered by the chemical reactions. With the assumption of equal species molecular diffusivities, all the elemental conservation equations become identical and they can be represented by a single balance equation (Equation 2.67) free of reaction source terms. This is a great simplification considering the difficulty of a direct closure approach for the reaction source terms appearing in the species mass balance equations. As a result, the mixture fraction approach has been the corner stone of most of the modeling efforts which then focus on describing the turbulent statistics of the mixture fraction and linking the mixture fraction to the other non-conserved scalars such as species mass fractions and temperature. Some of the popular approaches to modeling will be reviewed in the following sections.

Scalar Dissipation Rate and Regimes in Non-Premixed Flames

An important concept in non-premixed combustion is the scalar dissipation rate defined as:

$$\chi = 2D\frac{\partial Z}{\partial x_j}\frac{\partial Z}{\partial x_j} \tag{2.72}$$

It has the dimension of $time^{-1}$ and can be thought of as the inverse of a characteristic diffusion time, a large χ meaning an enhanced mixing rate.

Regimes in non-premixed diffusion flames can be identified by considering the reactive/diffusive budget characterized by a Damköhler number defined as:

$$Da = \frac{\tau_d}{\tau_c} = (\tau_c \chi)^{-1} \tag{2.73}$$

where τ_d and τ_c are diffusive and chemical time scales respectively. While Equation 2.72 is for the instantaneous value of the scalar dissipation rate, the Favre averaged value is given in Equation 2.71 in which the $\widetilde{\chi}$ due to mean mixture fraction gradients are neglected against that due to fluctuation gradients.

In Figure 2.2, the upper branch of the S-shaped curve represents the combusting regime. Starting from the upper branch, if the diffusion time scale is decreased (e.g. by increasing flow rates), the Da reduces and the heat generated by reactions are diffused from the reaction zone faster until reactions can't keep up and the quenching

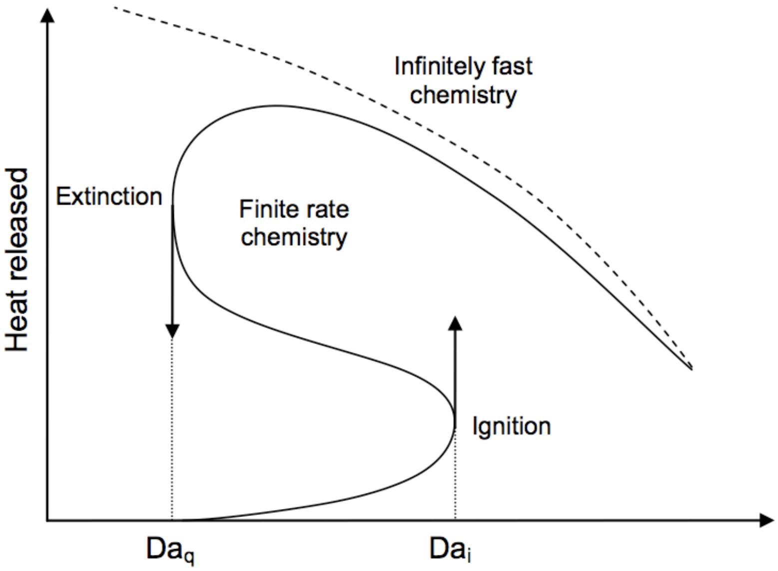

Figure 2.2: Generic response of the heat released by a 1-dimensional laminar diffusion flame. Da is based on χ_{st}. Reproduced from Veynante and Vervisch [70].

limit is reached. After quenching, a regime of pure mixing without combustion, represented by the lower branch of the curve, is attained. Starting from the lower branch, however, the same path is not followed when the Da is increased. Instead, the pure mixing regime exists until the ignition Da is reached. After ignition, a rapid transition to the upper branch follows.

If the chemistry is assumed to be infinitely fast in the analysis of such a flame, escape of heat from the reaction zone due to the fast diffusion compared to the chemistry speed, i.e. flame stretching, would not be captured. The infinitely fast chemistry approach then corresponds to the dashed line in Figure 2.2. In this approach, flame is completely described with the knowledge of mixing and hence the mixture fraction variable distribution.

On the other hand, if the flame is described by the mixture fraction variable and the scalar dissipation rate, finite-rate chemistry effects are recovered. However, whether the flame is extinct or ignited, corresponding to the lower or the upper branches of the curve depends on the path followed as discussed above. The progress variable methods, as discussed later in the context of extensions to the flamelet model, are proposed to remedy this problem.

In turbulent flow calculations, the mean scalar dissipation rate, $\widetilde{\chi}$, as shown in Equation 2.71, is an unclosed term appearing in the transport equation for the variance of the mixture fraction, Equation 2.70. It is modeled based on a turbulent time scale as:

$$\widetilde{\chi} = c_\chi \frac{\varepsilon}{k} \widetilde{Z''^2} \tag{2.74}$$

The time scale ratio is assumed to be a constant value of $c_\chi = 2$ as suggested by Janicka and Peters [71].

2.5.2 Steady Laminar Flamelet Model

In the flamelet models, a turbulent flame is viewed as an ensemble of thin laminar reactive-diffusive layers, flamelets, embedded in an otherwise turbulent non-reactive flow [52]. The flamelets are assumed to be thinner than the scale of a Kolmogorov eddy so that the effect of turbulence is limited to the deformation and stretching of the flame sheet but does not penetrate the reaction zone. The local reactive-diffusive balance in flamelets are viewed as similar to that of a laminar flame with the same Z and χ.

Flamelet equations can be derived [62] via a Crocco-type coordinate transformation of Equations 2.3 and 2.4. The original coordinate system is selected so that the x_2 and x_3 is locally aligned to the flame surface determined by the stoichiometric mixture fraction, $Z = Z_{st}$. Then x_1, which is normal to the stoichiometric surface, is replaced by Z.

$$(t, x_1, x_2, x_3) \rightarrow (\tau, Z, Z_1, Z_2) \tag{2.75}$$

where $\tau = t$, $Z = x_1$, $Z_2 = x_2$ and $Z_3 = x_3$. Transformation rules are given as:

$$\frac{\partial}{\partial t} = \frac{\partial}{\partial \tau} + \frac{\partial Z}{\partial t}\frac{\partial}{\partial Z} \tag{2.76}$$

$$\begin{aligned} \frac{\partial}{\partial x_1} &= \frac{\partial Z}{\partial x_1}\frac{\partial}{\partial Z} \\ \frac{\partial}{\partial x_j} &= \frac{\partial}{\partial Z_j} + \frac{\partial Z}{\partial x_j}\frac{\partial}{\partial Z} \quad (j = 2, 3) \end{aligned} \tag{2.77}$$

Assuming a unity Lewis number:

$$Le_i = \frac{\lambda / c_p}{\rho D} = 1 \tag{2.78}$$

and applying the transformation shown in Equation 2.76 to the instantaneous species mass balance and energy balance equations, Equations 2.3 and 2.4, the flamelet equations are reached as [62]:

$$\rho \frac{\partial Y_i}{\partial \tau} = \frac{1}{2}\rho\chi \frac{\partial^2 Y_i}{\partial Z^2} + \dot{\omega}_i - R(Y_i) \tag{2.79}$$

$$\rho \frac{\partial T}{\partial \tau} = \frac{1}{2}\rho\chi \frac{\partial^2 T}{\partial Z^2} - \sum_{i=1}^{n} \frac{h_i}{c_p}\dot{\omega}_i + \frac{1}{c_p}\frac{\partial p}{\partial \tau} - R(T) \tag{2.80}$$

with the operator R given as:

$$R = \sum_{j=2}^{3} \left[\rho u_j \frac{\partial}{\partial Z_j} - \frac{\partial(\rho D)}{\partial x_j}\frac{\partial}{\partial Z_j} - \rho D \left(2\frac{\partial Z}{\partial x_j}\frac{\partial^2}{\partial Z \partial Z_j} + \frac{\partial^2}{\partial Z_j} \right) \right] \tag{2.81}$$

Note that a low Mach number is assumed and hence the spatial pressure gradient as well as the viscous dissipation is neglected in Equation 2.4.

Peters [61] formally showed that the terms grouped in the R operator in Equations 2.79 and 2.80 are of higher order in ε which is a small quantity defined as the inverse of the non-dimensional activation energy. Hence they can be neglected. This translates into the assumption that the changes along the stoichiometric surface are small compared to the changes along the normal direction. Temporal derivatives are also omitted in the context of the steady flamelet models to arrive at:

$$\frac{1}{2}\rho\chi\frac{\partial^2 Y_i}{\partial Z^2}+\dot{\omega}_i=0 \tag{2.82}$$

$$\frac{1}{2}\rho\chi\frac{\partial^2 T}{\partial Z^2}-\sum_{i=1}^{n}\frac{h_i}{c_p}\dot{\omega}_i=0 \tag{2.83}$$

In Equations 2.82 and 2.83, the scalar dissipation rate appears as an external parameter. Peters [61] considered a 1D mixing layer problem to obtain the following analytical expression:

$$\chi(Z)=\chi_{st}\exp\left\{2\left([\mathrm{erfc}^{-1}(2Z_{st})]^2-[\mathrm{erfc}^{-1}(2Z)]^2\right)\right\} \tag{2.84}$$

With Equation 2.84, the flamelet equations (Equations 2.82 and 2.83) can be parameterized by χ_{st}. Then, the solution to those equations takes the functional form:

$$(Y_i,T)=f(Z,\chi_{st}) \tag{2.85}$$

Equation 2.85, computed with a complex chemistry, can be tabulated into a library as a pre-processing step to turbulent combustion computations. In turbulent flow calculations, the instantaneous thermo-chemical variables need to be linked to their mean values. This is achieved by convoluting the flamelet solutions with a PDF as:

$$\widetilde{Y_i}=\int\limits_{Z}\int\limits_{\chi}Y_i\widetilde{P}(Z,\chi_{st})d\chi_{st}dZ \tag{2.86}$$

where $\widetilde{P}$ is the density-weighed PDF:

$$\widetilde{P}(Z, \chi_{st}) = \frac{\rho(Z, \chi_{st})}{\bar{\rho}} P(Z, \chi_{st}) \tag{2.87}$$

Assuming statistical independence of χ and Z, the joint PDF in Equation 2.86 can be split [58; 72]:

$$\widetilde{P}(Z, \chi_{st}) = \frac{\rho(Z, \chi_{st})}{\bar{\rho}} P(Z) P(\chi_{st}) = \frac{\bar{\rho}}{\rho(Z, \chi_{st})} \widetilde{P}(Z) \widetilde{P}(\chi_{st}) \tag{2.88}$$

The β function for $P(Z)$ is widely adopted since its two parameters can be related to the first two moments:

$$P(Z) = \frac{Z^{\alpha-1}(1-Z)^{\beta-1}}{\int_0^1 Z^{(}\alpha - 1)(1-Z)^{\beta-1} dZ} \tag{2.89}$$

where

$$\alpha = \widetilde{Z} \left[\frac{\widetilde{Z}(1-\widetilde{Z})}{\widetilde{Z''^2}} - 1 \right] \tag{2.90}$$

$$\beta = (1-\widetilde{Z}) \left[\frac{\widetilde{Z}(1-\widetilde{Z})}{\widetilde{Z''^2}} - 1 \right]$$

$$\tag{2.91}$$

On the other hand, lognormal distribution for the $P(\chi_{st})$ is assumed. This assumption is tested and verified by several authors [59; 60]. The lognormal distribution for the scalar dissipation rate is given as:

$$P(\chi_{st}) = \frac{1}{\chi_{st}\sigma\sqrt{2\pi}} \exp\left[-\frac{1}{2\sigma^2} (\ln \chi_{st} - \mu)^2 \right] \tag{2.92}$$

with

$$\widetilde{\chi}_{st} = e^{\mu+\sigma^2/2} \tag{2.93}$$
$$\widetilde{\chi''^2_{st}} = \widetilde{\chi^2_{st}} \left(e^{\sigma^2} - 1\right)$$

The PDF of the scalar dissipation rate is known if the σ and the $\widetilde{\chi}_{st}$ are given. σ is often assumed unity [73] whereas $\widetilde{\chi}_{st}$ is obtained from Equation 2.74 using Equation 2.84.

An algorithm diagram for the steady laminar flamelet model is shown in Figure 2.3. Several extensions to the flamelet model are proposed in literature to relax the following key assumptions and limitations:

1. The differential diffusion effects are neglected, meaning that the molecular mass diffusivities of all the species are assumed the same and further they are equal to the thermal diffusivity ($Le_i = 1$).

2. Time dependent terms of the flamelet equations are omitted, yielding steady state flamelet solutions.

3. As discussed in the previous section, the flamelet equations, when solved and parameterized by χ_{st}, are not able to capture all the possible regimes of the flame. In Figure 2.2, the region between the extinction and ignition limits has multiple solutions corresponding to the non-combusting lower branch, combusting upper branch and the transient segment for a given value of the scalar dissipation rate. The steady laminar flamelet models employ a vertical projection to the upper branch.

4. The first assumption combined with the conserved scalar approach also results in species and energy conservation equations taking identical forms. Those can be combined into a single transport equation for mixture fraction if the

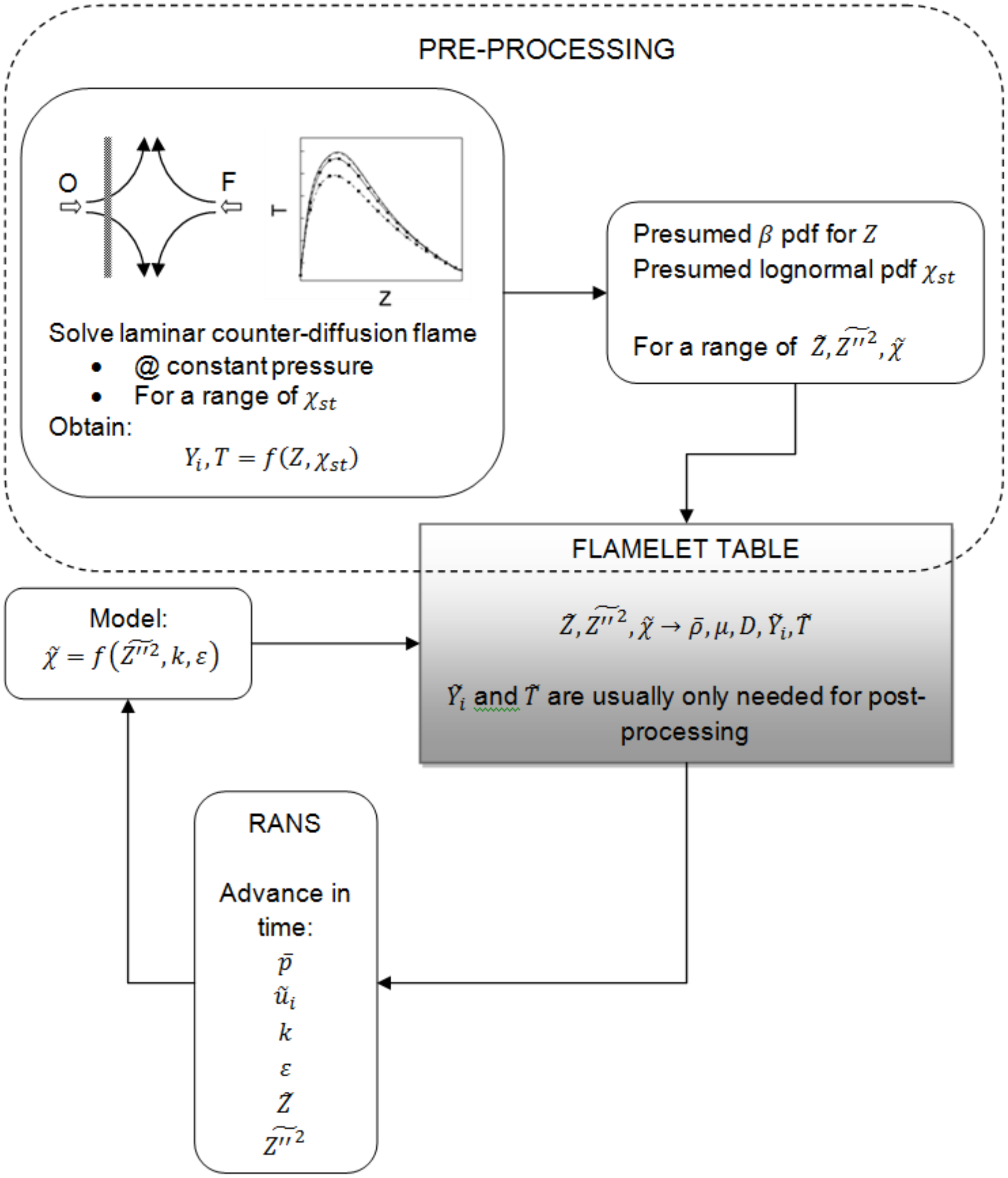

Figure 2.3: Algorithm diagram of the steady laminar flamelet model.

boundary conditions are also identical. This is true if there is no external heat addition or extraction such as heat transfer through the combustion chamber wall. As a consequence, the current model in the presented form is not able to incorporate wall heat transfer.

Pitsch and Peters [74] proposed a method to accommodate the differential diffusion effects exactly in the flamelet model. They define the mixture fraction as a scalar that satisfies the transport equation, Equation 2.67, i.e., the transport equation becomes the definition of Z. They then show that this Z can be linked to the original definition given in Equation 2.66. Flamelet equations are derived while no assumption is made regarding the diffusivities of species. They consider the counter-flow flames of hydrogen and n-heptane which have smaller and larger diffusivities compared to oxygen and nitrogen and demonstrate the effects of the differential diffusion. They conclude that a constant (but different) Le for each species is a reasonable assumption. In a subsequent work, Pitsch [75] investigated a turbulent $CH_4/H_2/N_2 - air$ diffusion flame and compared his results to experimental data. He concludes that the differential diffusion effects stem from the laminar region close to the nozzle and that the differential diffusion appears farther downstream as an unsteady effect. He reports that the predictions with differential diffusion effect considerations are improved close to the nozzle while a unity Le for all the species yields better results downstream in the fully turbulent region. Also suggested by Peters [52], a unity Le for all species is seen as an appropriate assumption for fully turbulent flames.

The limitation listed in item 3, i.e. the ambiguity of the steady laminar flamelet models regarding the state of the flame along the S-shaped curve (Figure 2.2), is remedied via the Flamelet/Progress Variable (FPV) approach as proposed by Pierce and Moin [76] and Ihme et al. [77]. In FPV models, a reaction progress variable is defined based on a combination of major product mass fractions or temperature. An additional transport equation for the progress variable is solved and the flamelets are parameterized with the progress variable.

In Steady Laminar Flamelet Models (SLFM), steady state flamelet solutions are parameterized with stoichiometric scalar dissipation rate, χ_{st}, meaning an inherent assumption that χ_{st} varies slowly. Regimes of validity of SLFM is investigated by Cuenot and Poinsot [78] who identified the limiting issues as flow unsteadiness, curvature and quenching of flamelets. Buriko et al. [79] utilized SLFM to study jet diffusion flames and compared their results to experimental measurements. They observed good predictions in the fast combusting region. However they note the importance of unsteady flamelet effects in the downstream post-flame region where scalar dissipation rate is small. This finding is supported by Pitsch et al. [74] who used an unsteady flamelet model formulation with a Lagrangian time to analyze a steady turbulent jet diffusion flame. Peters [62] retained the unsteady terms in his asymptotic derivation of the flamelet equations. Mauss et al. [80] introduced the Lagrangian time concept to account for unsteady flamelet effects within a steady simulation of a turbulent jet diffusion flame.

Extensions for the limitation in the list item 4 are proposed to account for the radiative heat losses [81; 82; 83]. In these models, an enthalpy defect is introduced as an additional dimension to the flamelet table. To match a given enthalpy defect, temperature boundary conditions for the steady laminar flamelets are altered. However, for large enthalpy defects, this may cause unrealistic boundary temperatures. In these cases, reduction of the mixture fraction range [82] or changing the mixture composition at the boundaries [83] for the flamelet solution is proposed.

For more than two decades, flamelet models have been used extensively (see Peters [52] for a comprehensive review) as they offer satisfactory predictive capabilities without excessive computational cost. Where the limitations of the model are observed, extensions and variations are devised, the rather small list of which is offered above. More recent studies of flamelet models are often incorporated within a LES framework [75; 84; 85; 86; 87; 88; 89].

In this study, the laminar finite-rate chemistry (LFRC) model and the steady laminar flamelet model (SLFM) are used to facilitate the study of single and multi-element injector flows (Chapters 3 and 4, respectively). The SLFM accounts for the Turbulence-Chemistry Interactions (TCI) as opposed to the LFRC model.

In the SLFM, effect of turbulent fluctuations on chemical reactions and material properties are represented with presumed shape PDF distributions. Thus, the TCI can effectively be disabled by using a Dirac-δ PDF. Chemical non-equilibrium effect, on the other hand, is represented by the scalar dissipation rate and can be turned off by taking $\chi \rightarrow 0$. Through this flexibility of the SLFM, the individual effects are quantitatively assessed for injector type problems.

Furthermore, a parametric study of a multi-element injector for varying element arrangements is performed in Chapter 4. The complex 3D geometry of the problem and the need to simulate many design scenarios make computational cost a primary concern. Due to high pressures (∼50 bars) and Reynolds numbers (e.g. $Re = 5 \times 10^6$ for the oxidizer stream based on the nozzle diameter) involved, and the fast nature of H_2/O_2 chemistry, SLFM seems well suited for current purposes.

The advantages and the disadvantages of the current SLFM and the LFRC model are summarized in Table 2.2

2.6 Numerical Methodology

Two different CFD codes are utilized in the current study, namely Loci-Chem [21] and Loci-Stream [22; 23; 24]. Both are based on a rule based programming framework called Loci [20]. Applications in Loci are written using a collection of rules each of which are implemented in the form of a C++ class. In addition, the user must create a database of facts which describe the particular knowns of the problem, such as boundary conditions. Once the rules and the facts are provided, a query is made to have the system construct a solution. A salient feature of Loci is its ability to automatically determine the scheduling of events in order to produce the answer to the desired query, as well as to test the consistency of the inputs to determine whether a solution is possible. Another major advantage of Loci is its automatic handling of domain decomposition and distribution of the problem to multiple processors.

Both Loci-Chem and Loci-Stream are finite volume codes that can operate on

Table 2.2: Comparison of the steady laminar flamelet and the laminar finite-rate chemistry models.

Laminar Finite-Rate Chemistry (LFRC)	**Steady Laminar Flamelet Model (SLFM)**
Advantages: • General formulation • Chemistry speed not restricted • Wall heat transfer is accounted for • Compressibility is accounted for • Differential diffusion is accounted for	Advantages: • Turbulence-chemistry interaction is accounted for • Lower computational cost compared to LFRC
Disadvantages: • Lack of turbulence-chemistry interactions • Higher computational cost compared to SLFM	Disadvantages*: • Limited to fast chemistry • Adiabatic walls assumed • Le=1 is assumed for all species • Flamelets are generated at constant pressure, hence compressibility effect is disregarded

* While the disadvantages of the LFRC are strict, those of the SLFM are for the currently used form and can be overcome as mentioned in Section 2.5.2.

unstructured grids of mixed element types. They employ different approaches for the integration of the equations. Before detailing the differences in their approaches, the common scheme for the evaluation of the gradients at cell centers and face centers leading to second order accurate convective and diffusive fluxes are described here. For a more comprehensive background on finite volume and unstructured grid methods, please see the text by Blazek [90].

All the flow variables are stored at cell centers (collocated arrangement). Variations of the primitive variables within cells are reconstructed as a piece-wise linear function:

$$\phi^R_{c0}(\overrightarrow{x}) + \nabla\phi_{c0} \cdot (\overrightarrow{x} - \overrightarrow{x}_{c0}) + \mathcal{O}\left((\overrightarrow{x} - \overrightarrow{x}_{c0})^2\right) \tag{2.94}$$

where ϕ is any primitive variable (see Figure 2.4 for notation). The gradient at cell center c_0 is obtained via minimizing the weighted error (via least squares) between

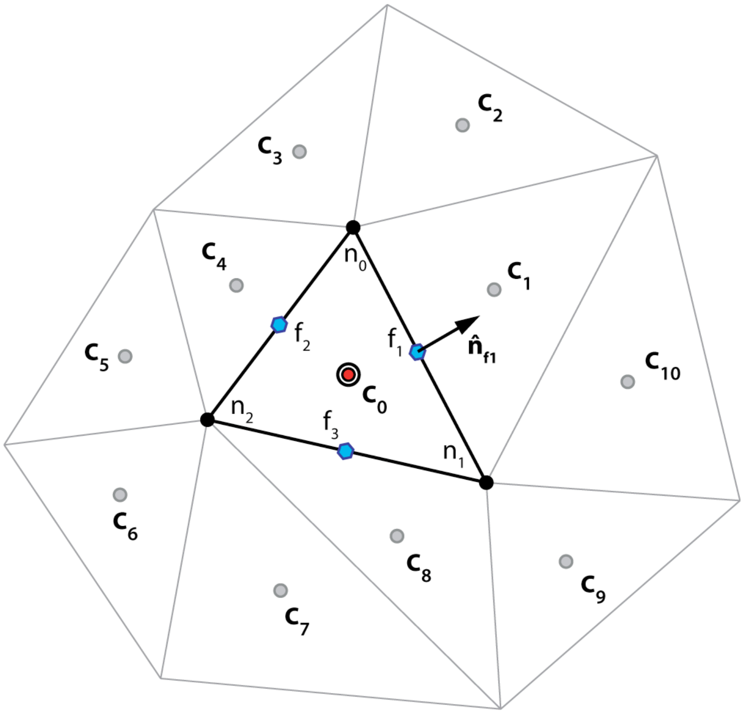

Figure 2.4: Cell-neighbor notation in an unstructured grid.

the reconstruction and the face sharing neighbor cell center values:

$$error = \sqrt{\sum_f \left(A_f \left(\phi^R_{c_0}(\overrightarrow{x}_{nbr}) - \phi_{nbr}\right)\right)^2} \tag{2.95}$$

where nbr denotes the face sharing neighbor cell index and A_f is the area of the face.

In the presence of discontinuities, Equation 2.94 is apt to produce non-physical overshoots. Hence the reconstruction is limited as:

$$\phi^R_{c_0}(\overrightarrow{x}) + \Psi_{c_0} \nabla \phi_{c_0} \cdot (\overrightarrow{x} - \overrightarrow{x}_{c_0}) \tag{2.96}$$

where Ψ_{c_0} is the limiter function. In the current study, the limiter proposed by Venkatakrishnan [91] is used.

For the evaluation of the diffusive fluxes, gradients at the face centers are needed. These are obtained via volume weighted averaging of the neighboring cell centered gradients; $\nabla\phi_{avg}$, and the component of the gradient along face normal direction is replaced by the more accurate direct finite differencing. An example for face f_1 (Figure 2.4) is:

$$\nabla\phi_{f_1} = \nabla\phi_{avg} - (\nabla\phi_{avg} \cdot \hat{n}_{f_1})\hat{n}_{f_1} + \frac{\phi_{c_1} - \phi_{c_0}}{(\overrightarrow{x}_{c_1} - \overrightarrow{x}_{c_0}) \cdot \hat{n}_{f_1}}\hat{n}_{f_1} \tag{2.97}$$

2.6.1 Loci-Chem

The density-based code Loci-Chem [21] solves for each flow variable, $\rho_1, \cdots, \rho_{NS}, u_i, E, k, \omega$, in a fully coupled manner with implicit 1^{st} or 2^{nd} order time integration. Generalized Minimal Residual Method (GMRES) algorithm with Jacobi preconditioning is used for the solution of the linear system. Pressure is obtained via the equation of state. Construction of cell variables on either side of a face is achieved via Equation 2.96. An approximate Riemann solution for these initial left and right states is obtained via the well known Roe scheme, extended for reacting flows [92]. HLLE [93] scheme is used locally near regions close to strong shocks. SST turbulence model and the wall treatment described in Section 2.3 along with the laminar finite-rate chemistry model (Table 2.1) is used in Loci-Chem. Note that the density-based solvers suffer from lost accuracy and convergence at the low Mach number limit where density ultimately does not vary with pressure and the equation of state is rendered stiff. Although these can be somewhat remedied by the use of preconditioning methods (which artificially alter the speed of sound to improve the system condition number) and modifications to convective flux evaluations (so as to scale numerical dissipation properly for decreasing Mach numbers), the pressure-based methods are fundamentally more suitable for low Mach number or incompressible flows.

2.6.2 Loci-Stream

The pressure-based code Loci-Stream [22; 24] is based on the SIMPLE (Semi-Implicit Method for Pressure-Linked Equations) algorithm [94] adopted for all speed flows [22; 95; 96]. It uses a finite volume approach with a collocated arrangement for the velocity components and the scalar variables like pressure.

Convective fluxes are evaluated with a second order upwind type scheme [97] where the interface fluxes are calculated based on the state on either left or right side of the interface depending on the sign of the interfacial mass flux. For a collocated arrangement of pressure and velocity components, a simple averaging of the nodal velocities to obtain the interface velocity leads to the well known checker-boarding problem. To avoid this, a dissipation term similar to Rhie-Chow momentum interpolation [98] is introduced while computing the mass flux.

The velocity components are computed from the respective momentum equations. The velocity and the pressure fields are corrected using a pressure correction equation. The correction procedure leads to a mass continuity satisfying velocity field. The species transport, energy and turbulence equations are also solved using the corrected velocity and pressure fields. The whole process is repeated until the desired convergence is reached [22; 94] and consequently, the time level is advanced. Pressure equations are solved with a GMRES algorithm with ILU preconditioning while symmetric Gauss-Seidel method is used for the momentum, species mass fraction, energy and turbulence equations.

In the flamelet model, the individual flamelets are pre-calculated and tabulated for a given pressure. In the flow solver, density is not calculated but read from the flamelet table. Thus the variations of pressure in the flow field do not affect the density. An incompressible solver is better suited for the current flamelet model implementation. Hence the flamelet model is only implemented in the Loci-Stream code.

CHAPTER III

Single Element Injector Simulations and Sensitivity Assessment

One of the major challenges facing liquid propellant rocket engines is the harsh thermal environment in the combustion chamber. A key goal of the liquid rocket injector design process is to minimize the combustion length, which requires faster mixing and burning of fuel and oxidizer. However, the extent to which the combustion length can be reduced is limited by the increased local heat transfer to the chamber wall resulting in possible material burn-out and crack. Various injector design approaches provide compromises between these two competing objectives. Before one can satisfactorily handle competing goals, adequate tools capable of predicting the reacting flow field and thermal environment under the injector operating conditions need to be available. To date, significant issues related to the CFD analysis of such flows exist, e.g. turbulence modeling, reduction of chemistry mechanism and determination of reaction rate constants, modeling of turbulence-chemistry interactions. There is a community-wide effort toward developing, evaluating, and refining CFD tools for these types of problems. This chapter summarizes our efforts on evaluating and improving the predictive capabilities of representative CFD modeling approaches for liquid rocket injector flows through systematic assessment of various model aspects.

A liquid propellant rocket engine injector commonly consists of multiple injector elements arranged in a specific pattern. While the arrangement of individual injector elements and their interactions play an important role in flow field characteristics, analysis of a combustor with a single injector element can offer valuable insight into individual element performance. Due to its simpler geometric configuration, the single element injector analysis provides a useful benchmark case to develop an understanding of the underlying physics such as turbulent mixing, chemical reactions and their interactions, as well as to validate and improve the CFD modeling efforts pertaining therein.

Table 3.1 summarizes selected studies based on computational modeling of single element H_2/O_2 shear coaxial injector flows.

Foust et al. [99] experimentally and numerically studied a GH_2/GO_2 single element injector with an optically accessible combustion chamber. They used the laminar finite-rate chemistry (LFRC) model together with the $k-\varepsilon$ turbulence model. In the LFRC model, the effect of turbulence on chemical reactions is neglected, resulting in convenient model simplifications (see Chapter 2). Reasonable qualitative agreement with measured species mole fractions and quantitative agreement with the measured velocity field were obtained. The agreement deteriorated towards downstream with increasing distance from the injector face.

Schley et al. [101] simulated the same experimental configuration of Foust et al.[99] with 3 different codes; AS3D, MSFC and PSU. All three codes use the LFRC model together with the $k-\varepsilon$ turbulence model. Levels of detail given for the methods used in each code vary but the main differences are:

- AS3D: density-based code, adaptive grid, law-of-the-wall for the turbulence wall treatment, supersonic outlet boundary condition (exit nozzle included in the domain).
- FDNS: pressure-based code, adiabatic wall, law-of-the-wall for the turbulence wall treatment, supersonic outlet boundary condition (exit nozzle included in

Table 3.1: Select literature on CFD simulations of O_2/H_2 shear coaxial injectors.

Publication	Propellants	Test Case	Pressure (MPa)	Domain	CFD Code	Turbulence Model	Chemistry Model
Foust et al. [99]	GO_2/GH_2	Self measurement	1.29	2D	PSU [100]	$k-\varepsilon$	Finite-rate 8 species, 18 reactions
Schley et al. [101]	GO_2/GH_2	Foust et al. [99]	1.29	2D	AS3D [102] FDNS [103] PSU [100]	$k-\varepsilon$	Finite-rate
Oefelein et al. [104]	LOX/GH_2	Mayer et al. [105]	10.1	2D	PSU [100]	LES	Finite-rate 9 species, 24 reactions
Ivancic et al. [106]	LOX/GH_2	Self measurement	6	2D	AS3D [102]	$k-\varepsilon$	Equilibrium
Lin et al. [107]	GO_2/GH_2	Marshall et al. [108]	5.2	2D	FDNS [103] Loci-Chem [20; 21]	Menter's BSL	Finite-rate 7 species, 9 reactions
Oefelein et al. [109]	LOX/GH_2	Oschwald et al. [110]	10.1	3D		DNS LES	Finite-rate 9 species, 19 reactions
Cheng et al. [111]	LOX/GH_2	Vingert et al. [112] Thomas et al. [113]	1 6	2D	FDNS [103]	$k-\varepsilon$	Finite-rate 6 species, 9 reactions
Mack et al. [19]	GO_2/GH_2	Conley et al. [114]	2.75	3D	Loci-Stream [23]	Menter's BSL	Finite-rate 6 species, 9 reactions
Tucker et al. [115]	GO_2/GH_2	Pal et al. [116]	5.42	3D 3D 2D 2D 2D	- LESLIE3D - GEMS Loci-Chem [20; 21]	LES LES LES URANS RANS	Finite-rate Finite-rate Flamelet Finite-rate Finite-rate

the domain).

- PSU: density-based code, low-Re turbulence model near the wall, pressure specified at outlet (exit nozzle excluded).

All three simulations used an axisymmetric domain to model the square combustion chamber. Note that no wall data such as temperature or heat flux distribution was compared. Similar turbulence and chemistry modeling used in different solvers rendered similar results within themselves and the numerical results of Foust et al. [99]. An assessment of modeling approaches was not provided.

Oefelein et al. [104] simulated a LOX/GH_2 high pressure case with a large eddy simulation (LES) model that includes models for non-idealized thermodynamics and multiphase phenomena, but no comparison to experimental data was given. Oefelein [109] subsequently performed a series of simulations using LES and direct numerical simulation (DNS) techniques for fully coupled compressible governing equations to further investigate the effect of non-idealized thermodynamics. Results showed the near jet region to be diffusion dominated with intense property gradients approaching contact discontinuity.

Ivancic et al. [106] used an equilibrium chemistry formulation with $k - \varepsilon$ turbulence model to simulate an experimental LOX/GH_2 single element injector problem. Experiments were also conducted by the authors. An axisymmetric domain and adaptive grid were used. Computed near injector radial OH mass fraction profile was compared to the experimental values measured in gray levels. Hence a quantitative comparison was not available. OH zone thickness in the computation was not predicted correctly. Authors attributed the discrepancy to the equilibrium chemistry assumption.

Lin et al. [107] used FDNS and Loci-Chem codes to simulate the experimental single element GO_2/GH_2 injector setup by Marshall et al. [108]. Both codes used the LFRC model and Menter's baseline turbulence model. Authors investigated the effect of the turbulence wall treatment on wall heat flux predictions. For both codes, low-Re turbulence wall treatment, compared to the simulations employing the law-of-the-wall method, resulted in better agreement in initial rise and peak value of the wall heat flux but over prediction is observed downstream of the re-attachment point. There, the law-of-the-wall simulations yielded better agreement.

Cheng and Farmer [111] used the FDNS code with the LFRC and equilibrium chemistry formulations along with the $k-\varepsilon$ turbulence model to simulate two different LOX/GH_2 single element injector experiments. They used a multiphase flow model with real-fluid propellant properties. Agreement with experimental measurements of radial distribution of mean temperature at several axial locations was fair. The LFRC and equilibrium chemistry computation results were only slightly different.

Mack et al. [19] used the pressure-based Loci-Stream code to simulate the experimental GO_2/GH_2 single element injector configuration due to Conley et al. [114] The rectangular combustion chamber with rounded corners was simulated with a 3D, 45 degree-slice domain. The LFRC model together with Menter's SST turbulence model was used. Combustion chamber peak wall heat flux location was correctly captured although the overall heat flux distribution was under-predicted. A grid resolution sensitivity study for a separate 2D single element injector problem was presented. Development of an oscillatory flame surface was observed with refined grids.

Tucker et al. [115] simulated the GO_2/GH_2 single element injector configuration due to Pal et al. [116] with several different codes representing different turbulent combustion modeling approaches and resolutions ranging from 2D RANS method to 3D LES. The results for the wall heat flux distribution as well as the detailed flow fields largely vary. While no consistent trend in predicted wall heat flux distribution is observed with increased model fidelity and grid resolution, the 3D LES simulation with the largest grid density (about 255 million cells) resulted in a very good agreement with the experimental measurements. A summary of the modeling approaches as well as the wall heat flux results obtained with each is included in the following text.

To our knowledge, turbulence-chemistry interaction effect was accounted for in both studies of Oefelein et al. [104; 109]. It was also considered in some of the studies presented in Tucker et al. [115].

In this chapter, we focus on two different experimental test cases by Vaidyanathan et al. [117] and Pal et al. [116]. With a RANS based framework using Menter's SST turbulence model and the LFRC formulation, the effects of the following modeling aspects are examined:

- Grid resolution,
- Choice of the chemistry mechanism,
- Chamber wall thermal boundary condition,
- Near wall treatment of turbulence.

The turbulence wall treatment is identified as a particularly important factor affecting the prediction accuracy of wall heat flux distribution. A zonal turbulence wall treatment approach is proposed in an effort to improve the prediction accuracy. In the zonal treatment, either the law-of-the-wall or the low-Re treatment (built into the SST turbulence model) is used based on flow attachment to the wall.

In addition, the steady laminar flamelet model (SLFM) is utilized to simulate the Pal et al. [116] case in order to investigate the impacts of turbulence-chemistry interactions and non-equilibrium chemistry. By systematically examining the individual combustion modeling components (laminar finite-rate, assumed PDF with either flamelet or equilibrium assumption), the roles played by chemical non-equilibrium and turbulence-chemistry interactions can be analyzed. Comparing LFRC with SLFM provides a way to assess the importance of turbulence-chemistry interaction effects in these types of injector flows. To investigate chemical non-equilibrium effects, we use the assumed PDF/equilibrium model which is identical to the flamelet model in the limit of zero scalar dissipation rate. Differences in the flow between the PDF/equilibrium model and the SLFM point to the importance, or lack thereof, of chemical non-equilibrium.

In the analysis of the Vaidyanathan et al. [117] case, the Loci-Chem code is used while both Loci-Chem and Loci-Stream codes are utilized for the Pal et al. [116] case. The details of models mentioned in this introduction as well as descriptions of the codes are provided in Chapter 2.

3.1 Reaction Mechanism

Four different H_2/O_2 chemistry mechanisms are evaluated. Reactions along with forward Arrhenius rate coefficients C, η, θ as used in Equation 2.52 are detailed in Table 3.2. While the different mechanisms chosen here share many common reactions, the reaction rates vary significantly in accordance with the original derivation conditions. The conditions under which the 6 species 9 reactions (6s9r) [19] and the 6 species 8 reactions (6s8r) [118] mechanism rates were determined could not be tracked down. On the other hand, the 8 species 9 reactions (8s9r) [119] mechanism targets high pressure combustion cases whereas the 8 species 19 reactions (8s19r) [120] mechanism is validated for a large range of pressures.

3.2 Test Cases

Two different single element injectors are investigated. The first test case is based on the experiments conducted by Vaidyanathan et al. [117]. The experimental setup consists of a GH_2/GO_2 single element shear coaxial injector and a rectangular combustion chamber to allow for optical access through quartz windows. The corners are rounded to withstand the high pressure. The setup is shown in Figure 3.1 and details of the two cases are listed in Table 3.3. Wall heat flux and OH-PLIF measurements were taken. Wall heat flux values are calculated using temperature readings at 3.2 mm and 9.5 mm distances from the inner wall. A schematic of the computational domain is shown in Figure 3.2. $1/8^{th}$ section of the combustion chamber is modeled. A uniform temperature of 500 K is imposed on the chamber wall while the injector face plate is assumed adiabatic. While these imposed conditions may be unrealistic, the correct conditions are not available for cases without prior experimental measurements. Thus it is chosen here to stay independent of experimental data in setting up the boundary conditions. An exception is the chamber pressure which is fixed to its

Table 3.2: Forward Arrhenius rate coefficients of tested reaction mechanisms.

(6s9r) - 6 species, 9 reactions mechanism used by Mack et al. [19]

Reaction	C $m^3/(kmol.s)$	η	θ	Reaction	C $m^3/(kmol.s)$	η	θ
$H_2 + O_2 \rightleftharpoons 2OH$	1.7×10^{10}	0	24,070	$H + O + M \rightleftharpoons OH + M$	1×10^{10}	0	0
$H_2 + OH \rightleftharpoons H_20 + H$	2.19×10^{10}	0	2,590	$2O + M \rightleftharpoons O_2 + M$	2.55×10^{12}	-1	59,390
$2OH \rightleftharpoons H_20 + O$	6.023×10^{9}	0	550	$2H + M \rightleftharpoons H_2 + M$	5×10^{9}	0	0
$H_2 + O \rightleftharpoons OH + O$	1.8×10^{7}	1	4,480	$OH + H + M \rightleftharpoons H_2O + M$	8.4×10^{15}	-2	0
$0_2 + H \rightleftharpoons OH + O$	1.22×10^{14}	-0.91	8,369				

(6s8r) - 6 species, 8 reactions mechanism by Evans and Schexnayder [118]

Reaction	C $m^3/(kmol.s)$	η	θ	Reaction	C $m^3/(kmol.s)$	η	θ
$H_2 + M \rightleftharpoons 2H + M$	5.5×10^{15}	-1	51,987	$H_2O + O \rightleftharpoons 2OH$	5.8×10^{10}	0	9,059
$O_2 + M \rightleftharpoons 2O + M$	7.2×10^{15}	-1	59,340	$H_2O + H \rightleftharpoons OH + H_2$	8.4×10^{10}	0	10,116
$H_2O + M \rightleftharpoons OH + H + M$	5.2×10^{18}	-1.5	59,386	$O_2 + H \rightleftharpoons OH + O$	2.2×10^{11}	0	8,455
$OH + M \rightleftharpoons O + H + M$	8.5×10^{15}	-1	50,830	$H_2 + O \rightleftharpoons OH + H$	7.5×10^{10}	0	5,586

(8s9r) - 8 species, 9 reactions mechanism by Gontkovskaya et al. [119]

Reaction	C $m^3/(kmol.s)$	η	θ	Reaction	C $m^3/(kmol.s)$	η	θ
$H_2 + O_2 \rightleftharpoons 2OH$	2.52×10^{9}	0	4,691	$OH + H_2 \rightleftharpoons H_2O + H$	2.25×10^{10}	0	630
$H + O_2 \rightleftharpoons OH + O$	1.55×10^{11}	0	2,009	$H_2 + O \rightleftharpoons OH + H$	2.46×10^{10}	0	1,183
$2H + M \rightleftharpoons H_2 + M$	3.6×10^{12}	0	0	$H + O_2 + M \rightleftharpoons HO_2 + M$	3.6×10^{12}	0	0
$2OH + M \rightleftharpoons H_2O_2 + M$	1.11×10^{13}	0	231	$HO_2 + HO_2 \rightleftharpoons H_2O_2 + O_2$	1×10^{10}	0	0
$H + H_2O_2 \rightleftharpoons H_2 + HO_2$	1.17×10^{11}	0	1,419				

(8s19r) - 8 species, 19 reactions mechanism by Ó Conaire et al. [120]

Reaction	C $m^3/(kmol.s)$	η	θ	Reaction	C $m^3/(kmol.s)$	η	θ
$H + O_2 \rightleftharpoons O + OH$	1.91×10^{11}	0	8,273	$HO_2 + O \rightleftharpoons OH + O_2$	3.25×10^{10}	0	0
$O + H_2 \rightleftharpoons H + OH$	5.08×10^{1}	2.67	3,166	$HO_2 + OH \rightleftharpoons H_2O + O_2$	2.89×10^{10}	0	-251.6
$OH + H_2 \rightleftharpoons H + H_2O$	2.16×10^{5}	1.51	1,726	$HO_2 + HO_2 \rightleftharpoons H_2O_2 + O_2$	4.2×10^{11}	0	6,029
$O + H_2O \rightleftharpoons 2OH$	2.97×10^{3}	2.02	6,743	$HO_2 + HO_2 \rightleftharpoons H_2O_2 + O_2$	1.3×10^{8}	0	-819.7
$H_2 + M \rightleftharpoons 2H + M$	4.57×10^{16}	-1.4	52,890	$H_2O_2 + M \rightleftharpoons 2OH + M$	1.27×10^{14}	0	22,900
$2O + M \rightleftharpoons O_2 + M$	6.17×10^{12}	-0.5	0	$H_2O_2 \rightleftharpoons 2OH$	2.95×10^{11}	0	24,360
$O + H + M \rightleftharpoons OH + M$	4.72×10^{15}	-1	0	$H_2O_2 + H \rightleftharpoons H_2O + OH$	2.41×10^{10}	0	1,998
$H + OH + M \rightleftharpoons H_2O + M$	4.5×10^{19}	-2	0	$H_2O_2 + H \rightleftharpoons H_2 + HO_2$	6.03×10^{10}	0	4,001
$H + O_2 + M \rightleftharpoons HO_2 + M$	3.48×10^{13}	-0.41	-563	$H_2O_2 + O \rightleftharpoons OH + HO_2$	9.55×10^{3}	2	1,998
$H + O_2 \rightleftharpoons HO_2$	1.48×10^{9}	0.6	0	$H_2O_2 + OH \rightleftharpoons H_2O + HO_2$	1×10^{9}	0	0
$HO_2 + H \rightleftharpoons H_2 + O_2$	1.66×10^{10}	0	412.6	$H_2O_2 + OH \rightleftharpoons H_2O + HO_2$	5.8×10^{11}	0	4,811
$HO_2 + H \rightleftharpoons 2OH$	7.08×10^{10}	0	151				

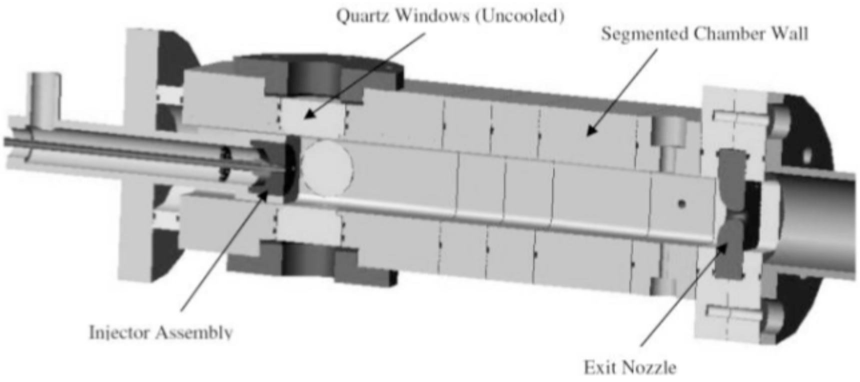

Cross section (mm)	25.4×25.4
Corner radius (mm)	3
Chamber length (mm)	169.3

Figure 3.1: Vaidyanathan et al. [117] combustion chamber configuration.

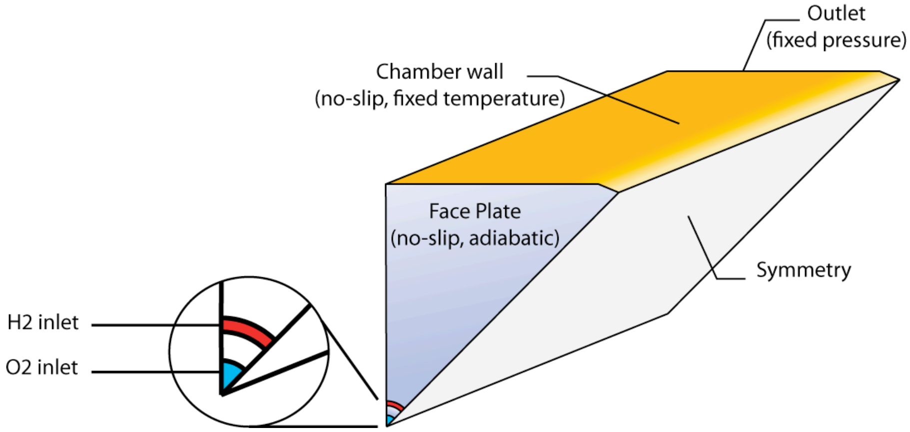

Figure 3.2: Computational domain for the Vaidyanathan et al. [117] injector.

experimentally observed value via a pressure outlet condition. Note that the correct value could be reproduced independently by extending the domain to include the exit nozzle at the expense of additional computational cost. Uniform mass flux profiles of H_2 and O_2 are imposed at the inlets with the values listed in Table 3.3. The inlet temperatures are taken as 300 K. The law-of-the-wall formulation as described in Chapter 2 is used for the chamber wall.

The second test case is based on the measurements reported by Pal et al. [116]. The experimental setup consists of a single element shear coaxial injector, a main

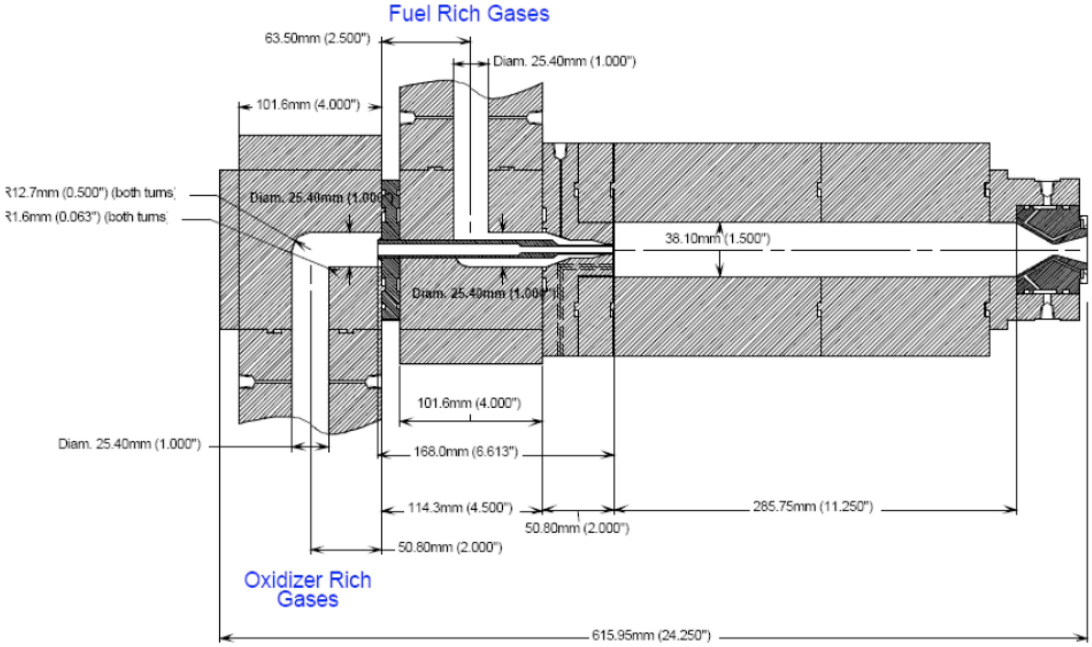

Figure 3.3: Pal et al. [116] injector setup schematic.

cylindrical combustion chamber and two GO_2/GH_2 preburners which provide hot, oxidizer-rich and fuel-rich streams. A schematic of their experimental setup is shown in Figure 3.3. The main chamber wall is instrumented with coaxial heat flux gauges which provide both temperature and heat flux profiles. Details of the experimental conditions are given in Table 3.3, a complete description is provided by Pal et al. [116].

Computational domain and boundary condition types for the Pal et al. [116] injector are depicted in Figure 3.4. Axisymmetric domain is modeled with a 1-degree pie shaped grid (circumferential dimension is exaggerated in Figure 3.4 for clarity). For the chamber wall thermal boundary condition, options of assigning a uniform temperature (700 K) or prescribing the measured temperature profile are evaluated whereas the face plate and exit nozzle temperatures are set to upstream and downstream ends of the measured wall temperature data respectively. As opposed to the Vaidyanathan et al. [117] test case, both inlet and exit nozzles are included in the domain. An extrapolated boundary condition is used at the supersonic exit, so the chamber pressure is not imposed but followed from the solution.

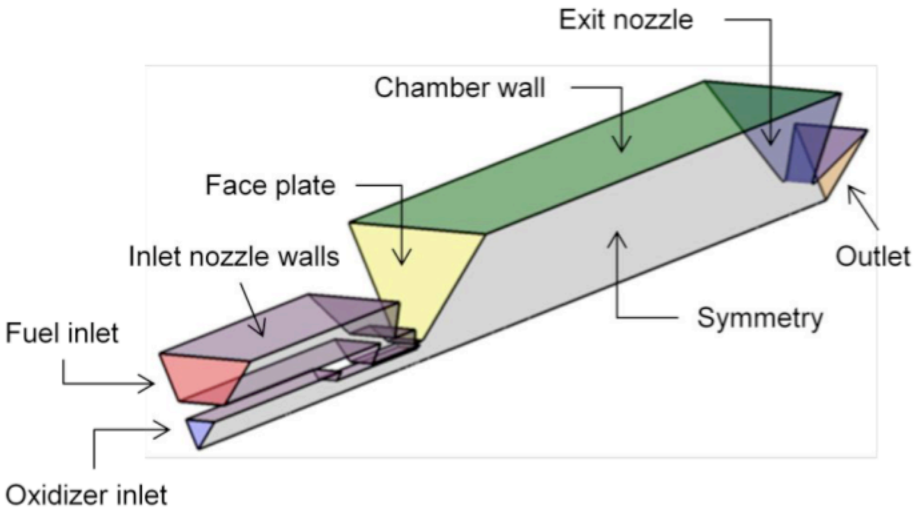

Inlet nozzle walls	Face plate	Chamber wall	Exit nozzle wall
Adiabatic	Uniform T=754 K	Uniform T=700 K or Experimental profile	Uniform T=510 K

Figure 3.4: Computational domain schematic and thermal boundary conditions for the Pal et al. [116] injector.

In SLFM simulations of the Pal et al. [116] injector and in corresponding comparison simulations with the LFRC model, the wall boundaries are taken as adiabatic and the exit nozzle is excluded while imposing the chamber pressure at the outlet. This is done due to the limitations of the SLFM which uses an incompressible formulation and doesn't account for the wall heat transfer (see Chapter 2).

The experiment of Pal et al. [116], compared to that of Vaidyanathan et al. [117] was conducted on a larger chamber with hot fuel and oxidizer being injected in significantly higher velocities resulting in a higher chamber pressure. Also, fuel/oxidizer velocity ratio is twice as high as the Vaidyanathan et al. [117] case.

Table 3.3: Details of the test cases.

		Vaidyanathan et al. [117]	Pal et al. [116]
	Chamber pressure (bars)	37	54.2
	Oxidizer post inner diameter (mm)	1.2	5.26
	Oxidizer post thickness (mm)	1	1.04
	Fuel annulus diameter (mm)	2.69	7.49
	Chamber height (mm)	25.4	38.1
	Chamber length (mm)	169	286
Fuel	Fuel mass flux (g/s)	0.58	33.1
	H_2 mass fraction in fuel	1	0.402
	Velocity (m/s)	103.5	740
	Temperature (K)	300	811
Oxidizer	Oxidizer mass flux (g/s)	2.198	90.4
	O_2 mass fraction in oxidizer	1	0.945
	Velocity (m/s)	41.4	146
	Temperature (K)	300	700
	Equivalence ratio	2.11	1.24
	Fuel/Oxidizer velocity ratio	2.5	5.07
	Oxidizer/Fuel mass flux ratio	3.79	2.73
	Fuel Reynolds Number†	8E3	7E4
	Oxidizer Reynolds Number‡	1E5	6E5
	Measurements	Wall temperature Wall heat flux OH concentration field	Wall temperature Wall heat flux

†Based on annulus gap height at inlet nozzle exit

‡Based on diameter at inlet nozzle exit

3.3 Results and Discussions

Table 3.4 provides a summary of the numerical test matrix for each case. The results and discussions are provided for each test in the following sections.

The Loci-Chem [20; 21] and Loci-Stream [23] codes are utilized in this chapter. Brief descriptions of both codes are provided in Chapter 2.

Simulations for both the Vaidyanathan et al. [117] and the Pal et al. [116] cases are conducted with the Loci-Chem code using the LFRC model. The Favre-averaged governing equations including the transport equations for each species, as shown in

Table 3.4: Summary of numerical tests.

Test Item	**Vaidyanathan et al. [117]**	**Pal et al. [116]**
Grid resolution levels (# cells)	51K, 217K, 740K, 2,214K, 2,003K	100K, 127K, 496K
Chemistry mechanisms	6s9r 6s8r 8s9r 8s19r	6s8r 8s19r
Law-of-the-wall vs. Low-Re	✔	✘
Uniform wall temperature vs. Using experimental profile	✔	✘
Turbulence model	Menter's SST	Menter's SST
Combustion model	LFRC	LFRC and SLFM
Code	Loci-Chem [20; 21]	Loci-Chem [20; 21] Loci-Stream [23]

Section 2.2, are solved. Effect of turbulent fluctuations on the reaction rates are not accounted for. Hence, no turbulent combustion closure model (such as those listed in Chapter 2) is used.

Note that the SLFM is only implemented in the Loci-Stream code. To facilitate a comparative study between the LFRC model and the SLFM, Pal et al. [116] case is also simulated with models using the Loci-Stream code. Several comparisons as follows provide assessments of the effects of turbulence-chemistry interactions and non-equilibrium chemistry.

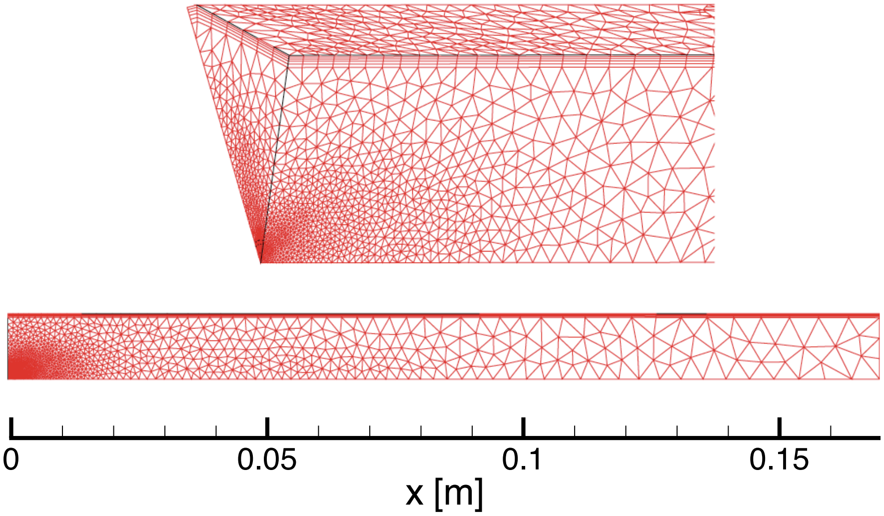

Figure 3.5: Two views of the coarsest grid (51K cells) for the Vaidyanathan et al. [117] injector.

3.3.1 Vaidyanathan et al. [117] Injector

Grid Resolution Sensitivity

The accuracy of CFD simulations largely rely on sufficient resolution of the flow features by the computational grid. Ideally, the grid should be fine enough that upon further refinement, solution is virtually unchanged. This grid insensitive level is demonstrated by starting with an initial coarse grid and performing simulations for four progressive grid refinement levels.

The grids used consist of tetrahedral cells with slender prisms for the chamber wall boundary layer and pyramids for transition between prisms and tetrahedra. Cells are clustered near the H_2/O_2 inlets and the mixing layer. Five different grids were tested to assess the sensitivity of simulations to grid resolution. Figure 3.5 shows two views of the coarsest grid.

Table 3.5 lists the total number of cells for each grid. Each level of refinement corresponds to a decrease in cell length scales by a factor of approximately 1.5 as uniformly as possible. Although Grid 5 has less total number of cells compared to Grid

Table 3.5: Grid sizes.

Grid No	**1**	**2**	**3**	**4**	**5**
Number of Cells	51K	217K	740K	2,214K	2,003K

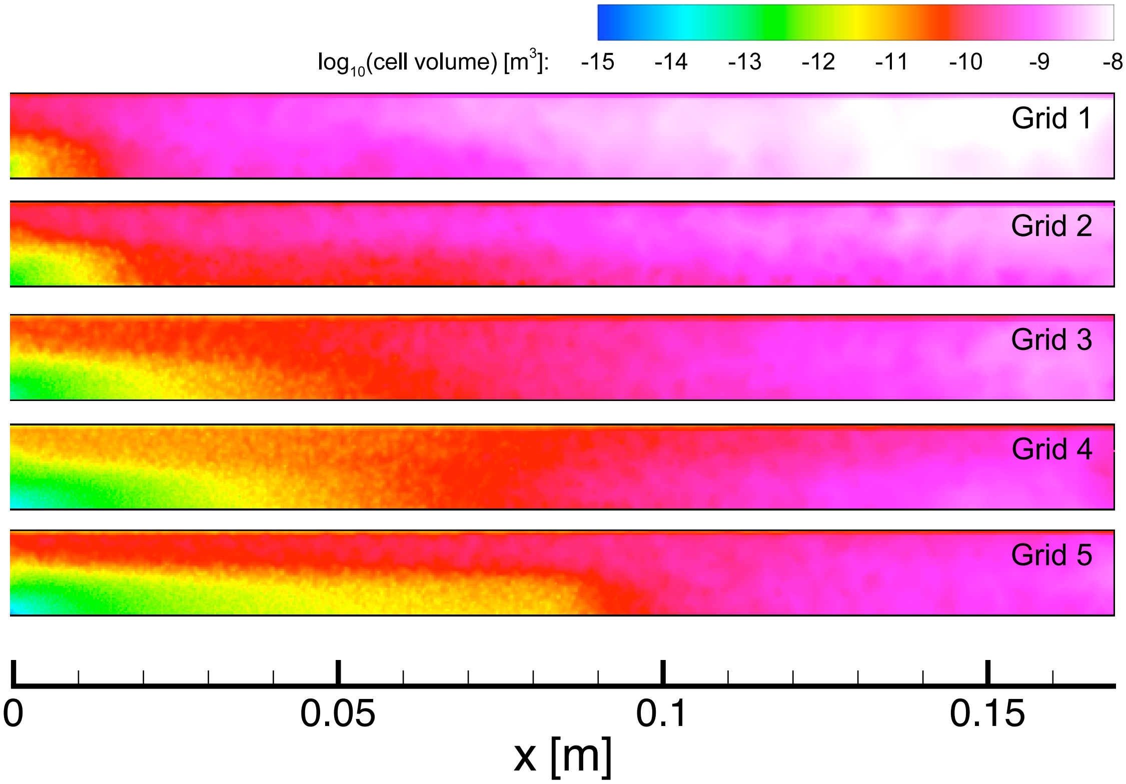

Figure 3.6: Grid cell volume distribution on the symmetry plane (Vaidyanathan et al. [117] injector).

4, it is refined in the flame region and coarsened elsewhere guided by the experience drawn from previous simulations. Distribution of grid points in the domain can be observed in Figure 3.6 where the cell volume contours are plotted for each grid.

Figure 3.7 shows a comparative view of the temperature field outcomes of the tested grids. As the grid is progressively refined, three general trends can immediately be observed:

- Flame is less dispersed,

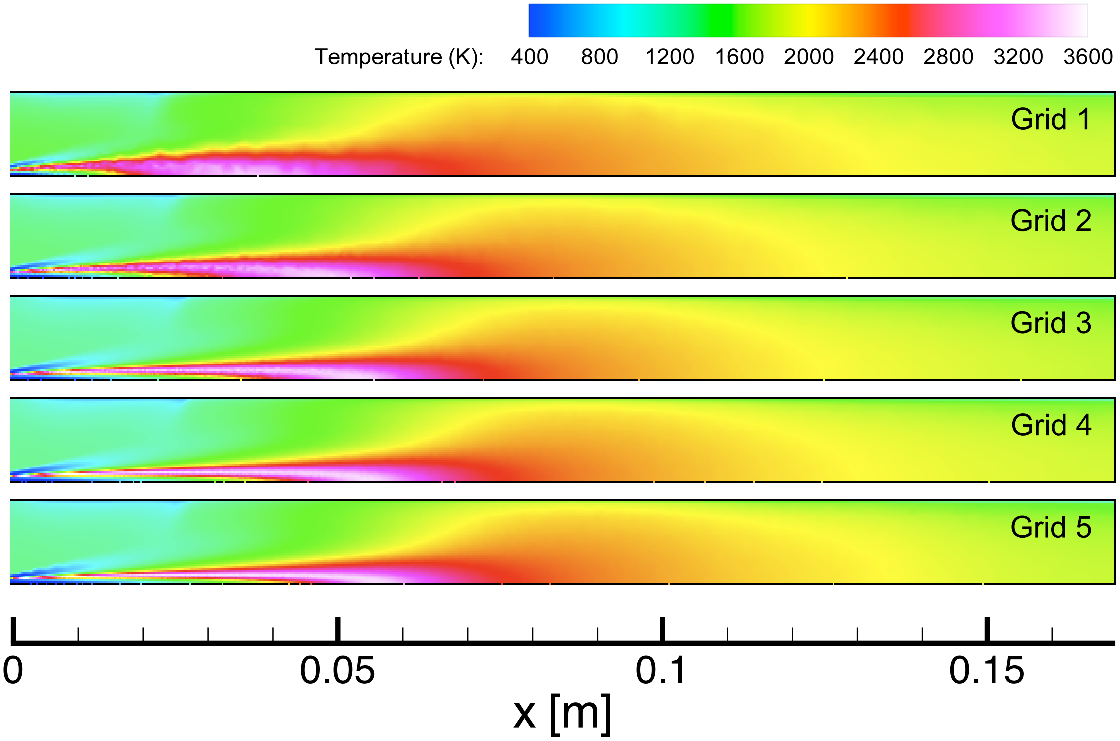

Figure 3.7: Temperature contours for different grid resolutions (Vaidyanathan et al. [117] injector).

- Although the combustion lengths are similar, flame merges to the centerline farther downstream,
- Upper left quadrant of the domain attains slightly lower temperatures.

Centerline OH mass fraction distributions for each grid are shown in Figure 3.8. The distributions shown provide indications of flame length and location of flame merge to the centerline which translates into how fast mixing of the fuel and oxidizer streams occur. Figure 3.8 confirms the observation that insufficient grid resolution results in a more dispersed flame and an earlier mixing compared to the finer grid solutions. Grid 3 to Grid 5 show consistent prediction of the peak OH mass fraction at the centerline and only slightly different merge locations.

Figure 3.9, on the other hand, compares the chamber wall heat flux distributions. Grid 2 and Grid 4 results are skipped for the sake of clarity as the results are prac-

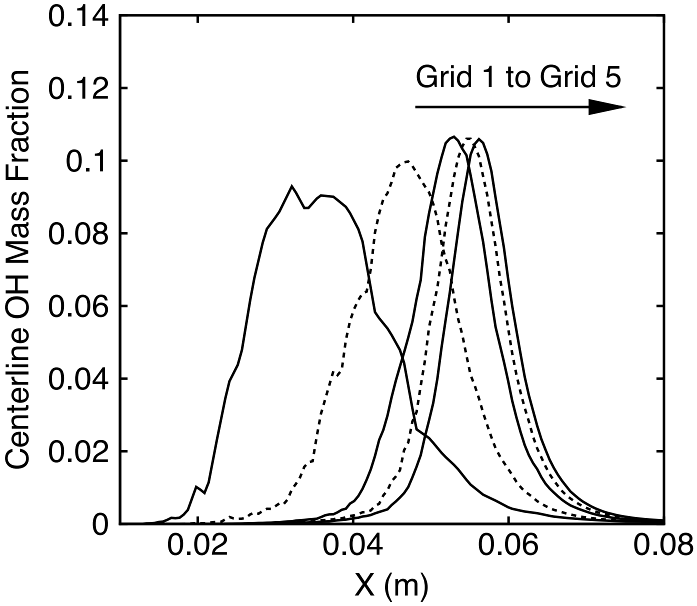

Figure 3.8: Centerline OH mass fraction distributions for different grid resolutions.

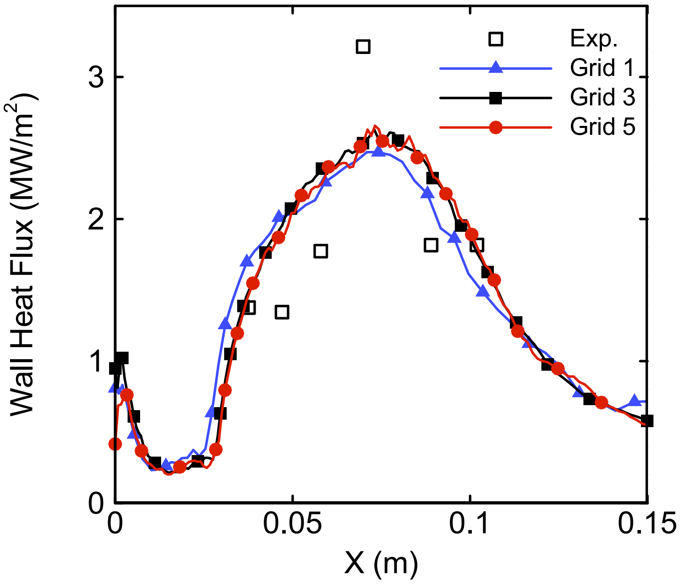

Figure 3.9: Chamber wall heat flux distributions for different grid resolutions.

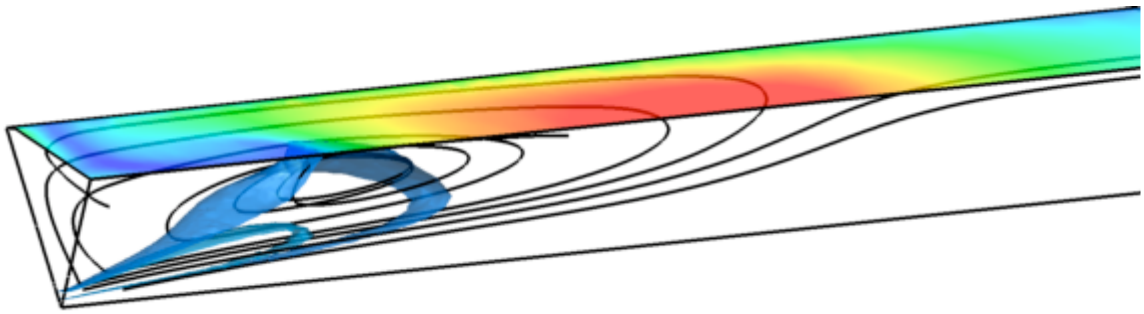

Figure 3.10: A 3D view of the solution (Vaidyanathan et al. [117] injector). Top wall contours: heat flux, Iso-surfaces: correspond to OH mass fractions of 0.16 (outer) and 0.2 (inner).

tically identical to those of Grid 3 and Grid 5. Grid 1 exhibits slightly smaller peak heat flux value as well as a slight shift of the profile towards downstream. Overall, the wall heat flux feature proved largely insensitive to the grid resolution. This is also evident from the very similar near wall temperature distributions shown in Figure 3.7.

Note that the chamber wall is placed 4.2 outer injector diameters away from the injector. A large vortex on the upper left quadrant entraining part of the fuel stream cools the upstream portion of the wall. It is only when the stream attaches to the wall that the heat from the flame is transmitted to the wall. Thus the location and value of the peak heat flux is largely independent of how well the flame is resolved but it depends more on the total energy output of the flame. Figure 3.10 demonstrates these points.

Sensitivity to Chemistry Mechanism

Reduced reaction mechanisms for a particular chemistry is generally derived and validated for specific types of problems and ranges of pressure, mixedness, etc. Hence, they are not universally applicable. As detailed in Table 3.2 before, four different H_2/O_2 reaction mechanisms are chosen to be evaluated. Table 3.6 lists some common reactions between them and gives reaction rate constants at 3000 K temperature as

Table 3.6: Rate constants in $m^3/(kmol.s)$ calculated at 3000 K temperature for some of the common reactions between different chemistry mechanisms.

	6s9r	6s8r	8s9r	8s19r
$H_2 + O_2 \rightleftharpoons 2OH$	5.57×10^6	-	5.3×10^8	-
$OH + H_2 \rightleftharpoons H_2O + H$	9.2×10^9	reverse:2.9×10^9	1.8×10^{10}	2.2×10^{10}
$H_2O + O \rightleftharpoons 2OH$	reverse:5×10^9	2.8×10^9	-	3.3×10^9
$H_2 + O \rightleftharpoons OH + H$	1.2×10^{10}	1.2×10^{10}	1.7×10^{10}	3.4×10^{10}
$O_2 + H \rightleftharpoons OH + O$	5.1×10^9	1.3×10^{10}	7.9×10^{10}	1.2×10^{10}
$O + H + M \rightleftharpoons OH + M$	1×10^{10}	reverse:1.2×10^5	-	1.6×10^{12}
$2O + M \rightleftharpoons O_2 + M$	2.1	reverse:6.2×10^3	-	1.1×10^{11}
$H_2 + M \rightleftharpoons 2H + M$	reverse:5×10^9	5.46×10^4	reverse:3.6×10^{12}	1.4×10^4
$H + OH + M \rightleftharpoons H_2O + M$	9.3×10^8	reverse:8×10^4	-	5×10^{12}
$2HO_2 \rightleftharpoons H_2O_2 + O_2$	-	-	1×10^{10}	5.6×10^{10}
$H_2O_2 + H \rightleftharpoons H_2 + HO_2$	-	-	7.3×10^{10}	1.6×10^{10}
$H + O_2 + M \rightleftharpoons HO_2 + M$	-	-	3.6×10^{12}	1.6×10^{12}

calculated via Equation 2.52. Entries in the table are shaded based on the calculated rate constants; darker color corresponding to higher rates. The entries labeled as "reverse" give reverse reaction rate constants as the forward rate coefficients are not available. Note that the forward and reverse rates for a given reaction may not necessarily be on the same order. Hence, a comparison between them is not informative.

At the test temperature of 3000 K, individual reaction steps belonging to the 8 species mechanisms (8s9r and 8s19r) generally exhibit a trend of larger rate constants but still stay on the same order. The third body reactions (M reactions), on the other hand, show greater variation in rate constants. There is no clear trend between the two 6 species or 8 species mechanisms among themselves. While disparities between individual reaction rates for each mechanism are apparent, this analysis does not offer insight into the integrated effect. To have a more quantitative idea about the response time scales of these mechanisms, the following test procedure is adopted:

1. Sample thermodynamic state of an in-flame point from one of the current simulations,

Table 3.7: Thermodynamic state of the sampled in-flame point perturbed by 20% O_2 addition.

		Mass Fractions					
Pressure (bar)	**Temperature (K)**	H_2	O_2	OH	O	H	H_2O
37	3000	0.06793	0.000326	0.01936	0.00117	0.00148	0.90733

2. Perturb the sampled thermodynamic state by introducing 20% additional O_2,
3. Integrate the 4 different reaction mechanisms in time until convergence to a new equilibrium state.

The perturbed state (step 2) is listed in Table 3.7. Results of the step 3 is presented in Figure 3.11 as the time history of species mass fractions.

Note that the state listed in Table 3.7 is still fuel rich. So the additional oxygen drives the reactions towards consuming some of the available H_2, producing more H and H_2O. An interesting observation is that compared to 6s9r and 8s19r mechanisms, the 6s8r and 8s9r mechanisms consumed the same amount of O_2, but consumed more of H_2 resulting in higher H and H_2O with lower OH levels. Even when two particular chemistry mechanisms have the same set of reaction steps, with possibly different rates, their equilibrium states for a given condition can be different due to the different interplay between the individual reaction steps. In this case, although disparities between the new equilibrium states exist, the magnitude of the difference is minute.

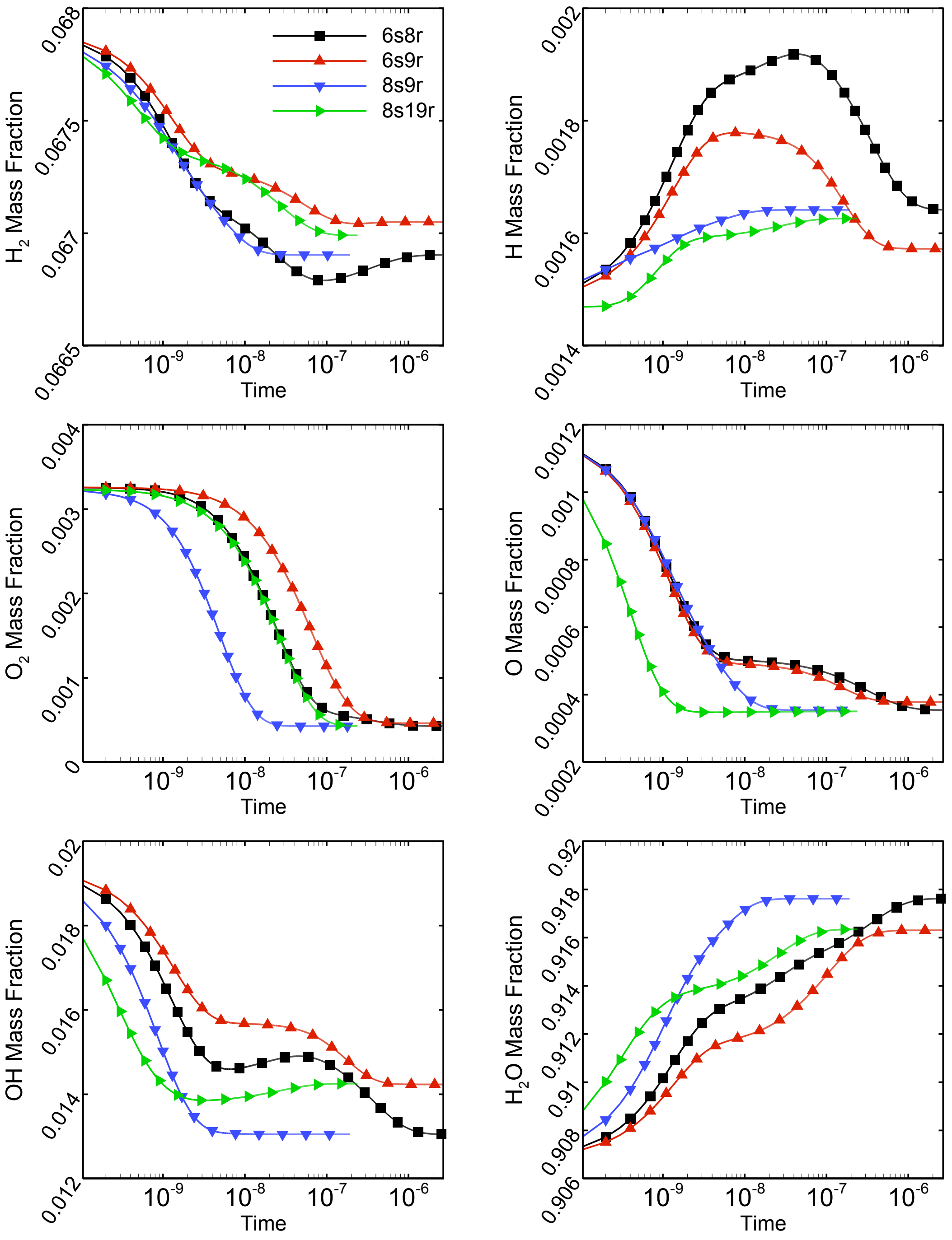

Figure 3.11: Time history of reaction mechanism responses.

Table 3.8: Fluid flow time scales in seconds.

τ_d	$\tau_{c,local}$	$\tau_{c,global}$
$\sim 10^{-4}$	$\sim 10^{-5}$	$\sim 10^{-3}$

Figure 3.11 also demonstrates that there is a noticeable disparity between the time scales of the 8 species and 6 species mechanisms as predicted whereas within themselves, they are consistent in terms of response speed. This can have a large impact on simulations unless the fluid flow time scales (whether diffusive or convective) are much larger than those of chemistry. The following definitions of flow time scales are considered:

Diffusive time scale:

$$\tau_d = \frac{\ell^2}{\nu + \nu_t} \tag{3.1}$$

Local convective time scale (cell residence time):

$$\tau_{c,local} = \frac{\ell}{|u|} \tag{3.2}$$

Global convective time scale:

$$\tau_{c,global} = \frac{\text{flame length}}{\text{average velocity within flame}} \tag{3.3}$$

where ℓ is the local grid cell length scale.

The same point in the flow field, thermodynamic state of which was sampled in step 1 of the described test procedure, was used to calculate the time scale values listed in Table 3.8.

Figure 3.11 reveals that even the overall slowest reaction mechanism reaches the equilibrium state at around 10^{-6} seconds. Thus, at least for the near flame conditions, it can be assumed that the chemical reactions reach a local equilibrium and the different mechanisms chosen here are expected to result in close, if not identical, solutions. In fact, Vaidyanathan et al. [117] injector case was solved with all the listed chemistry mechanisms and identical results were obtained. It should be noted that in the present computational framework, chemical reactions are handled based on the mean flow variables, and no detailed treatment has been made in regard to turbulence-chemistry interactions. It is well known [68] that this aspect can substantially affect the outcome of the reaction rates and the mean thermal and velocity fields.

3.3.2 Pal et al. [116] Injector

This test case was studied before by Tucker et al. [115] where several researchers simulated the same problem using different turbulence models and resolutions ranging from 3D LES to 2D RANS. Both finite-rate chemistry and flamelet models were used. A comparison of wall heat flux values obtained in this study versus Tucker et al. [115] is provided later in Figure 3.18 along with a brief summary of methodologies utilized by Tucker et al. [115].

We, instead, took a lateral approach, i.e., given our CFD framework of RANS turbulence closure and the LFRC model, several aspects that may impact simulation accuracy are assessed. The test matrix is summarized in Table 3.9. Options utilized for Case 1 are highlighted in grey. For each progressive case, a single option (boxed in Table 3.9) is changed over the previous case configuration. One exception is that the chemistry mechanism option is reverted to 6s8r for the Case 5. Note that Grid 2 is identical to Grid 1 except that the latter has a more refined wall boundary layer so as to yield $y^+ < 1$. The geometry considered in the simulation is axisymmetric.

In addition to the test matrix shown in Table 3.9, a number of simulations with the SLFM are performed. The details and results are shown in Section 3.4 where the effect of the turbulence-chemistry interactions and non-equilibrium chemistry are discussed.

Table 3.9: Pal et al. [116] injector test cases.

No	**Wall Temperature**	**Law-of-the-wall**	**Chemistry Mechanism**	**Grid**	**Number of Cells**	y^+ **max**
1	Uniform:700 K	yes	6s8r	Grid 1	100K	15
2	Experimental Distribution	yes	6s8r	Grid 1	100K	13
3	Experimental Distribution	no	6s8r	Grid 2	127K	0.11
4	Experimental Distribution	no	8s19r	Grid 2	127K	0.11
5	Experimental Distribution	no	6s8r	Grid 3	496K	0.24

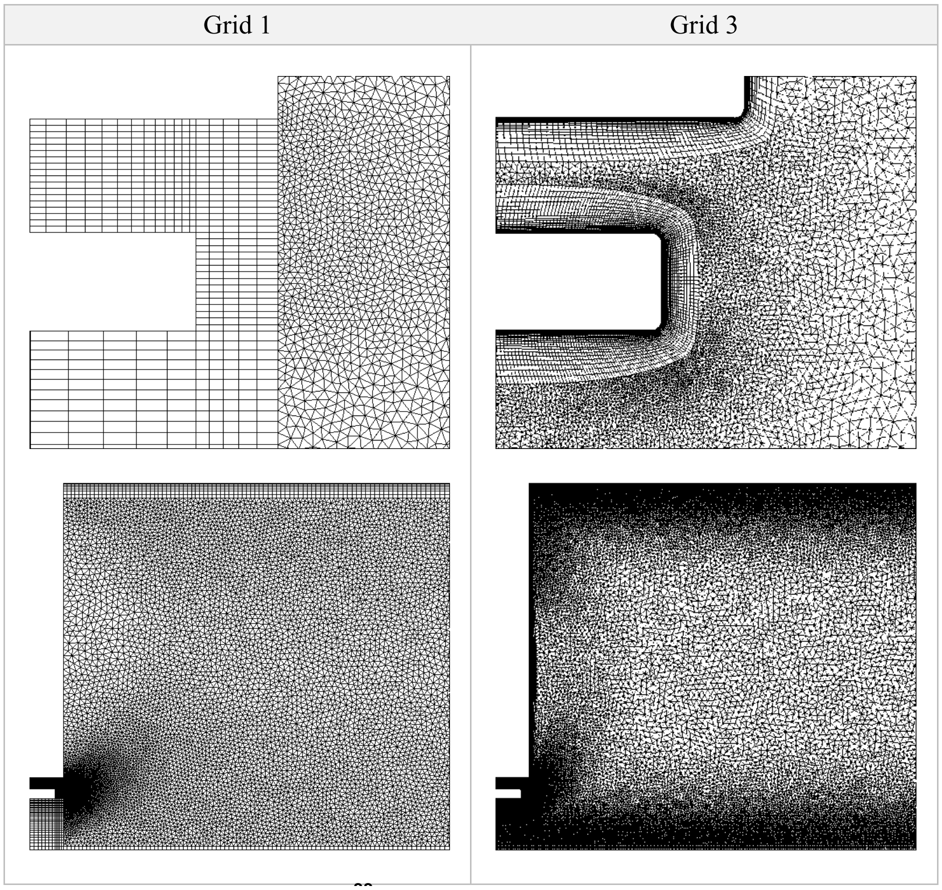

Figure 3.12: Grid views for Pal et al. [116] injector. Top row: injector close-up, Bottom row: full height view of the near injector region.

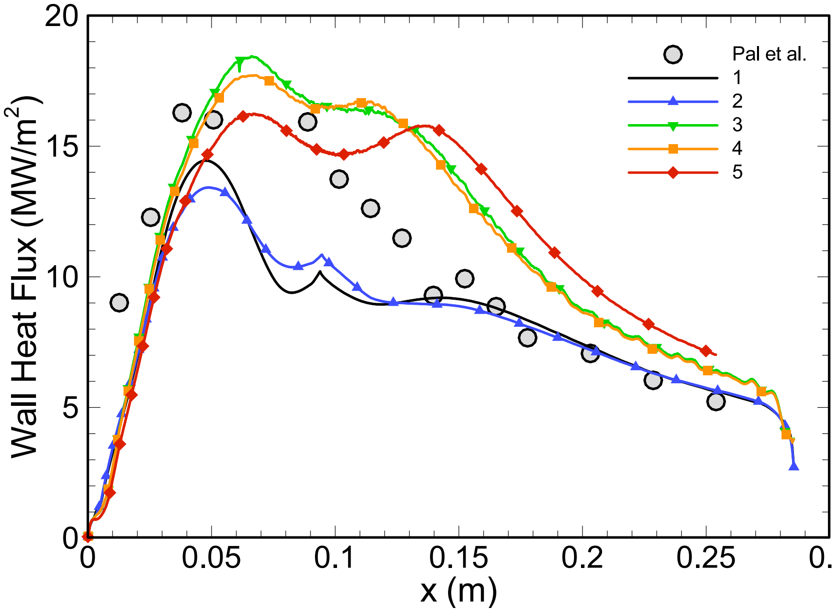

No	Wall Temperature	Law-of-the-wall	Chemistry Mechanism	Grid	Number of Cells	y^+ max
1	Uniform:700 K	yes	6s8r	Grid 1	100K	15
2	Experimental Distribution	yes	6s8r	Grid 1	100K	13
3	Experimental Distribution	no	6s8r	Grid 2	127K	0.11
4	Experimental Distribution	no	8s19r	Grid 2	127K	0.11
5	Experimental Distribution	no	6s8r	Grid 3	496K	0.24

Figure 3.13: Wall heat flux distributions in comparison to experimental data by Pal et al. [116].

Figure 3.13 shows wall heat flux distributions compared to the experimental measurements while Figure 3.16(a) and Figure 3.16(b) compares temperature and OH mass fraction fields respectively for each case.

Case 1 vs. Case 2: Uniform wall temperature of 700 K vs. imposing experimental temperature profile

Given a problem definition, a predictive CFD simulation should ideally be independent of incorporating any experimental measurement. For the current injector setup, this is a challenging objective in terms of the chamber wall thermal boundary condition. In order to achieve independent simulations, one needs to perform a conjugate simulation of the solid enclosing the combustion chamber and the ambient flow which adds greatly to the complexity of the simulations. As an alternative, assigning an estimate uniform wall temperature is explored and compared with the case of assigning the experimental temperature profile at the wall. The resulting temperature and OH mass fraction fields are indistinguishable. A slight difference in wall heat flux distributions is observed while the integrated wall heat transfer values were similar.

Figure 3.14(a) shows experimentally measured wall temperature distribution and the imposed uniform temperature value. The wall heat flux distributions obtained using each thermal boundary condition are also overlaid. Denoting the heat flux obtained using the experimental temperature distribution as $q_{w,T_{exp}}$ and the heat flux obtained using a uniform wall temperature of $700K$ as $q_{w,700K}$, following general observations are made from Figure 3.14(a) :

- $q_{w,700K}$ and $q_{w,T_{exp}}$ are generally in good agreement except in two regions which can be identified as the peak heat flux region and the recirculation closure region.

- Around the peak heat flux region, $q_{w,700K} > q_{w,T_{exp}}$ while $T_{exp} > 700K$. This is intuitive since a colder wall next to a hot gas is expected to experience a higher heat transfer rate.

- Around the recirculation closure region ($x \approx 0.1m$), this trend reverses while $T_{exp} > 700K$ still holds true. A closer local look at the near wall region at $x = 0.1m$ (Figure 3.14(b)) reveals that the temperature gradient calculated with $T = 700K$ is actually slightly steeper as expected. However, note that the heat flux value is not calculated based on the resolved gradient at the wall. Instead, it is calculated using the law-of-the-wall formulation. The law-of-the-wall, as

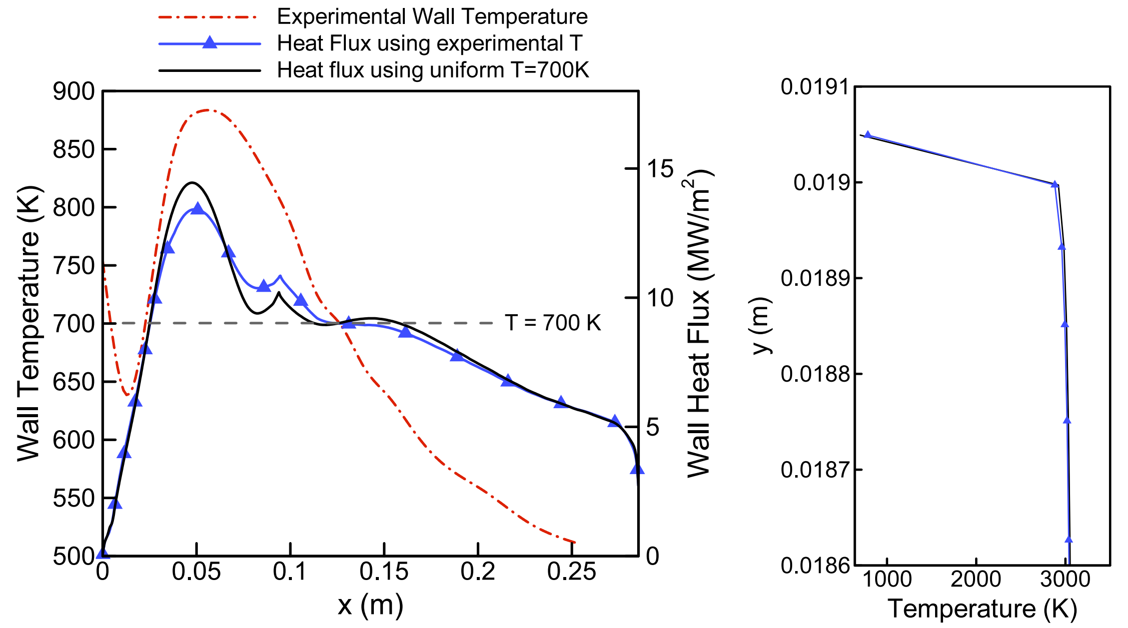

(a) Wall boundary temperature distributions and corresponding wall heat fluxes.

(b) Near wall temperature profiles at $x = 0.1m$ for different temperature boundary conditions.

Figure 3.14: Effect of wall temperature boundary condition on wall heat flux.

stressed before, is strictly only valid for wall attached, boundary layer type flows. This is clearly violated near the stagnation region where the recirculation zone closes. Thus, the heat flux distributions shown in Figure 3.14(a) near $x \approx 0.1m$ are not reliable.

Case 2 vs. Case 3: Law-of-the-wall vs. low-Re model

Alternative near wall treatments of turbulence are described in detail in Chapter 2. The law-of-the-wall treatment is based on an assumed velocity profile and an analogy between shear stress and heat flux. The assumed near wall velocity profile is based on the empirically observed similarity of a non-recirculating wall-bounded turbulent boundary layer flow structure. Strictly, its application to complex flow fields involving substantial flow curvatures, recirculation, and pressure gradients is invalid. The low-Re approach is conceptually more appropriate to resolve the small length

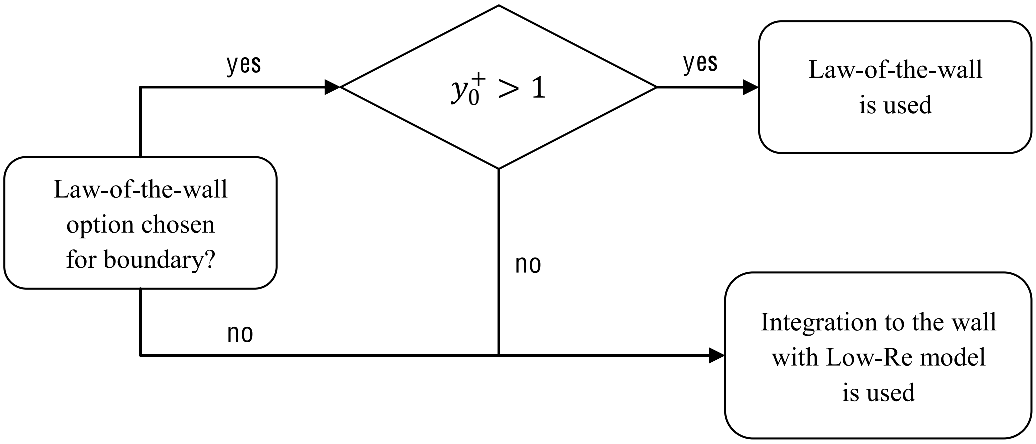

Figure 3.15: Choice of wall treatment.

scale phenomena such as shear stress and heat flux. A competing issue is that the wall dampens the turbulent fluctuation and the Reynolds number locally, requiring that the turbulence model be revised. This requires a good handling of the local flow structures and is not a straightforward task. A low-Reynolds number modification to the turbulence model as described in Chapter 2 is utilized locally near the solid walls whence the resolution of the grid is sufficient based on the switch shown in Figure 3.15.

Our focus here is to conduct a computational assessment of the alternative wall treatments in order to help shed light on the effectiveness and challenges of them.

Integrating to the wall with the low-Re model, in this case, resulted in a better prediction of the peak wall heat flux value whereas use of the law-of-the-wall yielded a corresponding under-prediction. Note that the recirculating region extends up to $x \approx 0.1m$. Further downstream after the re-attachment point, a reversal of the trend is observed consistent with the argument above and the findings of Lin et al. [107]; law-of-the-wall result more closely follows the experimental data and the low-Re model causes an over-prediction there. Figure 3.17 shows axial velocity and temperature profiles along the chamber section at $1/4^{th}$ and $3/4^{th}$ chamber lengths corresponding to recirculating and attached flow regions respectively.

Low-Re model consistently results in effectively fuller momentum and thermal boundary layers, hence a larger shear stress and heat transfer rate. Increased heat loss causes an overall cooler thermal field and a decreased extent of the flame as observed in Figure 3.16(a) and Figure 3.16(b).

Case 3 vs. Case 4: 6 species 8 reactions chemistry mechanism vs. 8 species 19 reactions mechanism

For the previous injector setup (Vaidyanathan et al. [117] case), 4 different chemistry mechanisms were tested and found to yield identical results. For the Pal et al. [116] injector, however, we observe a minimal overall decrease in wall heat flux and a slight increase in OH mass fraction near the flame core. The underlying reasons need to be investigated to be able to offer more insight.

Case 4 vs. Case 5: Grid refinement

Grid 3 used for Case 5 (see Table 3.9) is substantially finer near the injector post, flame core and chamber wall boundary. An outcome similar to the grid independence study of the Vaidyanathan et al. [117] injector is reached: Refined grid causes a slower mixing of fuel and oxidizer streams, hence increasing the flame length as can be seen from Figure 3.16(a) and Figure 3.16(b). Shifting of the flame towards downstream also reflects on the wall heat flux profile with elevated values downstream and a reduced peak value.

Case 5 vs. Tucker et al. [115]

Figure 3.18 shows our current wall heat flux results in comparison to those reported by Tucker et al. [115]. The first observation, also noted by Tucker et al. [115], is that there is no progressive convergence to the experimental results as the CFD model fidelity is increased. However, the Tucker et al.-1 case, which uses LES together

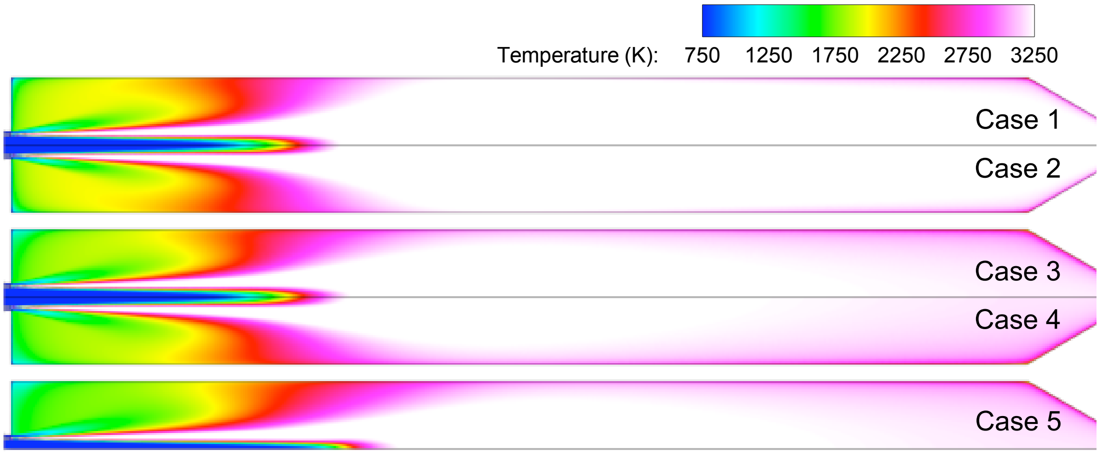

(a) Temperature fields

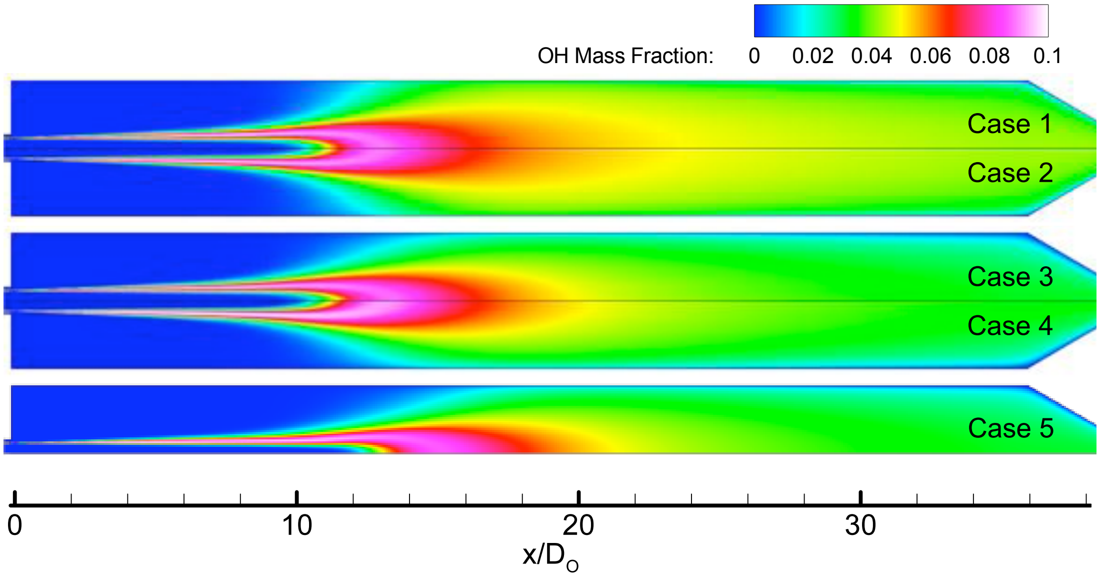

(b) OH mass fraction fields

No	**Wall Temperature**	**Law-of-the-wall**	**Chemistry Mechanism**	**Grid**	**Number of Cells**	y^+ **max**
1	Uniform:700 K	yes	6s8r	Grid 1	100K	15
2	Experimental Distribution	yes	6s8r	Grid 1	100K	13
3	Experimental Distribution	no	6s8r	Grid 2	127K	0.11
4	Experimental Distribution	no	8s19r	Grid 2	127K	0.11
5	Experimental Distribution	no	6s8r	Grid 3	496K	0.24

Figure 3.16: Comparative views of the temperature and OH mass fraction fields (Pal et al. [116] injector).

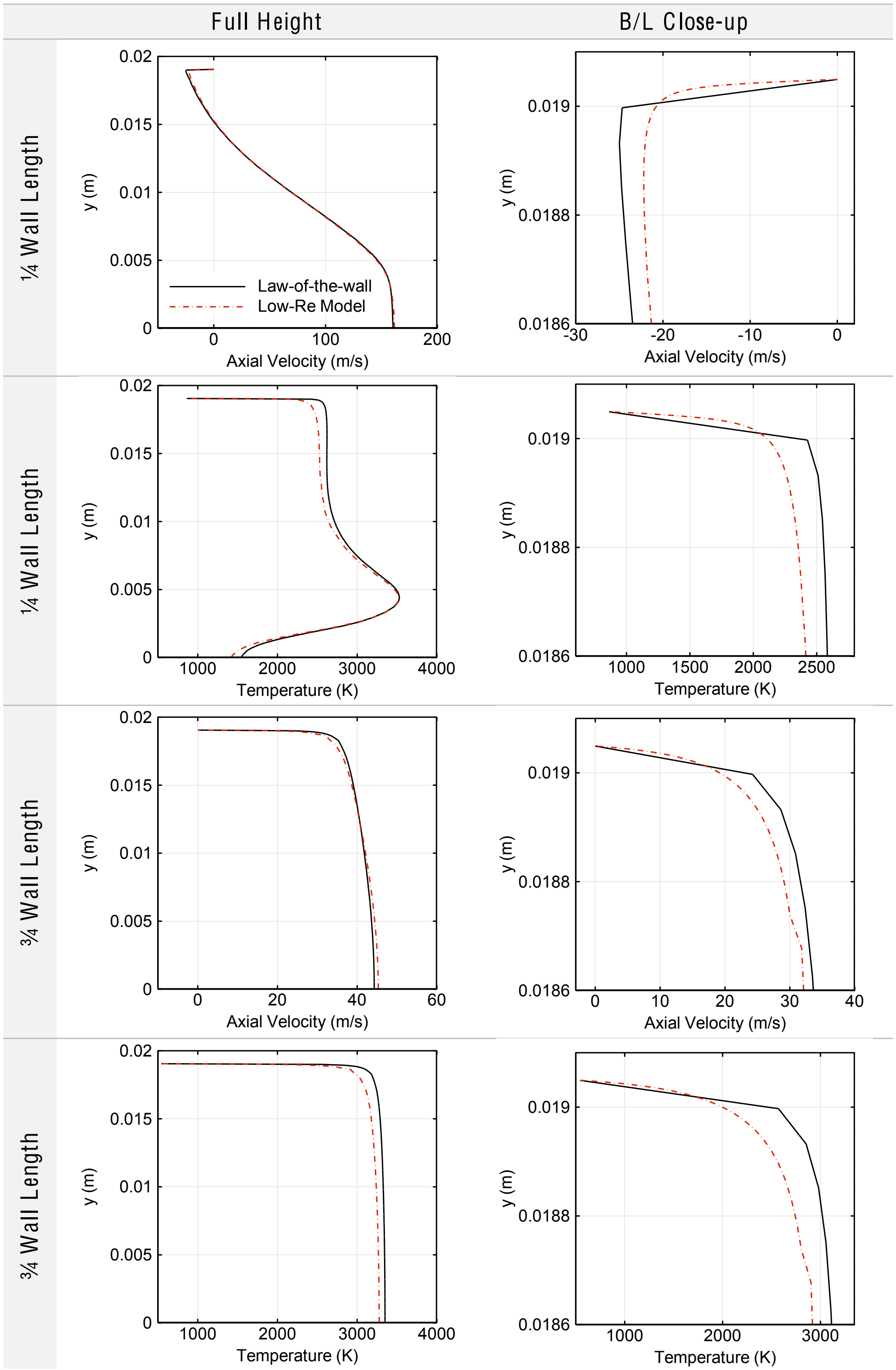

Figure 3.17: Axial velocity and temperature profiles along chamber height at $1/4^{th}$ and $3/4^{th}$ chamber length sections (Pal et al. [116] injector).

with a 255 million cell grid, exhibits the overall best match to the experimental data. Our RANS model results, depending on whether the law-of-the-wall formulation was used or not, display close match to experimental profile in either the downstream or upstream portion of the wall respectively.

Current results suggest that the RANS framework can be an accurate and relatively feasible tool for predicting injector type flows. A logical next step for us here is to adopt the low-Re model for the upstream recirculating region but to switch to the law-of-the-wall treatment in the downstream portion following the re-attachment point. This approach is explored in the next section.

3.3.3 Zonal Wall Treatment for the Pal et al. [116] Case

The results presented in the previous section for the Pal et al. [116] case showed that the largest variation in the wall heat flux distribution prediction was due to the choice of the turbulence wall treatment. The observations prompted exploration of a zonal approach where depending on flow attachment to the chamber wall;

- Low-Re model is applied in the upstream portion of the wall corresponding to the recirculating region. As noted before, this portion is already known to extend up to $x \approx 0.1m$.
- Law-of-the-wall is applied for the rest of the chamber wall downstream where the flow is known to be attached to the wall.

In this zonal approach, a fine boundary layer grid ($y^+ < 1$ for the first grid cell center off the boundary) needs to be used for the upstream portion (direct integration for the low-Re model). Whereas, boundary layer grid must be coarsened downstream after the re-attachment point to allow application of the law-off-the-wall method. Thus, a new grid is prepared which uses the boundary layer discretization of Grid 1 in the upstream portion of the chamber wall and Grid 2 in the downstream portion.

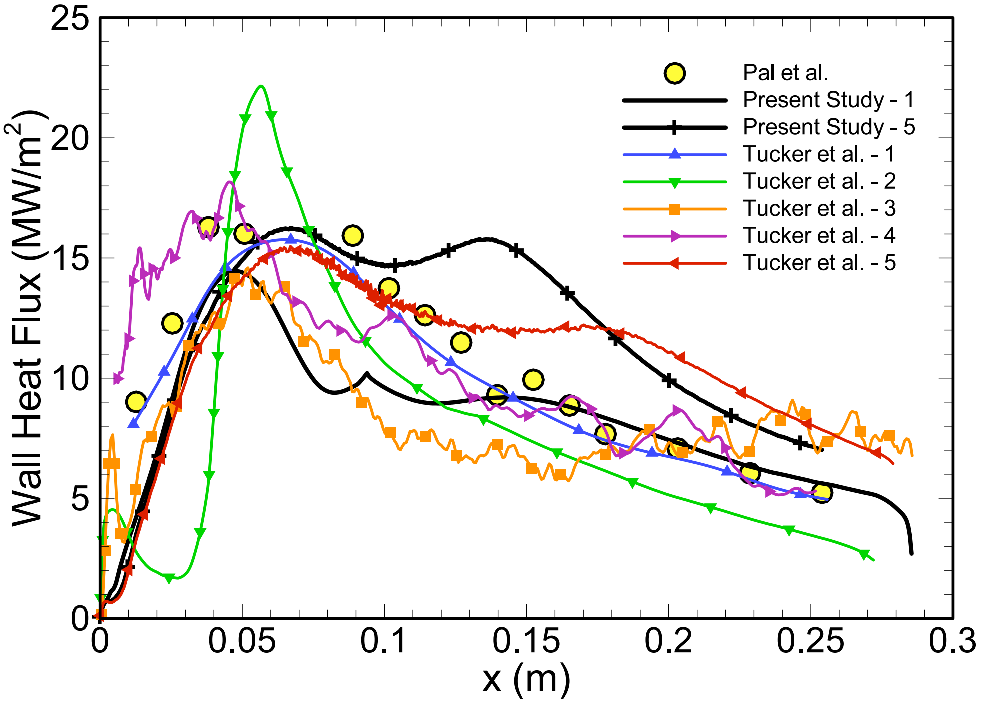

Designation	**Chemistry**	**Turbulence Model**	**Dimension**	**Grid Size**	**Time Step (μsec)**
Tucker et al. - 1	Finite-rate	LES	3D	255,000K	0.068
Tucker et al. - 2	Finite-rate	LES	3D	3,160K	0.01
Tucker et al. - 3	Flamelet	LES	2D	263K	0.1
Tucker et al. - 4	Finite-rate	URANS	2D	250K	0.1
Tucker et al. - 5	Finite-rate	RANS	2D	400K	100

Figure 3.18: Comparison of current chamber wall heat flux results and those of Tucker et al. [115]. See Table 3.9 for descriptions of Cases 1 and 5.

The two zones are blended as shown in Figure 3.19 around the re-attachment point location. Note that this grid adjustment was needed needed only because the code automatically switches to the low-Re model if the y^+ value is smaller than one (see Figure 3.15).

Following this section, an investigation of the effect of turbulence-chemistry interactions and chemical non-equilibrium is performed by comparing the results of the LFRC model and the SLFM for the Pal et al. [116] case. As mentioned in Chapter 2, the SLFM is only implemented in the Loci-Stream code. For consistency of

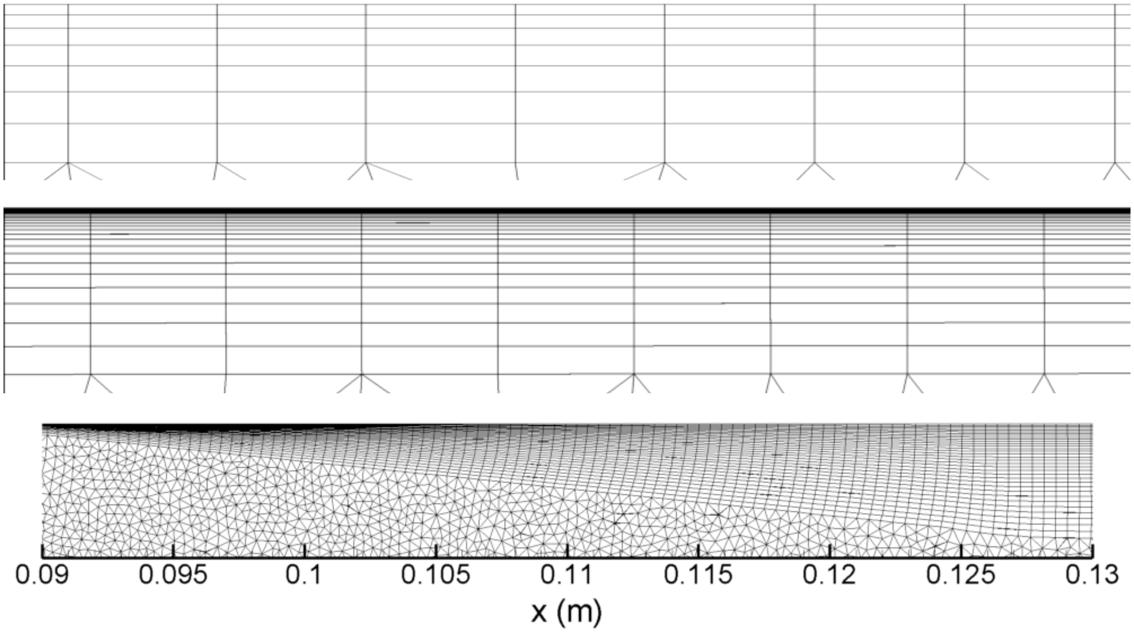

Figure 3.19: Boundary layer discretization. Top: Grid 1, Middle: Grid 2, Bottom: Zonal grid.

comparisons, LFRC model computations presented throughout the rest of this text are also performed with the Loci-Stream code (see Chapter 2). Identical chemistry mechanism, turbulence model and wall treatment options as used in previous analyses are retained. The switch shown in Figure 3.15 also applies.

The effect of the turbulence wall treatment has already been demonstrated to be contained near the wall boundary while the rest of the flow field remains mostly unaffected (see Figure 3.16(a) and Figure 3.16(b) for a comparison of Cases 2 and 3, and Figure 3.17 for temperature and axial velocity profiles at different axial locations). The effect on the wall heat flux distribution, however, is substantial. Cases 2 and 3 (see Table 3.9 for case descriptions) are repeated with Loci-Stream and the zonal wall treatment is tested. The resulting wall heat flux distributions are shown in Figure 3.20(a) in comparison to the experimental data while Figure 3.20(b) shows the corresponding y^+ distributions for the first grid cell center off the wall. On the figures, beginning and end of the grid blending region (see Figure 3.19) as well as the

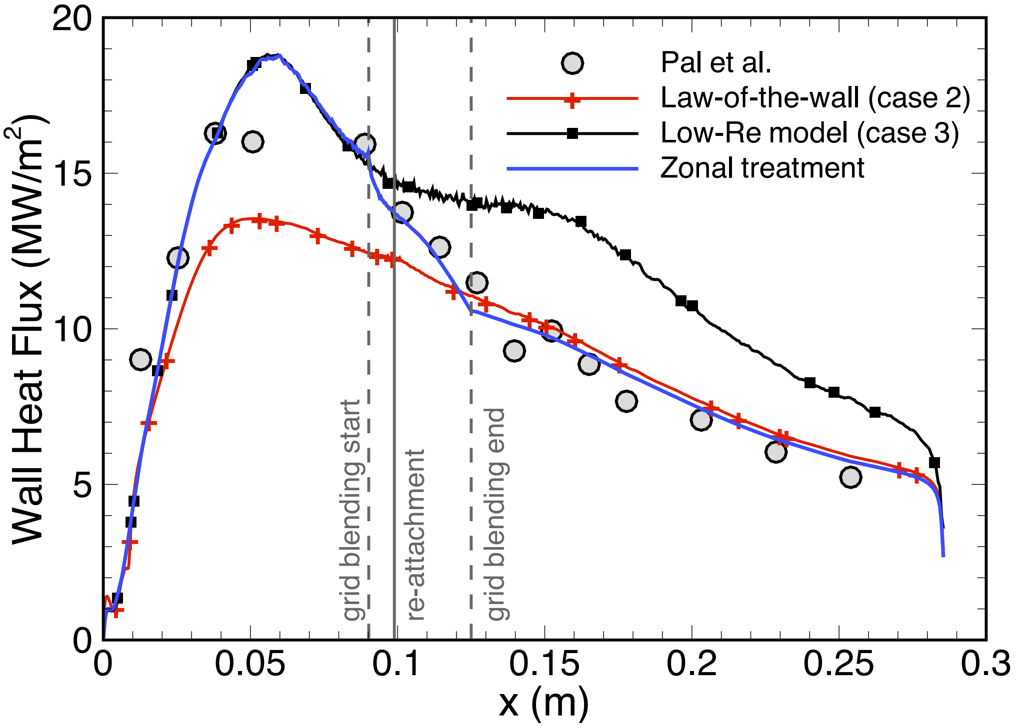

(a) Wall heat flux distibutions.

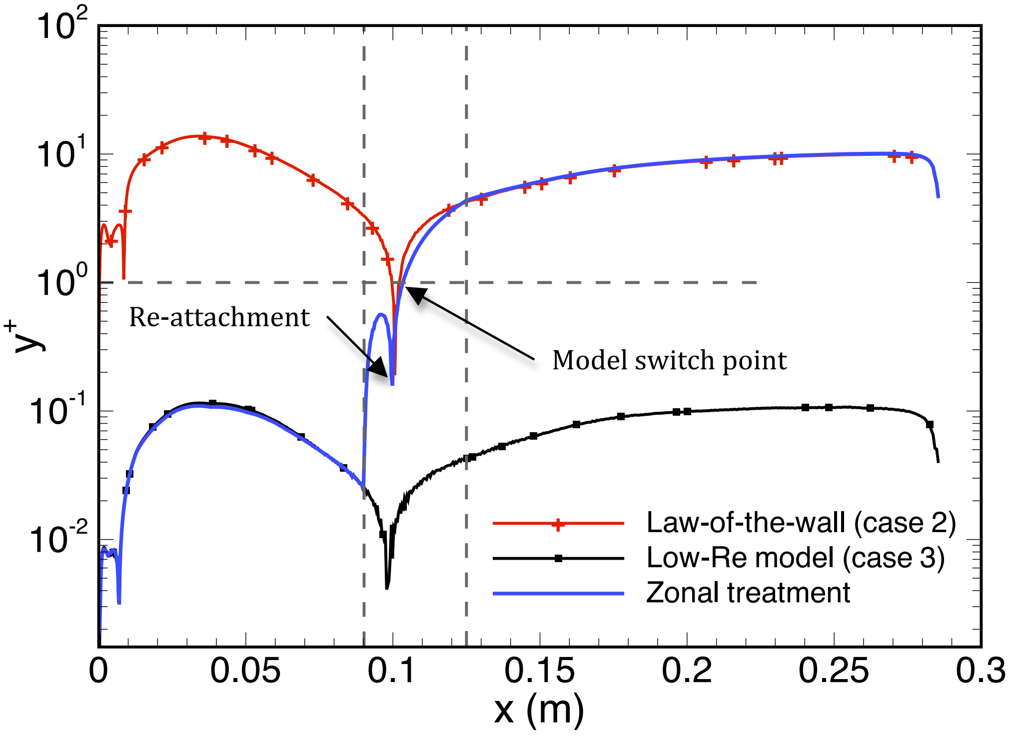

(b) Corresponding y^+ distributions for the first grid cell center off the wall.

Figure 3.20: Effect of turbulence wall treatments on the chamber wall heat flux distribution. See Table 3.9 for descriptions of Cases 2 and 3.

location of the re-attachment point are indicated. Note that the exact re-attachment point location slightly varies between the solutions with different wall treatments as can be observed via the dips in y^+ distributions shown in Figure 3.20(b). Also note that the zonal treatment's switch from the low-Re model to the law-of-the-wall does not precisely occur at the point of re-attachment. Rather, the switch occurs at a point where the y^+ value first exceeds unity, slightly after the re-attachment point. Fig 3.21 shows the near wall axial velocity and temperature profiles at the beginning and end of the grid blending region as well as the re-attachment and model switch points. The zonal treatment profiles match the low-Re model results before the model switch point as expected. After the switch, while the velocity profiles for all solutions are consistent, the temprature profiles begin to differ. The zonal treatment temperature distribution falls in between those of the low-Re model and the law-of-the-wall results.

In the current implementation, switch from the low-Re treatment to the law-of-the-wall formulation occurs abruptly at the point of $y^+ = 1$ for the first grid cell center off the wall. This abrupt switch does not seem to affect the continuity of the heat flux distribution around the switch location (see Figure 3.20(a)). The discontinuities of the slope at the beginning and end of the grid blending region are due to abrupt angling and flattenning of the grid lines.

The zonal treatment result is in good agreement with the measurements through the entire wall heat flux profile. But in the current application, a-priori knowledge of the re-attachment point location and a new corresponding blended wall grid were needed. This issue is only an artifact of the model implementation and can be eliminated with the introduction of a boundary condition which would enforce the use of law-of-the-wall regardless of how low the y^+ value is. Then a fine boundary layer grid (Figure 3.19, middle) can be utilized along the entire chamber wall. The detection of the re-attachment point location, and hence the point of wall treatment switch, can be automated. Furthermore, a blending of the two models can be applied near the

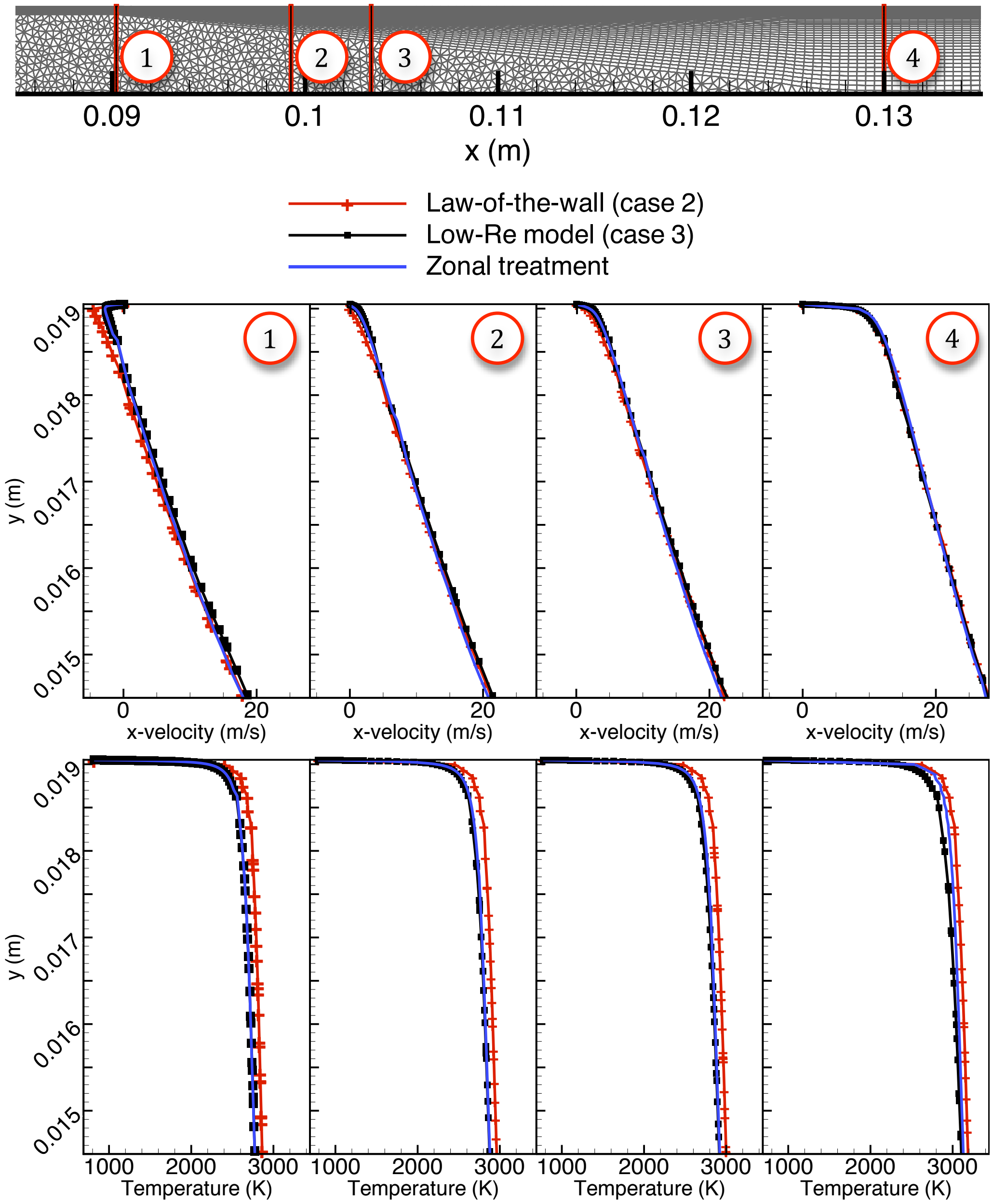

Point	x (m)	
1	0.09	Grid blending start
2	0.099	Re-attachment point for zonal treatment
3	0.103	Model switch point ($y^+ = 1$)
4	0.13	Grid blending end

Figure 3.21: Near wall velocity and temperature profiles for different near wall turbulence treatments.

Table 3.10: Numerical test conditions for flamelet model comparisons.

Case	**Model**	**Wall Thermal BC**	Z **PDF**	χ **PDF**	**Exit BC**	Le	Sc	Le_t	Sc_t
3	LFRC	Experimental distribution	-	-	Supersonic	-	-	1.36	0.95
3A	LFRC	Adiabatic	-	-	Fixed pressure	-	-	1.36	0.95
3B	LFRC	Adiabatic	-	-	Fixed pressure	1	1	1	1
F1	SLFM	Adiabatic	β	lognormal	Fixed pressure	1	-	1	0.95
F2	SLFM	Adiabatic	β	$\chi \rightarrow 0$	Fixed pressure	1	-	1	0.95
F3	SLFM	Adiabatic	δ	$\chi \rightarrow 0$	Fixed pressure	1	-	1	0.95
F4	SLFM	Adiabatic	δ	δ	Fixed pressure	1	-	1	0.95
F5	SLFM	Adiabatic	δ	δ	Fixed pressure	1	1	1	1

switch to ensure a smooth transition.

3.4 Turbulence-Chemistry Interactions and Non-equilibrium Chemistry

The computational results presented in this chapter thus far were carried out with the LFRC in which the transport equations for mean species mass fractions and enthalpy were explicitly solved but the effect of turbulent fluctuations on chemical reaction rates were omitted due to the difficulties outlined in Chapter 2. Also in Chapter 2, several different modeling approaches for turbulent closure of reaction rates were discussed and the SLFM was described in detail. SLFM is implemented in the Loci-Stream code and simulations for the Pal et al. [116] case were performed in order to quantitatively characterize the effects of turbulence-chemistry interactions and non-equilibrium chemistry.

The conditions for the numerical test cases discussed in this section are summarized in Table 3.10 and temperature contours corresponding to each case are presented in Figures 3.22 and 3.23 for qualitative comparison. In all simulations, identical chemistry mechanisms (6s8r, see Table 3.2) were used. Grids were also identical (Grid 2, see Table 3.9) except that the exit nozzle was excluded for all of the cases other than Case 3. Instead, a fixed pressure outlet boundary condition (54.2 bars, as listed in Table 3.3) was imposed.

In the following section, the results of the simulations listed in Table 3.10 are analyzed comparatively to assess:

- Equivalency of the LFRC and SLFM models under similar assumptions.
- Effect of chemical non-equilibrium
- Effect of turbulence-chemistry interactions

3.4.1 LFRC Model vs. SLFM

The main underlying differences between the LFRC model and the SLFM are:

1. SLFM does not account for wall heat transfer and in effect, adiabatic wall boundary condition is used.
2. SLFM accounts for turbulence-chemistry interactions while the LFRC model does not.
3. In the current SLFM formulation, a unity Lewis number, $Le = 1$, is used for all the species, i.e. diffusivities for each species are the same and equal to the thermal diffusivity.

More detailed discussions regarding these items are provided in Chapter 2. To facilitate meaningful discussions about the effect of turbulence-chemistry interactions via comparison of the two model results, equivalency of them under a similar assumption set need to be established first.

As determined from the LFRC simulations with imposed wall and face plate temperatures, around 45% of the energy released via the reactions is lost through the

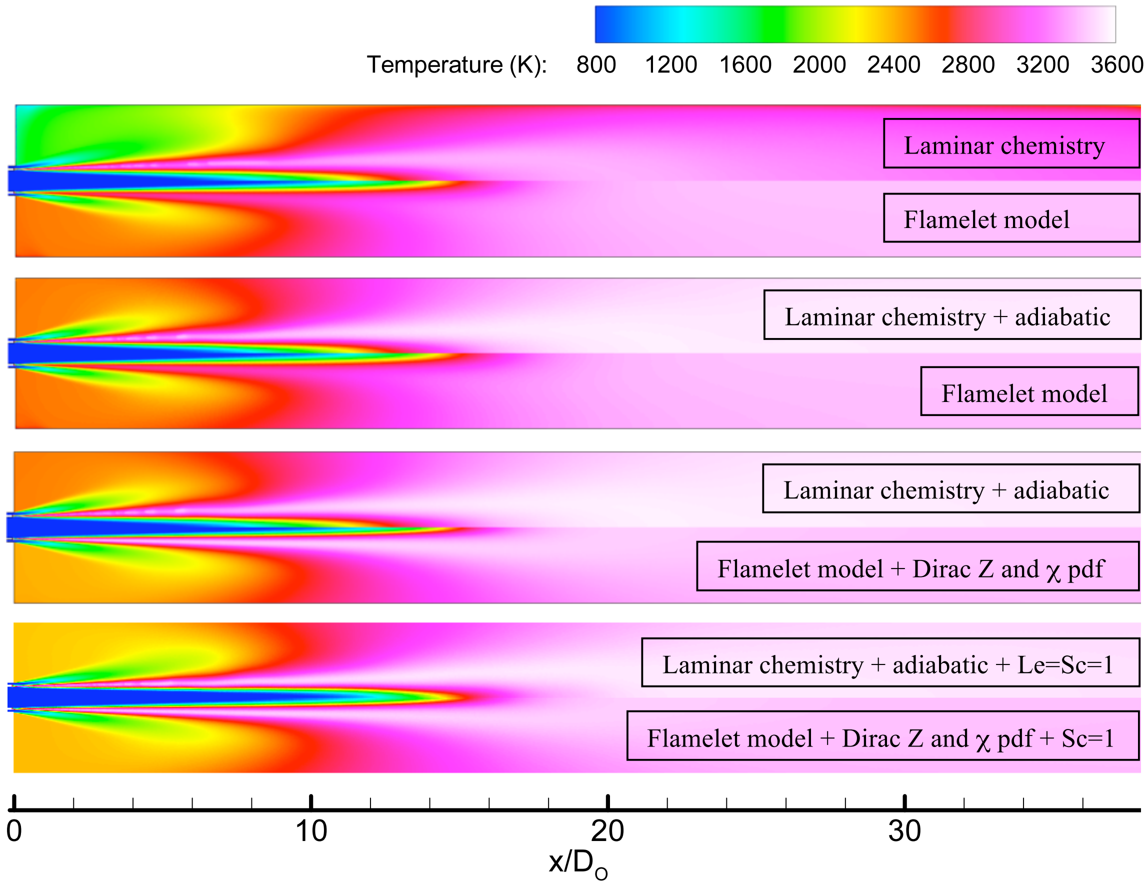

Figure 3.22: Temperature contours obtained with LFRC and SLFM for Pal et al. [116] case.

walls while the rest exits through the outlet. Therefore, the choice of an imposed temperature distribution vs. an adiabatic wall condition can be expected to have a significant impact not only confined to the near wall region. This can in fact be verified by inspection in Figure 3.22 of the LFRC result with an imposed wall temperature distribution (top row, upper half) and the LFRC results with adiabatic wall conditions (2^{nd} row, upper half). Heat loss through the wall has an especially more pronounced cooling effect in the recirculation zone in the upper left corner of the domain. Hence, the Case 3 (imposed wall temperature, LFRC) result is not further compared to the flamelet model simulations.

The SLFM, in comparison to the adiabatic LFRC model simulation (Figure 3.22, 2^{nd} row), produces a noticeably lower mean temperature field near the flame region. Furthermore, the oxygen core extends further downstream in the SLFM simulation indicating slower mixing and hence a larger flame length. When the turbulence-chemistry interaction effect in the SLFM is effectively turned off by utilizing a Dirac-δ PDF distribution, similar temperature fields are observed (Figure 3.22, 3^{nd} row) while the flame length discrepancy persists. The turbulence-chemistry interaction effect will be further discussed in the following sections.

Note that in simulations with both models, a turbulent Schmidt number of $Sc_t = 0.95$ was used. While a turbulent Prandtl number of $Pr_t = 0.7$ is used for the LFRC model simulations, SLFM simulations correspond to $Pr_t = Sc_t$ because of the assumption of $Le = 1$ (see Table 3.10). For the results shown in Figure 3.22 (last row), laminar and turbulent transport properties between the two models are matched:

$$Le = Le_t = Sc = Sc_t = 1$$

This comparison (with adiabatic walls, no turbulence-chemistry interactions and equal transport properties for both models) eliminates the fundamental model differences and very similar results are observed as expected.

3.4.2 Non-equilibrium Chemistry Effect

As detailed in Chapter 2, transport equations for the averaged conserved scalar mixture fraction, $\widetilde{Z}$, and its mean variance, $\widetilde{Z''^2}$, are solved in the flamelet model. The mean scalar dissipation rate, $\widetilde{\chi}$, which has the units of $1/s$ and can be seen as an inverse diffusive time scale, is modeled (Equation 2.74). The scalar dissipation rate represents the non-equilibrium chemistry effects. In the limit of $\chi \to 0$, chemistry is infinitely fast compared to the diffusion and hence the propellants attain chemical

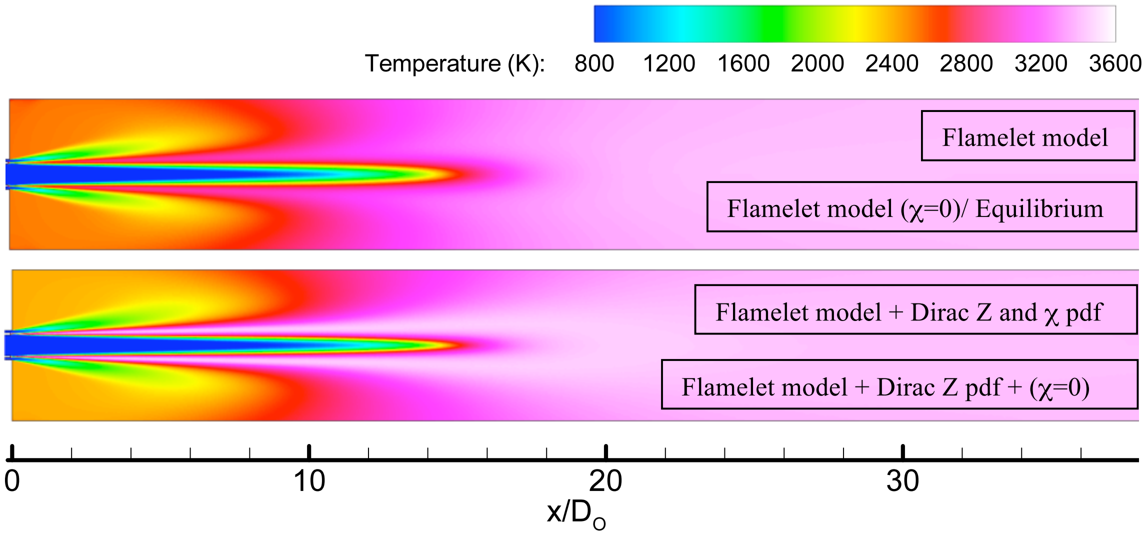

Figure 3.23: Effect of non-equilibrium chemistry.

equilibrium immediately upon mixing. As χ increases, diffusion time scale becomes comparable to the chemistry time scale and eventually the heat is carried out of the reaction zone at a faster rate than its generation via the chemical reactions. This in turn causes the extinguishing of the flame (quenching).

In the 1^{st} row of Figure 3.23 the flamelet model solution is compared to the solution in which χ is taken as zero (equilibrium). In this isolated look into the effect of non-equilibrium chemistry, no identifiable difference in the temperature field is observed. The same observation holds true for the simulations with or without the non-equilibrium effects in the absence of turbulence-chemistry interactions (achieved via the Dirac-δ PDF, see the 2^{nd} row of Figure 3.23). Thus, the chemical non-equilibrium effect was unimportant both with and without the presence of turbulence-chemistry interactions.

In Figure 3.24, laminar flamelet solutions parameterized with χ_{st} are plotted. The effect of the scalar dissipation rate is negligible for $ln(\chi_{st}) < 8$. As shown in the mean scalar dissipation rate contours in Figure 3.25 as well as the values probed in Figure 3.27, the region where $ln(\chi_{st}) < 8$ is confined to a small area near the injector exit where the strong shear layer between the fuel and oxidizer streams yield a diffusive time scale small enough to interact with the chemical reaction rates. The lack of non-equilibrium chemistry effects is often the case for hydrogen flames due to the fast chemistry as noted by Peters [52] referring to the experimental study by Barlow et al. [121]. This was also demonstrated in the chemistry time scale analysis performed for the Vaidyanathan et al. [117] injector case in this chapter. Cheng and Farmer [111] simulated two different LOX/GH_2 single element experimental injectors and their finite-rate and equilibrium chemistry computation results were only slightly different. Since the non-equilibrium chemistry plays no noticeable role in the current investigation, the flamelet model essentially becomes the same as that of the assumed PDF chemical equilibrium model discussed in Correa and Shyy [68].

As mentioned earlier, a large enough scalar dissipation rate will eventually result in flame quenching. Although the scalar dissipation rate attains large values near the injector exit region, the quencing limit was not approached in the entire flow field.

3.4.3 Turbulence-Chemistry Interaction (TCI) effect

The comparisons presented in 2^{nd} and 3^{rd} rows of Figure 3.22 provide a more objective look into the TCI effects. In the 2^{nd} row, both simulations were performed with adiabatic wall conditions while only the flamelet model (Case F1) accounts for turbulent closure of reaction rates. In the 3^{rd} row, the TCI effect in the flamelet model (Case F4) was effectively turned off by utilizing a Dirac-δ PDF distribution for both Z and χ. An immediate observation is that the flamelet model yields a consistently lower mean temperature field while the discrepancy is greater near the flame surface (The flame surface is depicted in solid black line in Figure 3.25). When the TCI effect is turned-off, however, the temperature field becomes more comparable to the laminar chemistry model solution (Case 3A).

Radial temperature profiles at several axial locations obtained with the LFRC

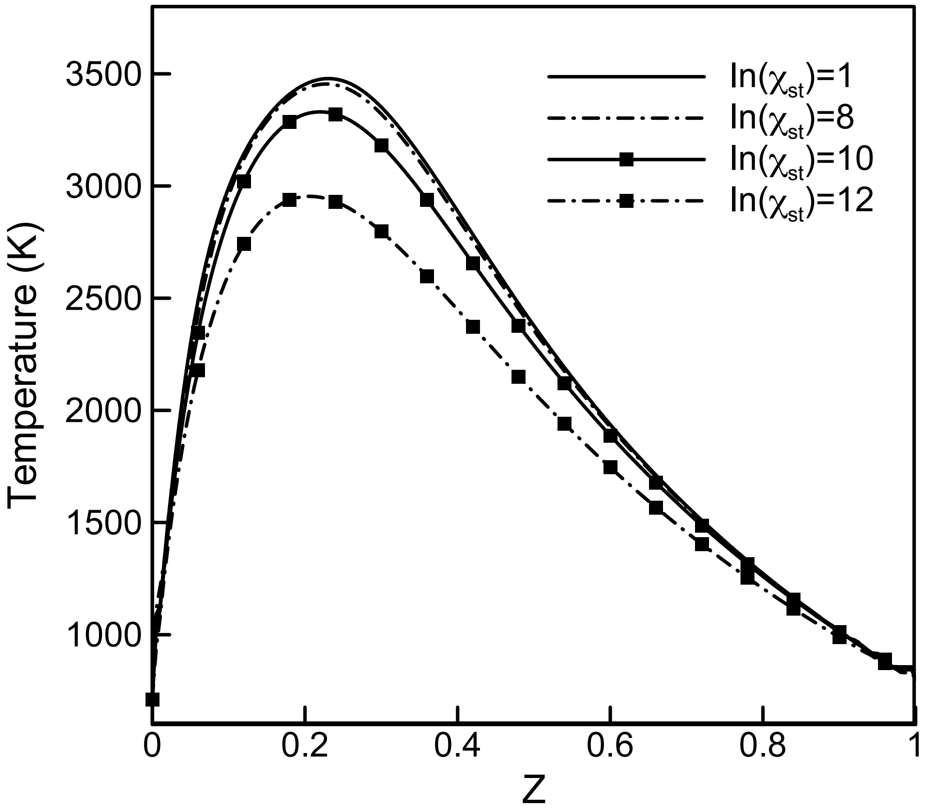

Figure 3.24: Laminar flamelet temperature profiles for varying stoichiometric scalar dissipation rates.

model, SLFM and SLFM with disabled turbulence-chemistry interactions (via utilizing Dirac-δ PDF distributions for both Z and χ) are given in Figure 3.26. The latter simulation is denoted as SLFM-δ in the following discussions. β and lognormal PDF distributions for Z and χ respectively for several representative points are given in Figure 3.27. The probe points are also marked in Figure 3.26.

The LFRC and SLFM-δ simulations both consider the non-equilibrium chemistry effect (shown already to be unimportant in this case) and they both disregard the turbulence-chemistry interactions. Thus ideally, similar outcomes are expected in simulation results. Instead, it can be seen that throughout the profiles at $x/D_0 = 2$ to $x/D_0 = 15$, the SLFM-δ yields slightly larger peak temperatures with less spread. In addition, at these locations the core temperatures are significantly lower in SLFM-

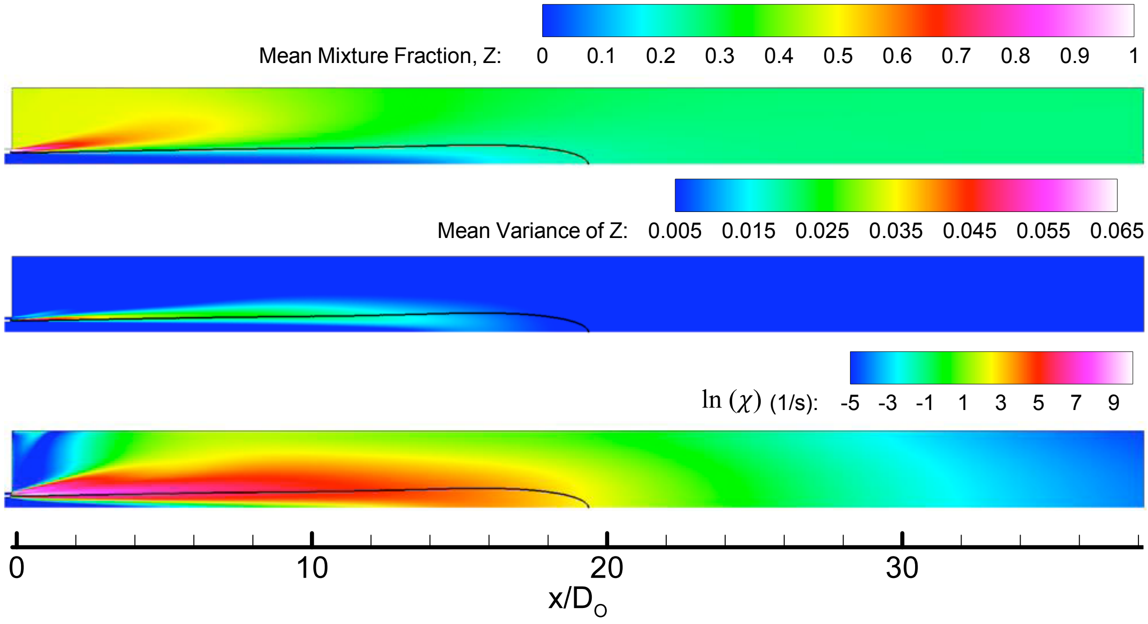

Figure 3.25: Flamelet model solution (F1) contours. Solid black line indicates stoichiometric mixture fraction (flame surface) at $Z = 0.229$.

δ results. The discrepancies are attributed to the difference of laminar and turbulent transport properties in the two models as discussed in Section 3.4.1.

Having ruled out the effects of the scalar dissipation rate and hence the non-equilibrium chemistry in the flamelet model (Section 3.4.2), the extent of the TCI can be described by the assumed β PDF distribution of the mixture fraction Z and hence can be observed by comparing the SLFM and SLFM-δ simulation results in Figures 3.22 and 3.26. The PDF distributions at several points (as marked in Figure 3.26) are given in Figure 3.27. The skew and width of the β PDF for the mixture fraction is determined by its mean, $\widetilde{Z}$, and its mean variance, $\widetilde{Z''^2}$, respectively. The mean scalar dissipation rate, $\widetilde{\chi}$, is also directly related to the mean mixture fraction variance via the modeling relation given in Equation 2.74. As shown in Figure 3.25, both $\widetilde{Z''^2}$ and $\widetilde{\chi}$ are only significant near the mixing layer between fuel and oxidizer streams, and hence near the stoichiometric flame surface shown as the black line. They take their largest value upstream near the injector post tip whereas both re-

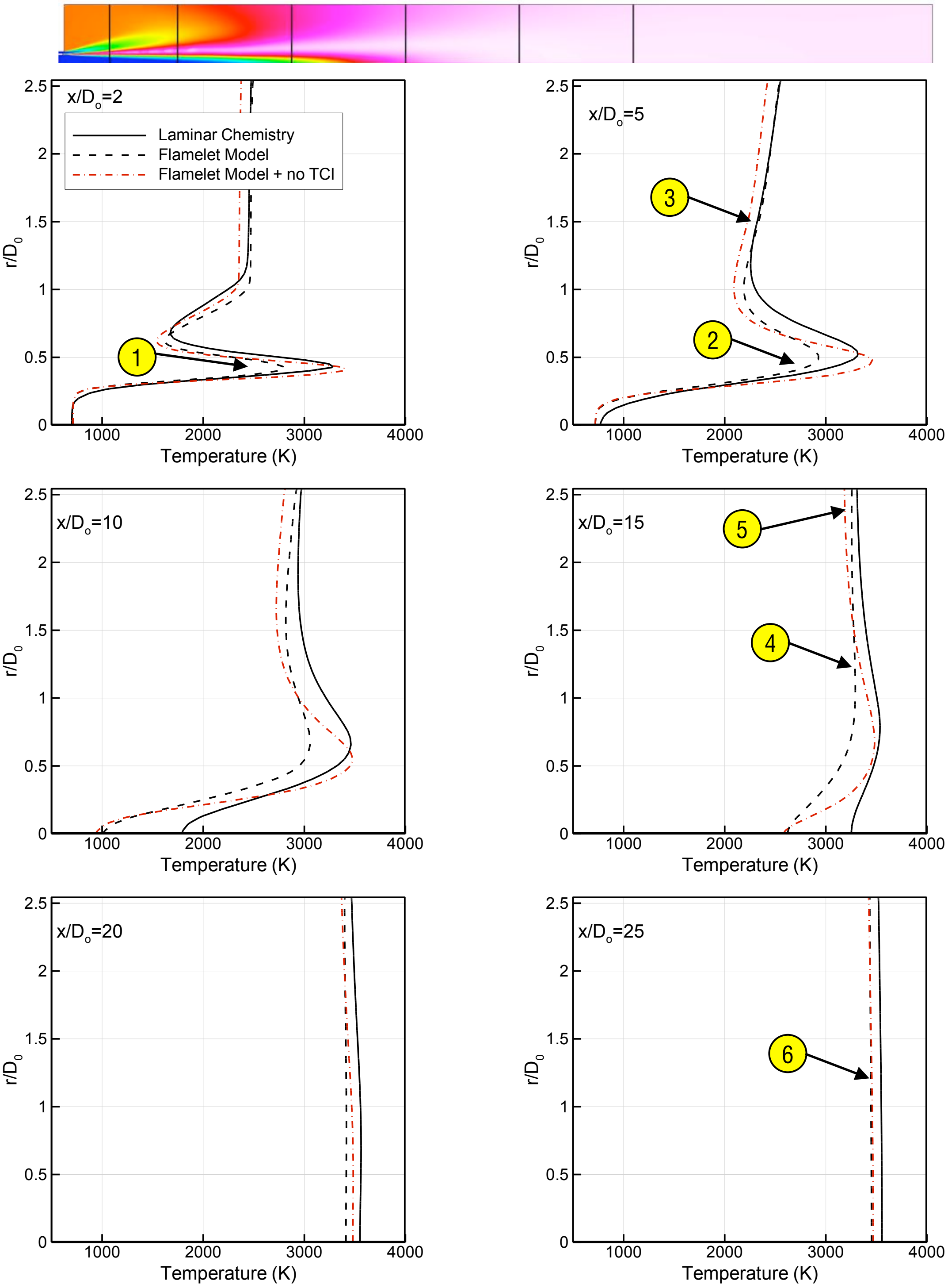

Figure 3.26: Comparison of temperature profiles of laminar finite rate chemistry and flamelet solutions at different axial locations. PDF distributions corresponding to the numbered locations are given in Figure 3.27.

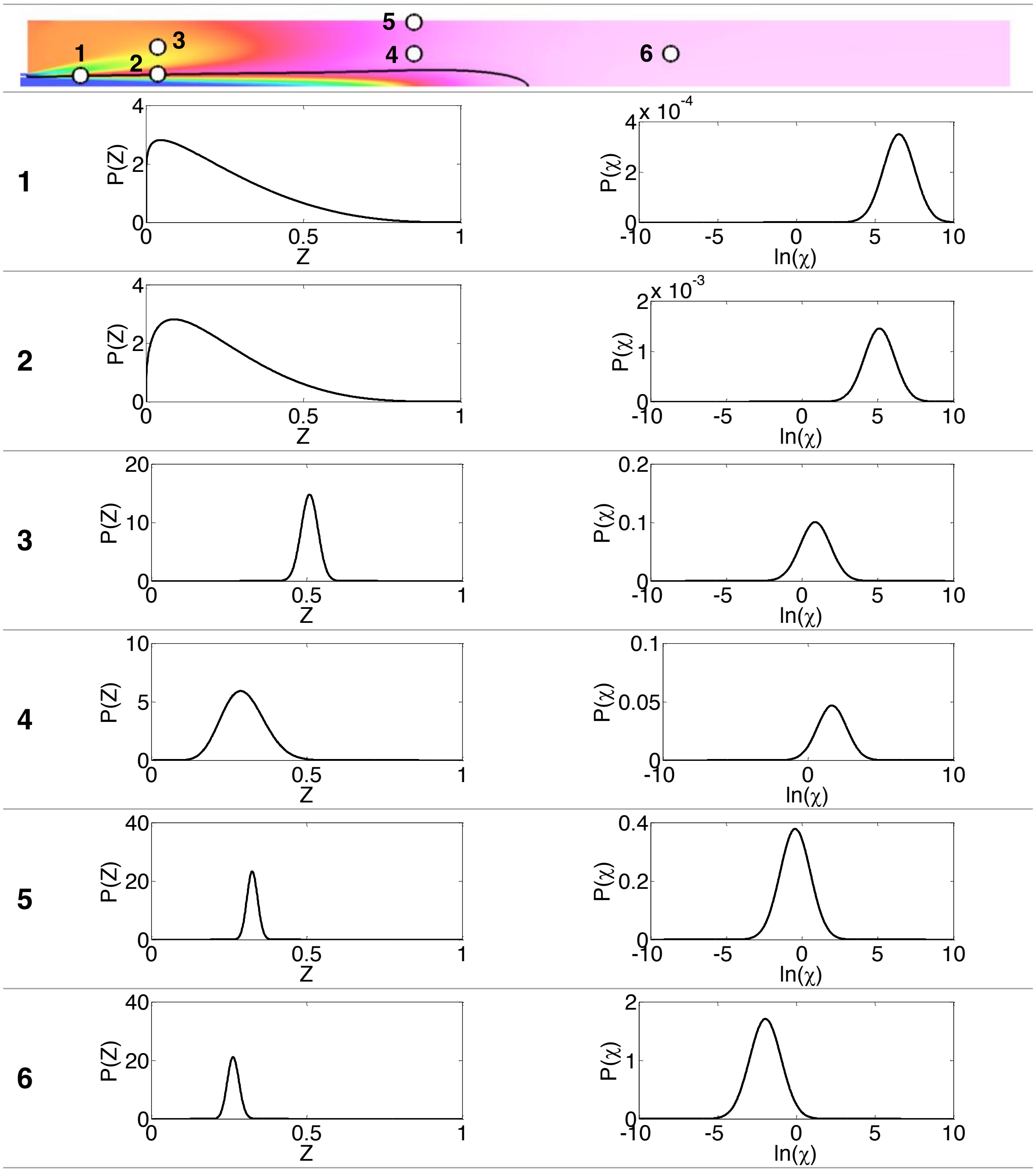

Point	x/D_0	r/D_0	$\widetilde{Z}$	$\widetilde{Z''^2}$	$ln(\widetilde{\chi})$
1	2	0.41	0.23	3.1E-2	8.0
2	5	0.4615	0.23	2.6E-2	6.6
3	5	1.5	0.51	7.3E-4	2.4
4	15	1.25	0.30	4.5E-3	3.1
5	15	2.45	0.32	2.9E-4	1.0
6	25	1.25	0.26	3.6E-4	-0.45

Figure 3.27: PDF distributions of mixture fraction and scalar dissipation rate at selected points in the combustion chamber.

duce towards downstream as the mixing layer diffuses. At all x/D_0 locations, the β distribution causes reduced temperatures near the stoichiometric flame surface but slightly increased temperatures away towards the wall. The effect of the PDF at this latter point (see probe point 3 in Figures 3.26 and 3.27) is negligible because of the more or less uniform local mixture composition and as a result, a small mixture fraction variance and hence a narrow PDF. Note that the usage of the β PDF for mixture fraction not only affects the temperature field but the density field and the distribution of the transport properties as well. Consequently, the resulting mixture composition field is altered depending on the choice of the PDF. As shown in Figure 3.28, when a Dirac-δ PDF is used, the mixture fraction value in the recirculating region is slightly larger, meaning a composition richer in hydrogen and a cooler thermal field. Near the flame surface, however, a large gradient of the mixture fraction exists. Corresponding large mixture fraction variance yields a wide β PDF as shown for probe points 1 and 2. Thus, the reduced peak temperature near this region is largely due to the consideration of TCI. Probe point 5 corresponds to a point near the edge of the boundary layer. There, the narrow PDF distribution points to negligible TCI effects. This holds true for any region away from the flame surface. Therefore, convergence of the temperature profiles further downstream after the closing of the flame surface is observed for locations $x/D_0 = 20, 25$.

The axial adiabatic wall temperature distributions for the LFRC and SLFM (β and lognormal PDFs for Z and χ) simulations are given in Figure 3.29. The difference in temperature is at most 3% consistent with the previous analysis because the wall is far from the flame surface.

3.5 Summary and Conclusions

Two different experimental GO_2/GH_2 single element shear coaxial injectors due to Vaidyanathan et al. [117] and Pal et al. [116] were modeled and tested with a

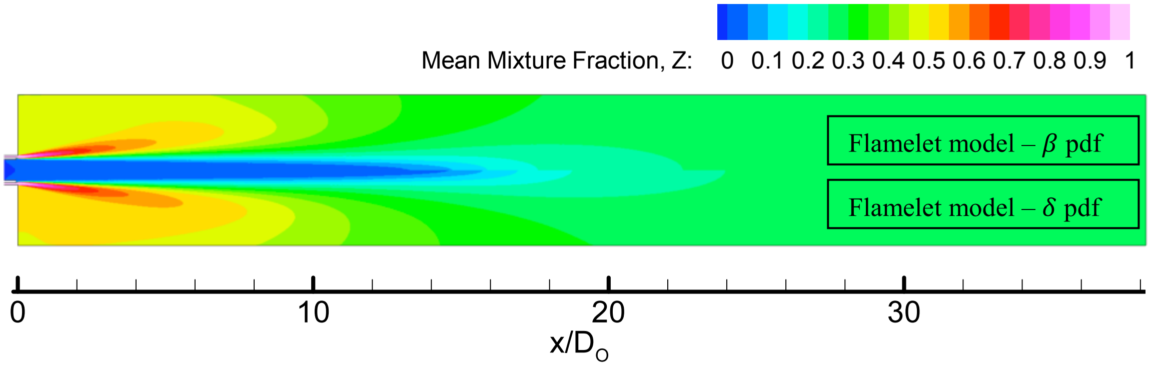

Figure 3.28: Mixture fraction fields for the flamelet models solutions with a β PDF (top half) and with a Dirac-δ PDF (bottom half).

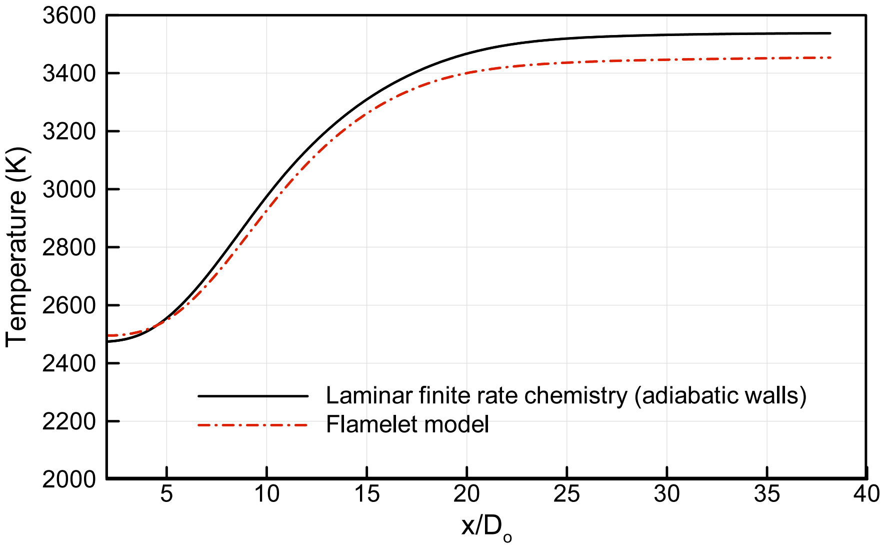

Figure 3.29: Adiabatic chamber wall temperature distribution for LFRC and SLFM simulations.

CFD framework based on RANS turbulence closure and laminar finite-rate chemistry model. Impacts of grid refinement, different choices of chemistry mechanisms, wall temperature boundary conditions and near wall turbulence treatments were assessed. The Pal et al. [116] case is also simulated with the steady laminar flamelet model to assess the effects of turbulence-chemistry interactions and non-equilibrium chemistry.

In both test cases, grid refinement resulted in a reduced mixing rate and hence a downstream shift of the flame. Effect of the refinement on wall heat flux profiles were less pronounced. Vaidyanathan et al. [117] injector was more extensively tested for this aspect with 5 different grid resolutions and convergence to a grid insensitive level was demonstrated.

Four different chemistry mechanisms were selected and tested for the Vaidyanathan et al. [117] injector whereas two of them were evaluated for the Pal et al. [116] injector. The simulation results were identical for the former injector whereas a minimal difference is observed for the latter one. Time scales of each reaction mechanisms were investigated in an analysis of introducing additional O_2 to an equilibrium condition and examining the time history of the response. It was noted that with a detailed treatment of turbulence-chemistry interactions, choice of the chemistry mechanism can make a larger impact on the outcome [68].

The Pal et al. [116] injector case was also tested for different choices of combustion chamber wall temperature boundary conditions and near wall treatment of turbulence. Imposing a uniform wall temperature versus using the experimentally measured temperature distribution didn't cause a noticeable effect in the flow field. Wall heat flux distribution was slightly affected but in an integral sense, total heat transfer to the wall was unchanged.

Use of the law-of-the-wall method versus integrating to the wall with a refined wall boundary layer grid distribution (low-Re model) by far had the largest impact on wall heat flux predictions in our tests. Former approach was shown to yield a better agreement with experimental wall heat flux distribution where the flow is attached to the wall. In the recirculation region, however, the latter approach performed better. Advantages and shortcomings of each approach were discussed. Based on these discussions and the observed results, a zonal wall treatment was proposed. The low-Re model is used at the recirculating flow region while the law-of-the-wall method is used elsewhere. This treatment showed considerable improvement in the overall wall heat flux distribution prediction.

Wall heat flux results for the Pal et al. [116] injector case were compared to those of Tucker et al. [115] who employed various CFD methodologies ranging in computational cost to simulate the same problem. The scatter between the various efforts is substantial (except for the case with very large number of grid points using LES, which shows consistently better agreement than other studies). The current RANS methodology, which would represent the lowest computational cost compared to those reported in Tucker et al. [115], provided comparable results. The zonal wall treatment option proposed herein, however, yielded excellent agreement with the experimental data throughout the chamber wall.

The effects of turbulence-chemistry interactions (TCI) and non-equilibrium chemistry were investigated for the Pal et al. [116] injector case by comparing the adiabatic wall simulation results of the LFRC model and the SLFM with:

1. β PDF for Z, lognormal PDF for χ,
2. β PDF for Z while $\chi \rightarrow 0$ is explicitly imposed (assumed PDF/equilibrium model),
3. Dirac-δ PDF for both Z and χ,
4. Dirac-δ PDF for Z while $\chi \rightarrow 0$ is explicitly imposed.

The first simulation accounts for both TCI and chemical non-equilibrium effects, while the former is shut down for the 2^{nd} and the 4^{th}. Both effects are shut down for the 3^{rd} simulation. Regardless of the consideration of TCI, the non-equilibrium chemistry effect was shown to be unimportant consistent with the chemistry mechanism tests and the time scale analysis for the Vaidyanathan et al. [117] case performed using the LFRC model. Cheng and Farmer [111] also reported only slight differences between their results obtained with the finite-rate and equilibrium chemistry models in the context of a LOX/GH_2 single element injector simulation. Similar to the work of

Correa and Shyy [68], we find that for the O_2/H_2 injector type problems such as those presented herein, the assumed PDF/equilibrium model is of sufficient fidelity to resolve turbulence-chemistry interactions without the need of accounting for the chemical non-equilibrium within the flamelet model.

The temperature profiles at several axial locations and PDF distributions at select representative points in the high shear region, recirculating region, near the chamber wall and away from the flame surface were inspected. In the absence of chemical non-equilibrium effects, the TCI is governed by the local mean and variance of Z, in the form of an assumed PDF. The width of the PDF is determined by the mean variance of Z. Hence in regions with large variations in mixture composition coupled with highly turbulent flow, such as near the flame surface, TCI effect is prominent while it diminishes with the distance from the flame surface. In the single element injector configuration of Pal et al. [116], flame surface lies far from the wall and the TCI effect doesn't alter the wall temperature distribution significantly. However this is only due to this particular single element injector test case setup. In realistic multi-element injectors where an array of injector elements are typically placed close to the chamber wall, the turbulence-chemistry interactions may be expected to have a considerable effect in wall heat flux predictions.

CHAPTER IV

Validation and Parametric Element Configuration Assessment of a Multi-Element Injector

Single element injector analyses such as those presented in Chapter 3 yield valuable insight into the flow physics and the performance of the numerical models used. However, in practical liquid rocket engines, a large number of injector elements, typically arranged in concentric circles are utilized. For example, the space shuttle main engine (SSME) uses 525 injector elements (see Figure 1.4). The interactions between individual elements play an important role in fuel/oxidizer mixing characteristics and combustion chamber thermal environment. In this study, an experimental 7 element injector configuration due to deRidder et al. [122; 123; 124] is taken as a basis for a two-fold objective:

1. To validate the CFD capability for multi-element injectors.
2. To conduct a parametric assessment of element arrangements by varying radial and circumferential element-to-element distances.

Loci-Stream code [22; 23; 24] with both the Laminar Finite-Rate Chemistry (LFRC) model and the Steady Laminar Flamelet Model (SLFM) is utilized in the analysis to examine the flow features along with the extent of the turbulence-chemistry interaction effects. The description of the code as well as the models mentioned are given in

Chapter 2. A major shortcoming of the SLFM used herein is that the wall heat loss is not considered and adiabatic wall boundary conditions are used. In liquid rocket applications, wall heat transfer is an essential outcome of the simulations. To alleviate this difficulty, we propose a method where the adiabatic solution near the wall is represented by the law-of-the-wall formulation. This is done as a post processing step in order to establish the thermal boundary layer. This can be expected to provide a reasonable estimate if the effect of the heat loss is limited to a thin layer near the wall and it does not affect the rest of the flow field significantly. LFRC simulations show that for the multi-element injector case to be presented here, the amount of the heat loss through the wall is only about 1% of the overall energy generated via the combustion. Thus, the previous assumption may be invoked. The resulting wall heat flux distribution is presented in comparison to the LFRC outcome and experimental measurements. Near wall velocity and temperature profiles are also shown to describe the methodology in detail.

In the parametric study, the injector configuration due to deRidder et al. [122; 123; 124] is taken as a basis. The number of outer row injector elements as well as the radius of the outer row are varied and corresponding changes in the flame length and the adibatic wall temperature is observed.

4.1 Multi-Element Injector

In a recent study, deRidder et al. [122; 123; 124] presented experimental measurements of axial and circumferential combustion chamber wall heat flux profiles for a gaseous H_2/ liquid O_2 combustor with a 7 element injector. The combustion chamber was instrumented with 88 thermocouples arranged in coaxial pairs distributed along inline and offline planes and the intermediate plane (see Figure 4.1). Three of the pairs were placed on the face plate. Each pair measures temperature at the inner surface of the combustion chamber and at 0.25 inches outwards.

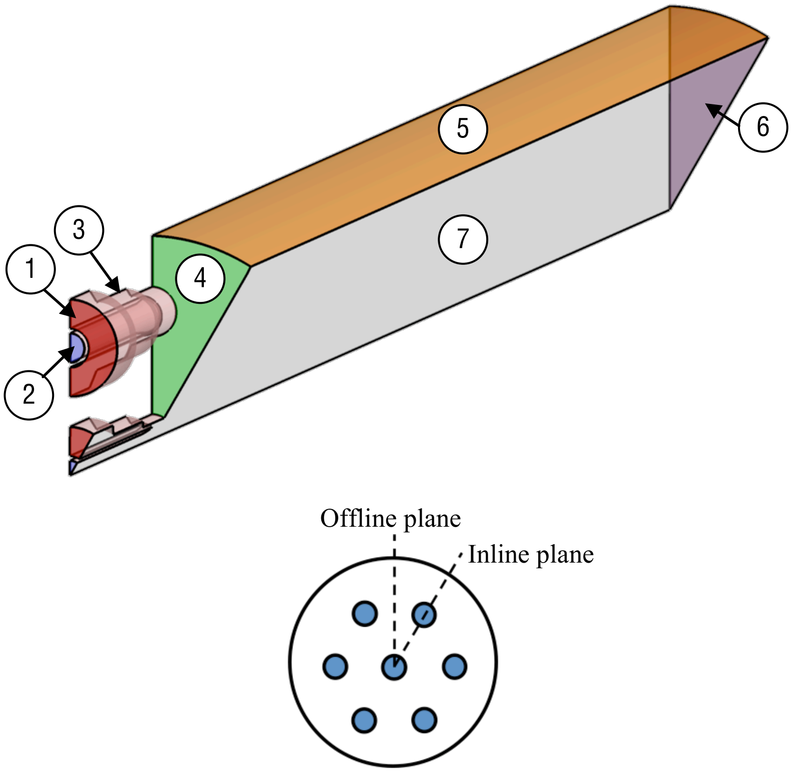

Label	Condition
1	Fuel inlet
2	Oxidizer inlet
3	Injector nozzle walls: No-slip, adiabatic
4	Face plate: No-slip @ 450 K or adiabatic
5	Chamber wall: No-slip @ 750 K or adiabatic
6	Outlet: Fixed pressure
7	Symmetry

Figure 4.1: Computational domain and boundary conditions for the multi-element injector case due to deRidder et al. [122; 123; 124].

Exploiting the symmetric nature of the problem, a 1/12th slice of the combustor is modeled which includes a $1/12^{th}$ section of the core element and a half of an outer element. Details of the computational domain and boundary conditions as well as the experimental case details are provided in Figure 4.1 and Table 4.1 respectively.

Time history of a sample thermocouple pair reading and corresponding wall heat flux are plotted in Figure 4.2. In the experimental procedure, LOX alone was run through the combustion chamber for a long time for pre-chilling. Following the in-

Table 4.1: Multi-element injector test case details.

	Chamber pressure (bars)	56.7
	Oxidizer post inner diameter (mm)	4.93
	Fuel post inner diameter (mm)	6.50
	Fuel post outer diameter (mm)	8.28
	Outer elements row radius (mm)	21.34
	Chamber radius (mm)	34.04
	Chamber length (mm)	307
Fuel	Total fuel mass flux (g/s)	374.2
	H_2 mass fraction in fuel	1
	Temperature (K)	~300
Oxidizer	Total oxidizer mass flux (g/s)	1134
	O_2 mass fraction in oxidizer	1
	Temperature (K)	~90
	Equivalence ratio (O/F)	5.28
	Fuel/Oxidizer velocity ratio	21
	Oxidizer/Fuel mass flux ratio	3.03
	Fuel Reynolds Number[†]	3E5
	Oxidizer Reynolds Number[‡]	5E6
	Measurements	Wall temperature Wall heat flux

[†] Based on annulus gap height at inlet nozzle exit

[‡] Based on diameter at inlet nozzle exit

troduction of H_2 and ignition, wall temperature rises rapidly but shut down occurs before a steady state wall temperature is reached. However, the wall heat flux value does reach a near steady state. Although Figure 4.2 shows data for only a single pair of thermocouples, this observation holds true for the rest. This leads to an ambiguity in assigning a wall temperature boundary condition in CFD simulations. In the present study, a uniform temperature was imposed on the chamber wall and the face plate as shown in Figure 4.1. In the analysis of a single element injector in Chapter 3, choice of a uniform temperature boundary condition, as opposed to imposing the experimentally measured distribution, was shown to be reasonable.

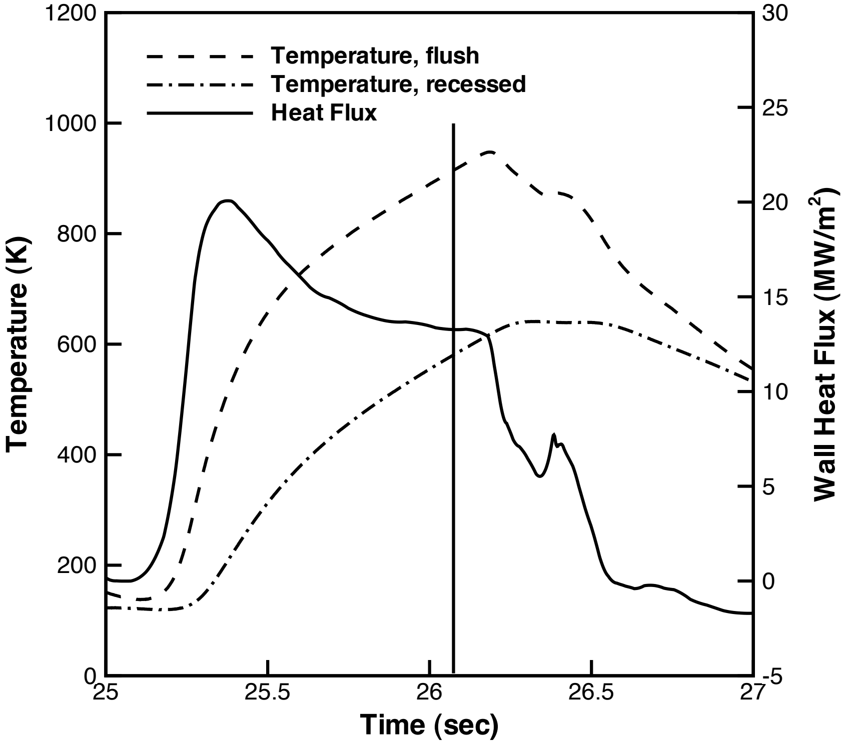

Figure 4.2: Thermocouple pair readings and corresponding heat flux history at 5.5 inches along the combustion chamber measured from the face plate (due to deRidder et al. [122; 123; 124]). Grey line represents the time slice used for validation.

4.2 Computational Grid

A 3D mixed structured/unstructured grid consisting of about 1.2 million cells is used. Boundary layer type stretched hexahedral elements are utilized near the chamber wall, oxidizer inlet nozzle wall and within the fuel inlet nozzle. Tetrahedral cells are used elsewhere. Sample views of the grid are shown in Figure 4.3. 12 layers of hexahedral cells were used for the chamber wall boundary layer. First grid cell center corresponds to $y^+ \approx 20$ while the subsequent cell heights are increased with a relaxation factor of 1.2.

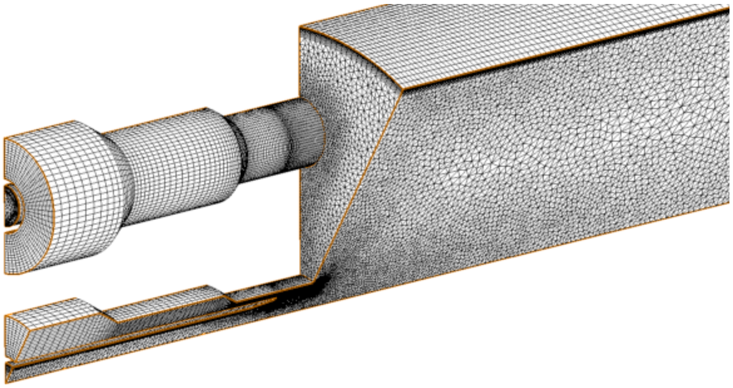

(a) Partial 3D view.

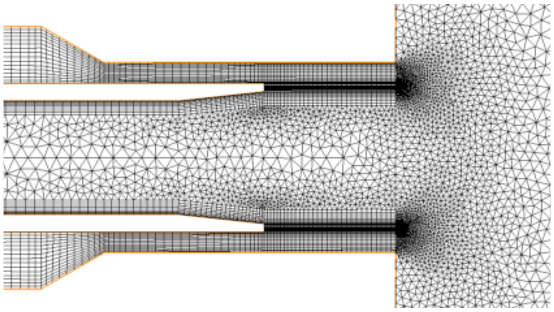

(b) Cut-plane detail of the injector element post

Figure 4.3: Multi-element injector grid.

4.3 Flow Field Based on Different Combustion Models

In the single element injector case studied in Chapter 3, the turbulence-chemistry interaction effect was shown to be constrained to the near flame surface region and the near wall thermal field was essentially unaltered by the effect. In a more realistic injector, large number of injector elements are typically placed in a patterned formation on the face plate. A commonly used arrangement is to place the elements in concentric circular rows. The result is, compared to the single element injectors, a closer proximity of the outer row flame to the chamber wall surface. The significance of the turbulence-chemistry interaction effect on the flow field in general and the near wall region in particalar is investigated in this section.

The multi-element injector setup is tested with both the LFRC model and the SLFM. Details of these modeling approaches are given in Chapter 2 and a comparative assessment in the context of a single element injector is presented in Chapter 3. For the LFRC simulation, the law-of-the-wall approach for the near wall treatment of turbulence was used whereas for the SLFM simulation, the low Reynolds number model was used. In the SLFM computations, adiabatic wall boundary condition is used on all surfaces as required by the model. The uniform temperature chamber wall boundary condition is used in the LFRC simulations. The LFRC model results predict that only 1% of the reaction generated heat is lost through the walls. Thus, even though the two cases have different wall thermal boundary conditions, it is expected that this will have a minimal effect on the overall solution. Note that a portion of the fuel inlet nozzle was excluded in the SLFM simulations due to the geometric constraints encountered in the following parametric study of injector element arrangements. In all the computations presented herein, the 6 species, 8 reactions (6s8r) chemistry mechanism as presented in Table 3.2 is used.

Temperature contours in the inline, intermediate and offline planes for each model simulations are shown in Figure 4.4. Figure 4.5 shows the temperature contours at several axial plane slices as well as the streamline structure. In both figures, solid black lines indicate the stoichiometric flame surface ($Z = 0.111$). Overall, the temperature fields obtained from the LFRC model and the SLFM are in good agreement. However, the latter results in reduction of temperature near the flame surface due to the accounting of turbulence-chemistry interactions through presumed shape probability density functions (PDF) for the mixture fraction and the scalar dissipation rate. The mean mixture fraction, its mean variance and the mean scalar dissipation rate fields are shown in Figure 4.7. Note that although not explicitly shown here, the scalar dissipation rate becomes significantly large only in a small region near the injector posts and thus the non-equilibrium chemistry effect is negligible elsewhere. These immediate observations are consistent with the findings presented in Chapter 3 where a more in-depth comparison of the two models is provided in the context of a

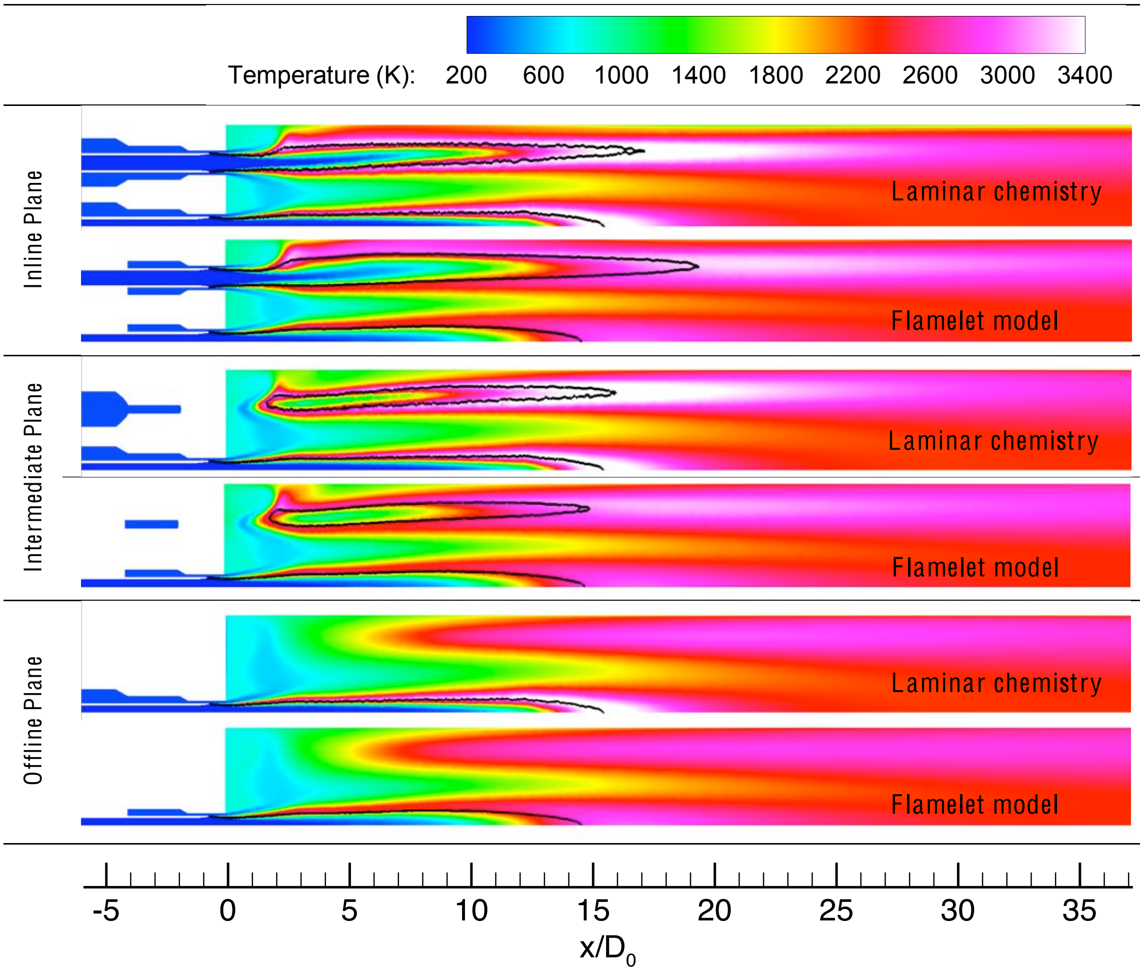

Figure 4.4: Inline, intermediate and offline plane temperature contours for laminar finite-rate chemistry and steady laminar flamelet model computations. Solid black lines indicate the stoichiometric mixture ($Z = 0.111$).

single element injector test case. One notable exception is that for the single element injector case, 45% of the heat generated in reactions was found to be lost through the combustion chamber wall and as a result, the choice of the temperature boundary conditions (adiabatic vs. temperature specification) was shown to have a large impact in the flow field. In the multi-element injector case analyzed here, however, the LFRC simulation reveals that only about 1% of the heat is lost through the walls enclosing the combustion chamber. Therefore, the wall cooling effect, in this case, can be expected to be mostly contained to within a thin layer near the wall.

The streamlines shown in Figure 4.5 (bottom) mostly originate from the upper injector element fuel stream. While a portion of the fuel stream is entrained to the recirculation region between the wall and the injector jet, some escape near the offline symmetry plane and merge to the inline plane further downstream. This fuel rich corridor is shown more clearly in Figure 4.6. This effect can also be observed in the Figure 4.5 temperature contours where a relatively cool layer merges to the inline plane and subsequently diffuses and diminishes further downstream. Note that this layer is thinner and faster diffusing in the flamelet model simulation. Consequently, an increased near wall temperature (compared to laminar finite-rate chemistry simulation) in the vicinity of the inline plane is realized with the flamelet model.

Consistent with the single element injector results (see Chapter 3) of the flamelet model simulations, the effect of turbulence-chemistry interactions is significant mostly near the flame surface and especially near the injector exit where the shear layer between the fuel and the oxidizer streams is stronger. The extent of the turbulence-chemistry interactions is directly correlated with the mean variance of the mixture fraction, $\widetilde{Z''^2}$, as it determines the width of the PDF of the mixture fraction. Contour plots of $\widetilde{Z}$, $\widetilde{Z''^2}$ and $\widetilde{\chi}$ for the inline and offline planes as well as the Z PDF distributions at select points near the wall are shown in Figure 4.7. In both the inline and the offline planes, the PDF width decreases towards downstream. At $x = 0.15\,m$ towards the closing of the near wall flame, and at $x = 0.25\,m$ further downstream, the PDF width is still significant. Despite the significant spread, the mean value of the mixture fraction, Z, at all near wall locations are away from the stoichiometric value of 0.111 (shown as dashed red line in the PDF plots). Thus the influence of the PDF, and hence the local turbulence-chemistry interaction effects, near the wall are small. For the widest PDF shown in Figure 4.7 occurring in the inline plane upstream location, local temperature reduction due to the PDF is about 8 K (0.3%).

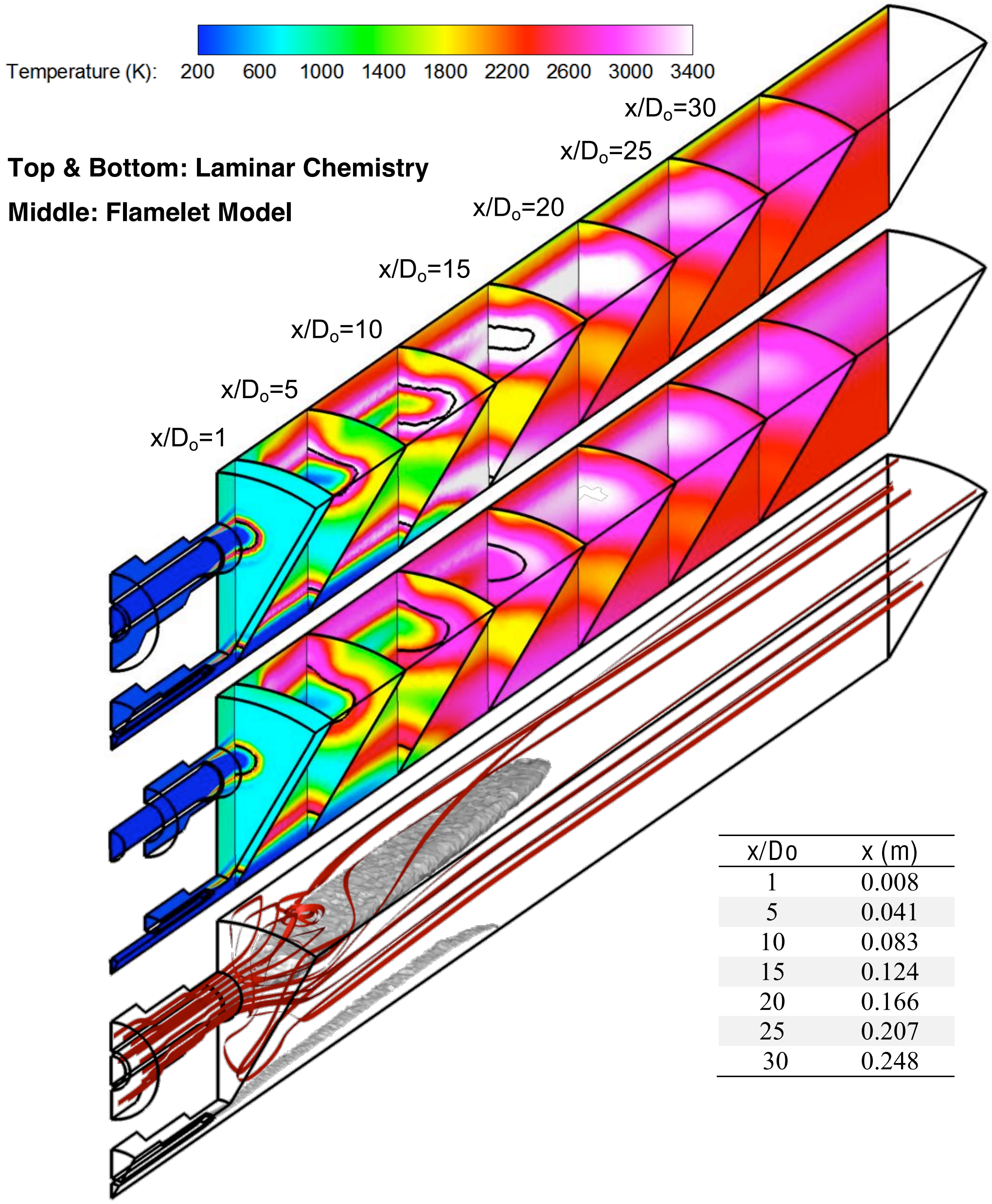

x/Do	x (m)
1	0.008
5	0.041
10	0.083
15	0.124
20	0.166
25	0.207
30	0.248

Figure 4.5: Temperature contours for axial plane slices. Bottom plot shows the streamline ribbons and the stoichiometric flame surface. D_0 is the fuel post outer diameter. Solid black lines indicate the stoichiometric mixture composition ($Z = 0.111$).

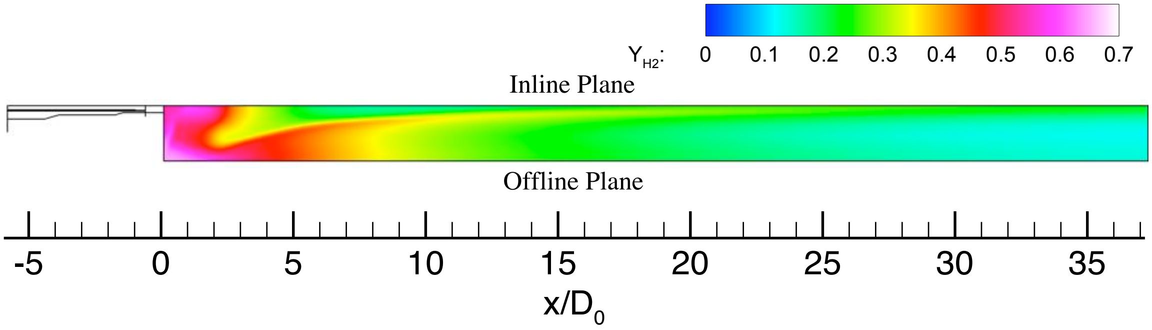

Figure 4.6: H_2 mass fraction contours along the chamber wall for the LFRC model simulation.

4.4 Estimation of Wall Heat Flux for the Flamelet Model

As discussed in Chapters 2 and 3, the current formulation of the SLFM does not account for wall heat transfer effects. However, the simulation results of the LFRC model suggest that the total heat losses to the walls amount to only about 1% of the heat generated via the reactions for the multi-element injector case under consideration. Thus, it can be expected that the effect of the wall heat losses is constrained to a thin region near the boundary. The temperature field plots shown in Figure 4.5 qualitatively support this view. In this case, using the computed near wall velocity and adiabatic wall temperature information, law-of-the-wall formulation as described in Chapter 2 can be utilized to construct the temperature gradient based on an assumed wall temperature and hence a wall heat flux value can be obtained. The procedure can be summarized in the following steps:

1. Axial velocity, density and temperature values at a location few grid points off the wall as well as distance to the wall are extracted from the flamelet model solution.
2. Mixture fraction variable is extracted at the wall and material properties (μ, λ, c_p) are calculated based on the extracted mixture composition and an assumed wall temperature.

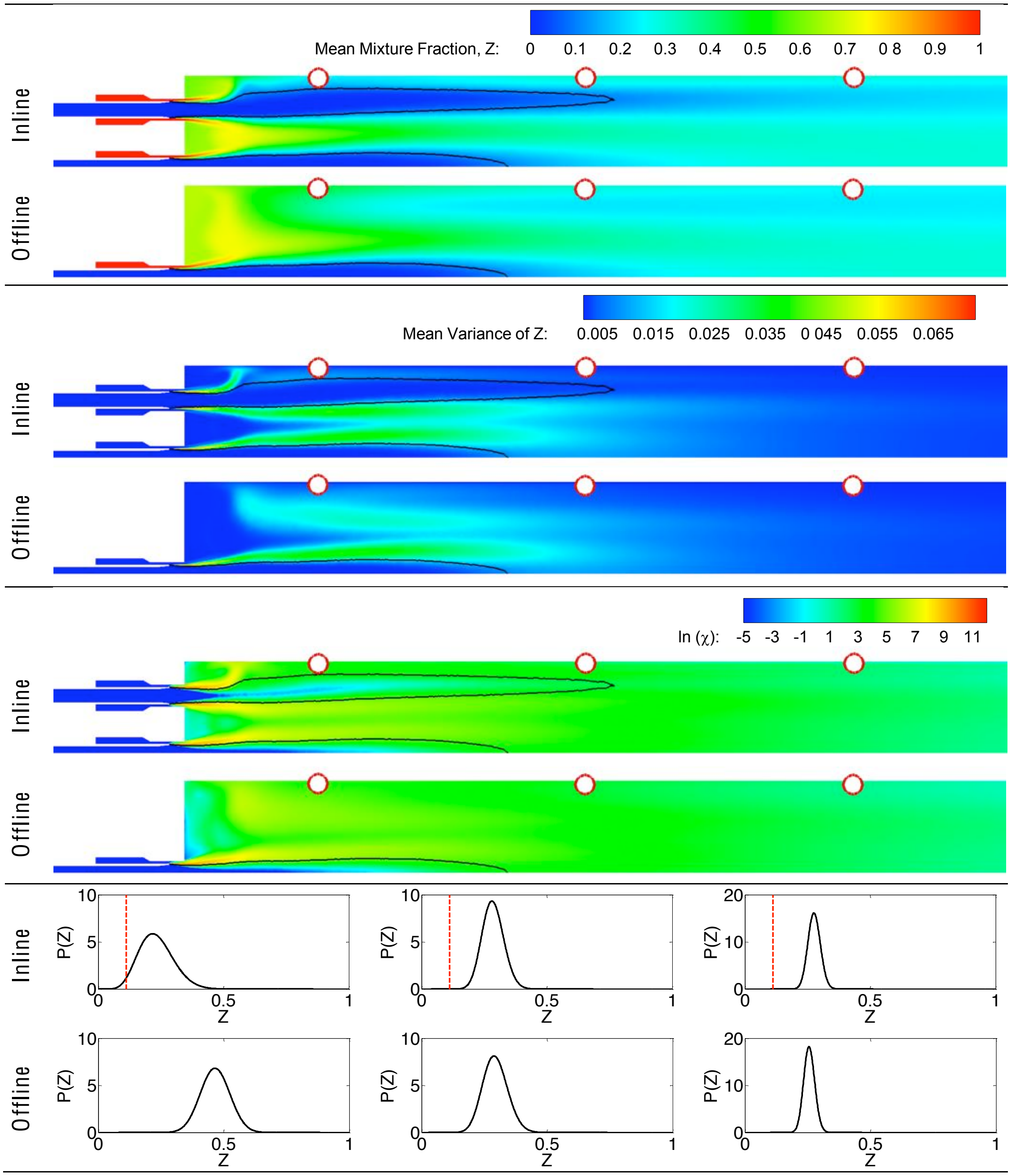

Figure 4.7: Contour plots for the mean mixture fraction, its mean variance and the scalar dissipation rate in the inline and offline planes and the corresponding mixture fraction PDF distributions at marked locations of $x = 0.05, 0.15, 0.25$ in meters. Black line corresponds to the stoichiometric flame surface, $Z = 0.111$

3. Based on the information obtained in steps 1 and 2, the law-of-the-wall formulation given in Equations 2.47 and 2.49 is iteratively solved to construct a near wall temperature distribution and hence the wall heat flux.

In the current study, the 3^{rd} grid node away from the wall is used in step 1. A temperature of 750 K and a Prandtl number of 0.7, consistent with the conditions for the LFRC model computation, are used at the wall. The selection of the 3^{rd} grid point at all axial locations is somewhat arbitrary and may result in inconsistencies for the following reasons:

- By using the 3^{rd} grid point off the wall, a part of the velocity field solution between the wall and the 3^{rd} grid node is being discarded and instead it is being replaced with the law-of-the-wall formula. In recirculating flow regions or in regions where there are significant streamline curvatures or pressure gradients near the wall, law-of-the-wall method loses its validity due to the empirical nature of the formulation. Thus, it is desirable to incorporate as much of the resolved flow information as possible by choosing the 1^{st} grid point off the wall as a basis for constructing the law-of-the-wall profiles.

- An adiabatic wall boundary condition is used with the SLFM. Hence the normal temperature gradient at the wall is zero. To construct the temperature profile with the law-of-the-wall method, the temperature value at the wall and at an additional point away from the wall need to be given. The wall value is assumed to be 750 K. For the second value, the computed temperature at the 3^{rd} grid point off the wall is given. This is in effect assuming that all or most of the temperature variation due to wall heat loss occurs in 3 cell heights distance from the wall. Considering the relatively small total heat loss to the wall for the current case, this assumption might be reasonable.

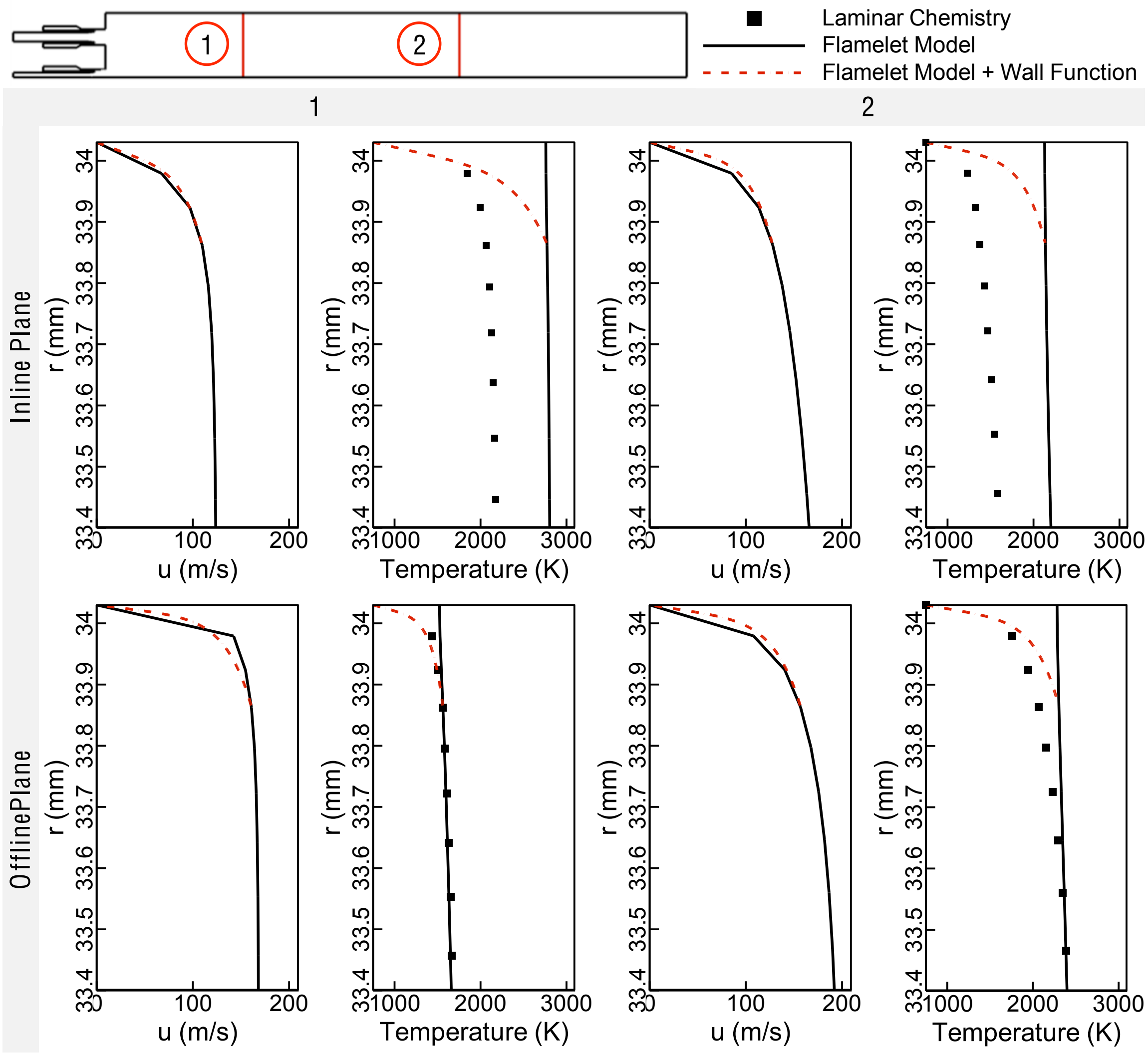

Figure 4.8: Radial temperature and velocity profiles at two different axial locations in the inline and offline planes. The upper range of the radial distance, r, correspond to the wall. The black symbols represent the LFRC model solution and they correspond to radial grid point locations.

In view of these discussions, the justification of the choice of the 3^{rd} grid point can be assessed by examining the near wall velocity and temperature profiles of the SLFM solution as well as the profiles reconstructed with the law-of-the-wall. Near wall temperature profile resulting from the LFRC model solution can also aid in the discussion. These profiles at two different axial positions in the inline and the offline planes are provided in Figure 4.8.

Note that despite the y^+ number of over 20 for the first grid cell center, the low-Reynolds number model was used (see Chapter 2) since the law-of-the-wall implementation is not available for the flamelet model. Therefore the near wall velocity profiles for the flamelet model solutions and those calculated afterwards via the law-of-the-wall are not expected to match identically. However, good agreement is obtained as shown in Figure 4.8. Moreover, the temperature profiles of the LFRC model solution show that the temperature variation due to the wall heat loss is largely contained within the first 3 grid points. The largest violation of this occurs at the downstream profile in the offline plane where an additional 15% temperature increase occurs between the 3^{rd} and the 10^{th} grid points. This can explain the over estimation of the wall heat flux at downstream locations in the intermediate and offline planes as seen in Figure 4.9. Ideally, rather than using a fixed height point of reference for the law-of-the-wall evaluations (such as the 3^{rd} grid point) at all axial locations, a local selection of this point can be made based on the local velocity boundary layer height.

This methodology is devised under the assumption that the wall heat transfer effect does not penetrate the bulk flow field and thus it is constrained to a thin near wall layer. This implies that the solutions of the problem with either isothermal or adiabatic wall boundary conditions are expected to match at the chosen reference point off the wall. Furthermore, since the methodology is based on the law-of-the-wall formulation, its applicability is limited to regions where the flow is attached to the wall and no significant streamline curvatures or wall normal pressure gradients exist.

4.5 Wall Heat Flux Distributions

The axial distribution of the combustion chamber wall heat flux along the inline, offline and intermediate planes are shown in Figure 4.9 (right column) in comparison to the experimental measurements of deRidder et al. [122; 123; 124]. The left column, on the other hand, shows the axial distribution of temperature along a near wall line with an offset of $4mm$ from the wall. The methodology proposed in the previous section is used to estimate the wall heat flux for the flamelet model solution. In the heat flux profiles for inline and intermediate planes, both laminar chemistry and flamelet model results show two dips roughly occurring at axial positions $x = 0.018\,m$ and $x = 0.038\,m$. These correspond to the closure of primary and secondary near wall recirculation zones as shown in Figure 4.5. The secondary recirculation zone does not extend up to the offline symmetry plane and hence only one dip in the heat flux curve is observed. Note that the law-of-the-wall near wall treatment was used for the laminar chemistry simulation. The flamelet model solution, on the other hand, was computed using a low-Re near wall model but the heat flux distribution was estimated as a post processing step utilizing the law-of-the-wall formulation. The limitations of this formulation were discussed in Chapter 2. The law-of-the-wall loses its validity in regions where a near wall recirculation zone exists. As shown in Chapter 3, under prediction of the heat flux in these regions is expected. The under prediction in the intermediate plane extends up to $x = 0.13\,m$ whereas quantitative agreement with the experimental data is achieved somewhat earlier for the offline plane. This is in direct correlation with aligning of the streamlines with the wall as seen in Figure 4.5. In the inline plane, an additional cooling effect, due to the fuel rich layer as discussed earlier, is observed. The size and the extent of this layer are predicted differently with the laminar chemistry and the flamelet models. The thinner layer resulting from the flamelet model simulations translates into an overall larger near wall temperature distribution in the inline plane (Figure 4.9, top row, left). The outcome is that the laminar chemistry model consistently under predicts the heat flux by 30-40% compared to the experimental measurements. The flamelet model, on the other hand, was able to reproduce the experimental distribution fairly well downstream of the recirculating regions. Common to both the intermediate and the offline planes, the flamelet model wall heat flux distribution shows an increasing trend towards downstream. This stems from the current methodology for the heat flux estimation as discussed in the previous section.

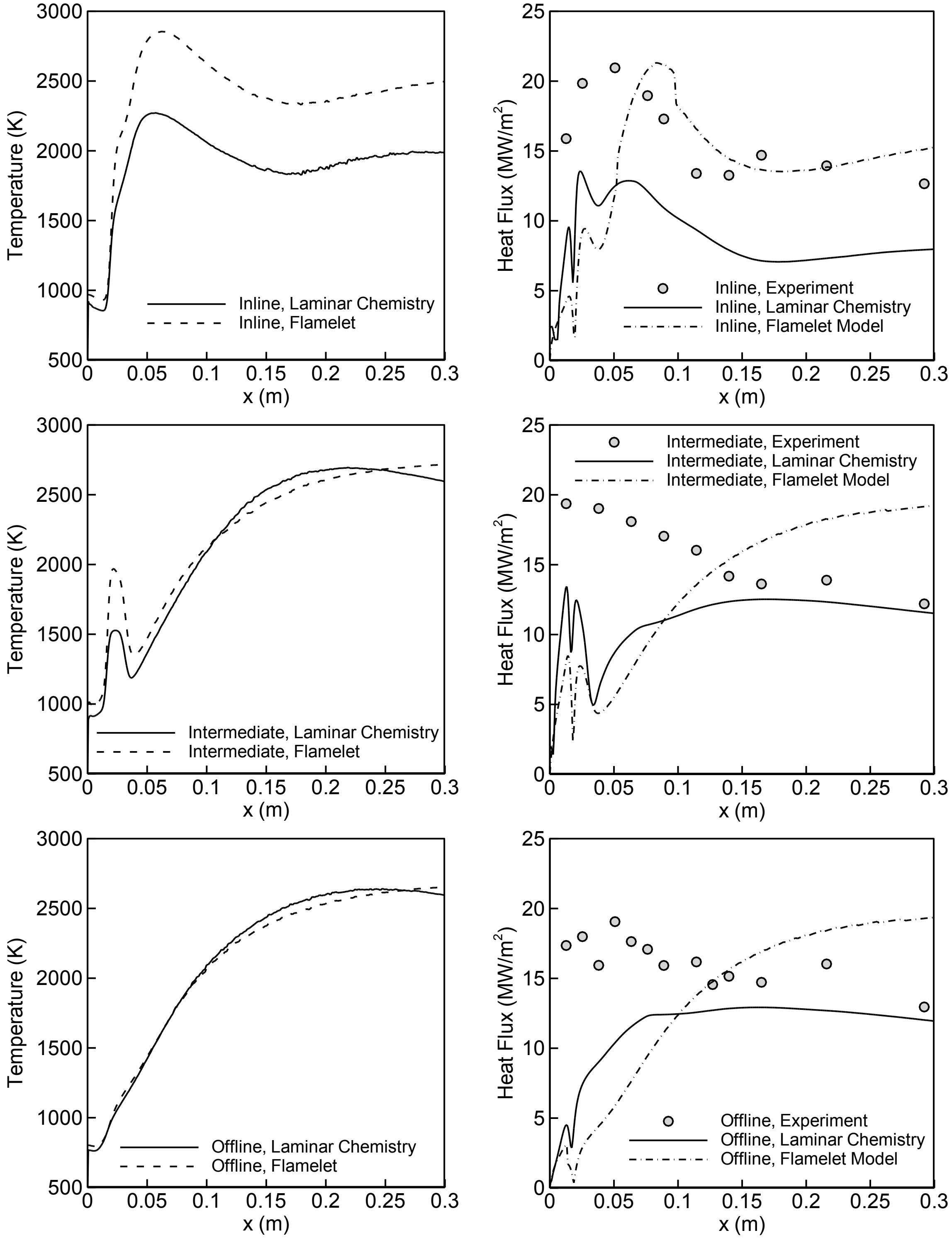

Figure 4.9: Spatial distribution of combustion chamber wall heat flux, computed and experimental [122; 123; 124].

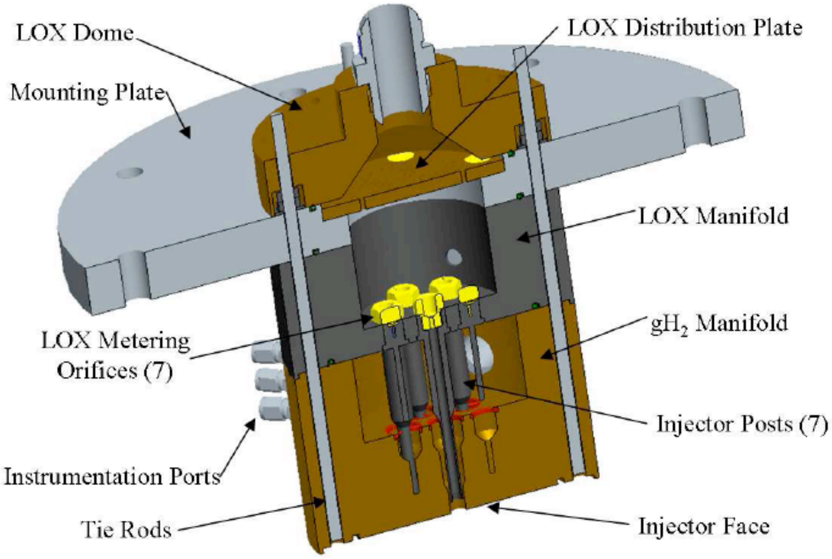

Figure 4.10: Experimental injector setup overview (from deRidder et al. [122; 123; 124]).

4.6 Oxygen Phase

The oxygen feed was measured by deRidder et al. [122; 123; 124] to be at about $1000psi$ pressure and $-300F$ ($89K$) temperature at the LOX manifold as shown in Figure 4.10. At the measured chamber pressure of $823.1psi$, oxygen transitions from liquid to supercritical stage at a temperature of $155K$. Therefore, it is likely that the oxygen enters the combustion chamber in liquid phase and quickly changes to supercritical conditions.

In both the LFRC model and the SLFM computations, the ideal gas equation of state was used. While this is a reasonable representation of the supercritical fluid behavior for temperatures larger than about $250K$ (see Figure 4.11, bottom), it results in a grossly under predicted density within the oxygen inlet nozzle and in a small region near the injector exit (see Figure 4.11, top). Since experimentally measured mass flux values are specified at the inlets, this means that an unrealistically large oxygen injection velocity (hence momentum flux) was used. To investigate the extent to which the flow field is affected by this misrepresentation of the oxygen phase within

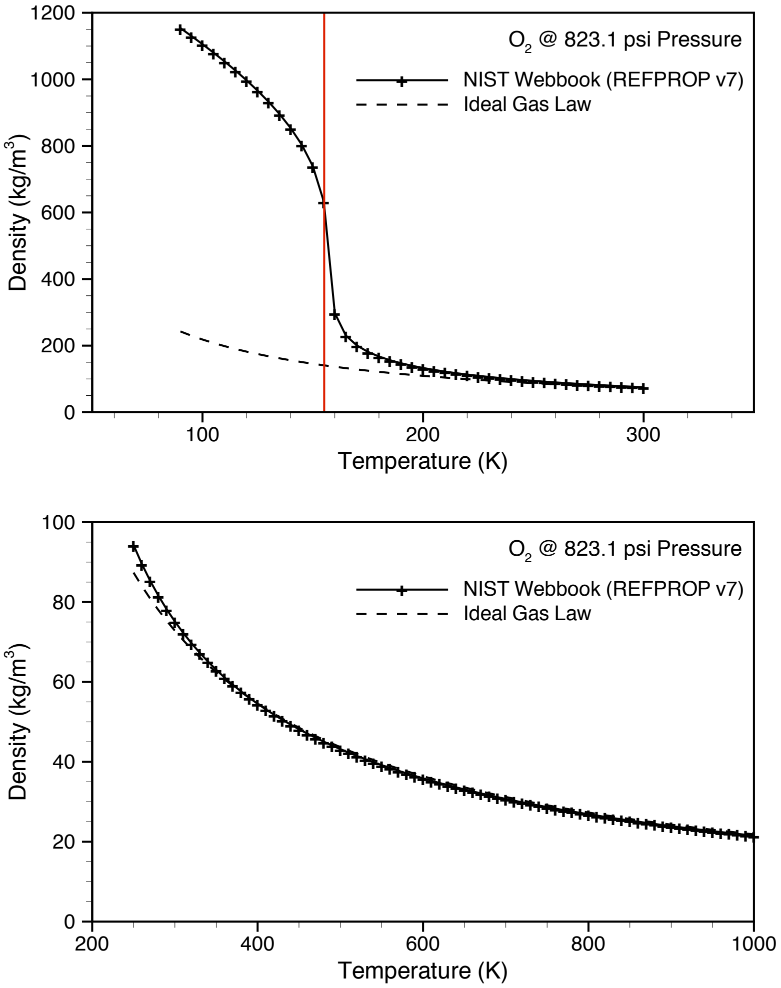

Figure 4.11: Variation of density with temperature for oxygen at 823.1 psi pressure.

the injector nozzle, a real fluid equation of state applicable at cryogenic conditions needs to be utilized.

As mentioned in Chapter 1, Bittker's [10] approximate calculations show that the gaseous mixing process is generally faster than spray evaporation and hence the latter is the rate controlling phenomena. The validity of this statement in the context of shear coaxial injector elements in general and for the current injector in particular is not known. Thus, beyond using the proper equation of state, accounting of the atomization and evaporation process may have a large impact on the solution and need to be investigated.

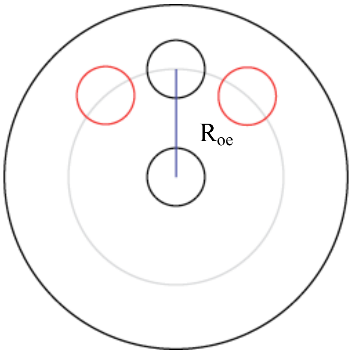

Design Variable	Baseline	Min	Max
Radial distance of the outer row of elements (R_{oe})	0.84 in	0.59 in	1.09 in
Number of outer row elements (N_{oe})	6	4	8

Figure 4.12: Design variables and ranges.

4.7 Parametric Study of Multiple Element Injector Configurations

In liquid rocket injector design, the arrangement and number of individual injector elements play an important role in the performance and reliability of the combustors [9]. Interaction of injector elements affects the mixing characteristics and hence the flame length as well as the heat the combustion chamber is exposed to. While reduction of both is desirable, the design choice may often be a compromise between the two objectives. CFD analyses of such problems offer substantial quantitative data and the ability to evaluate a much greater range of design configurations compared to the traditional ad-hoc and experiment based design methods.

In this study, the 7 element injector configuration due to deRidder et al. [122; 123; 124] is taken as a basis to examine the effect of injector element arrangements on flame length and the adiabatic chamber wall temperature using the SLFM simulations. Specifically, the radial distance of the outer row of elements and the number of elements in the outer row are varied as shown in Figure 4.12. In this particular problem, ranges of the design variables are restricted by geometrical bounds.

A Design of Experiments (DOE) using 13 simulation points is constructed. The

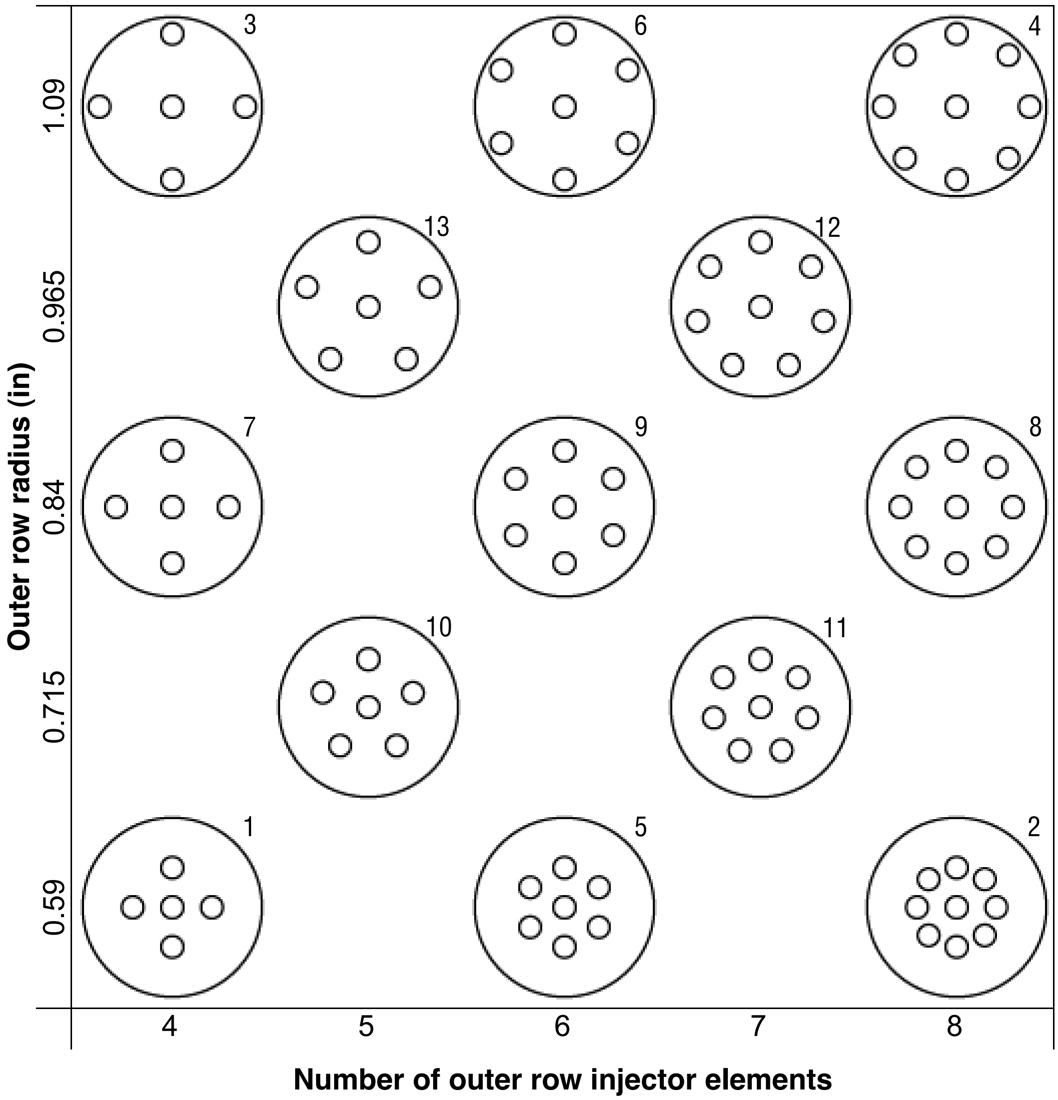

Figure 4.13: Design of experiments (DOE). Case 9 is the baseline case due to deRidder et al. [122; 123; 124].

Face-centered Central Composite Design (FCCD) [125] is used, while inserting 4 additional points at the centers of each quadrant to increase resolution as shown in Figure 4.13. Although the number of injector elements is varied, the total mass flow rate of oxidizer and fuel is kept the same as the baseline case due to deRidder et al. [122; 123; 124].

For each design point, a CFD simulation using the SLFM is run. The simulation results for flame length and peak adiabatic wall temperature are used to construct a

2^{nd} order Polynomial Response Surface (PRS) for each via the least squares method. Several different error measures can be employed to assess the quality of fit. For given simulation results y_i and the corresponding PRS evaluation $\hat{y}_i$, error at each simulation point is given as:

$$\varepsilon_i = y_i - \hat{y}_i \tag{4.1}$$

For P number of training points, the Root Mean Square (RMS) error is given by:

$$\sigma = \sqrt{\frac{\sum_{i=1}^{P} \varepsilon_i^2}{P}} \tag{4.2}$$

The coefficient of multiple determination is defined as:

$$R^2 = 1 - \left(\frac{\sigma^2 (P-1)}{\sum_{i=1}^{P} (y_i - \bar{y})^2} \right), \quad \bar{y} = \frac{\sum_{i=1}^{P} y_i}{P} \tag{4.3}$$

An R^2 value close to 1 indicates a good fit.

Contour plots of temperature for the baseline case as well as for the corner points of the design space are provided in Figure 4.14 while the peak wall temperature and flame length for each case are tabulated in Table 4.2. PRS plots for both and the corresponding fitting errors are shown in Figure 4.15.

In Figure 4.14, a general trend of decreasing flame length can be observed traversing from top to bottom row, meaning decreased outer row radius. Proximity of the central injector element to the outer row elements enhances mixing, and in general reduces the maximum flame length. Flame length seems to show less sensitivity to variations in the number of outer row elements (total mass flux is kept the same). These trends can also be clearly observed from the 2^{nd} order PRS as shown in Figure 4.15. Acceptable PRS fitting errors suggest fairly monotonic behavior of decreasing flame length with decreasing outer row radius and insensitivity to the number of outer row elements. An exception to the trend is observed in test Case 2 (max. outer row elements, min. outer row radius) where the outer row elements are circumferentially closest to each other among the 13 cases considered. Flame surfaces of two consequent injector elements on the outer row merge on the offline plane (see bottom left of Figure 4.14) causing an increase in flame length. Also in this situation, peak wall temperature is realized along the offline plane as opposed to the other configurations which consistently yield the peak near or on the inline plane. A monotonic trend of decreasing flame length with decreasing R_{oe} is observed.

Gill [9] notes that the performance of shear-coaxial elements mostly depends on individual element onfiguration and that it is insensitive to inter-element placement. The findings presented here show significant variation of the flame length with different injector arrangements and thus they are in contradiction to this statement.

It can be observed from Figure 4.14 and Table 4.2 that the peak adiabatic wall temperature is largely affected by two phenomena:

1. Increased outer row radius, therefore closer proximity of the outer flame surface to the wall, results in an increased wall temperature.

2. As the outer row jets and the central jet get closer, with reduced outer row radius, outer jets angle towards the wall due to the interaction. Therefore resulting again in an increased peak wall temperature as well as an extension of the hot wall region towards upstream.

These two competing effects suggest existence of an optimum outer row radial location where the outer flame surface is sufficiently displaced from the wall while interaction with the central jet is limited so as to not alter the flame angle significantly towards the wall. Among the simulated cases, the baseline configuration (case 9) most closely fits these criteria and results in the lowest wall temperature. This non-monotonic behavior of the peak adiabatic wall temperature causes large fitting errors for the

Table 4.2: Simulation results at DOE points.

Case	Outer Row Radius (in)	Number of Outer Row Elements	Flame Length (m)	Peak Wall Temperature (K)
1	0.59	4	0.130	2925
2	0.59	8	0.104	3294
3	1.09	4	0.190	3119
4	1.09	8	0.184	3166
5	0.59	6	0.111	3316
6	1.09	6	0.217	3514
7	0.84	4	0.185	3045
8	0.84	8	0.114	3403
9	0.84	6	0.160	2764
10	0.715	5	0.126	3408
11	0.715	7	0.108	3448
12	0.965	7	0.212	3521
13	0.965	5	0.211	3355

2^{nd} order PRS (see Figure 4.15, right). Despite the large fitting errors, the low order trend obtained via the PRS suggests a declining peak wall temperature with reduced number of outer row elements.

4.8 Summary and Conclusions

An experimental multi-element H_2/O_2 injector due to deRidder et al. [122; 123; 124] was analyzed with the LFRC model and the SLFM with only the latter accounting for the turbulence-chemistry interactions (TCI). The SLFM, due to TCI, resulted in reduced temperatures near the stoichiometric flame surface as expected.

A near wall cool fuel rich layer that gradually merges to the inline plane after the closure of the recirculation region was predicted by both models, however with different layer thicknesses. The SLFM predicted a thinner layer that yielded a higher near wall temperature in the inline plane compared to the LFRC simulation results.

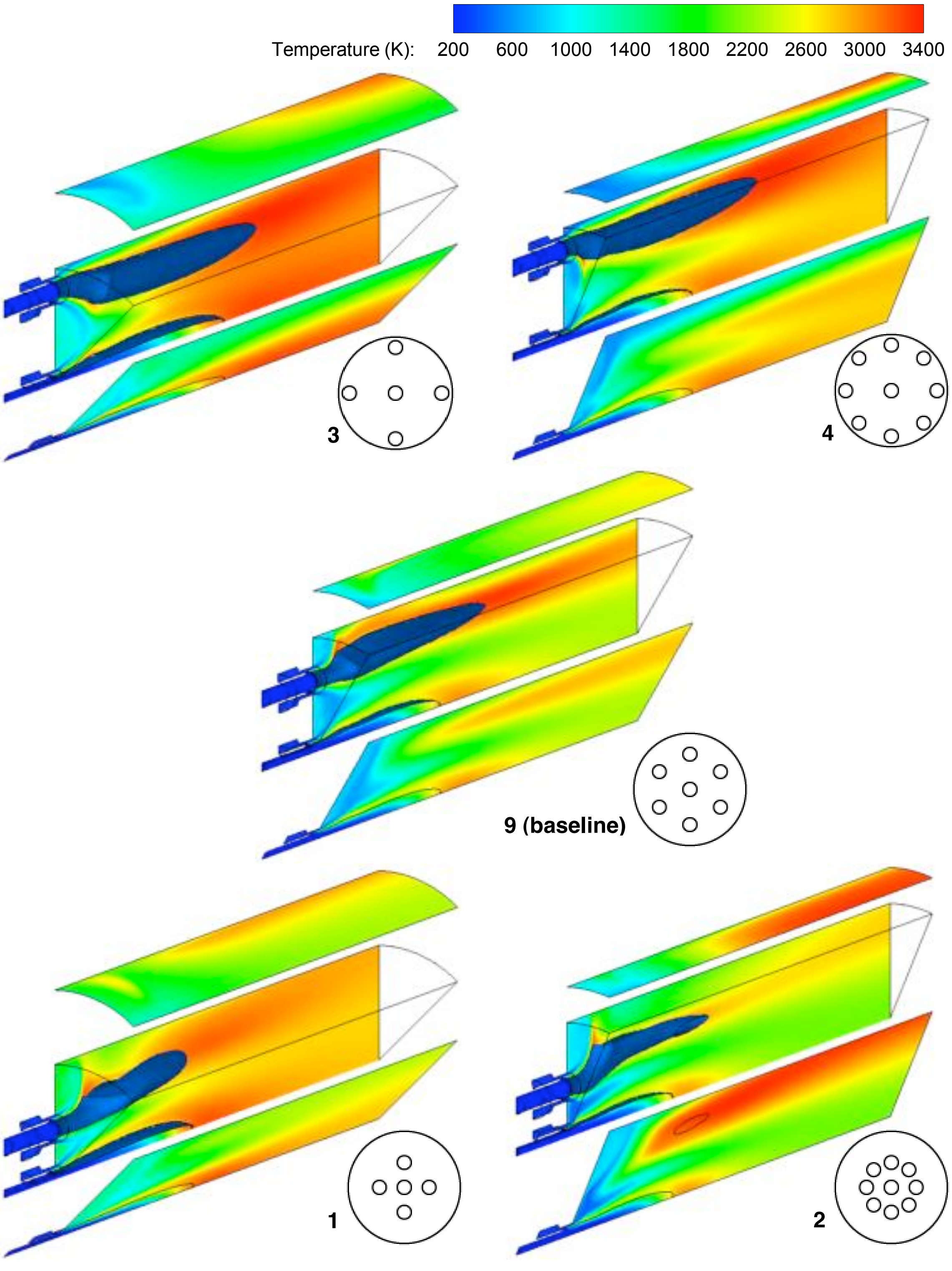

Figure 4.14: Temperature contours for the baseline case and the corner points of the design space. The stoichiometric flame surface is shown in dark blue. SLFM was used in the computations.

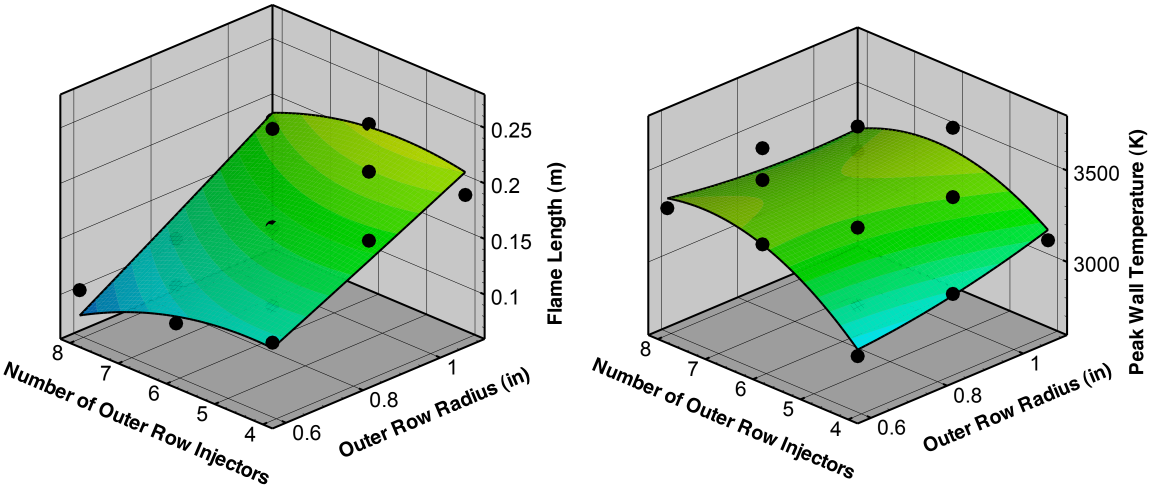

min Error	-0.033
max Error	0.0216
RMS Error	0.0178
R^2	0.82

min Error	-218
max Error	557
RMS Error	187
R^2	0.31

Figure 4.15: Polynomial response surfaces for flame length (left) and peak adiabatic wall temperature (right) and corresponding fitting errors. Black points represent CFD output at DOE points.

A methodology based on the law-of-the-wall formulation was described for obtaining wall heat flux distribution as a post processing step to the SLFM simulations. The accuracy of the proposed methodology relies on the wall heat loss effects being contained within a thin layer near the wall. For the current multi-element injector problem, this was verified by:

- Inspection of the temperature fields of the SLFM and the LFRC model results,
- LFRC model heat flux results showing that the wall heat loss is only about 1% of the total heat generated withing the combustion chamber.

The overall wall heat flux distribution was under predicted in the inline plane by the LFRC model. The SLFM prediction for the inline plane, on the other hand, was in good agreement with the experimental data in the wall attached flow region (see

Figure 4.9). In both the inline, intermediate and offline planes, both models suffered from under-predicting the experimental wall heat flux values in the upstream regions where near wall recirculation regions or large streamline curvatures exist. This is due to the limitations of the law-of-the-wall formulation as described in Chapter 2, and the under prediction is consistent with the findings presented in Chapter 3. A zonal wall treatment approach as demonstrated in Chapter 3 may be helpful to improve the predictions. In addition, accounting for the correct liquid oxygen density near the injector exit (as discussed in Section 4.6) may alter the predictions significantly.

In the second part of this study, the number of outer injector elements (N_{oe}) and the radius of the outer row of elements (R_{oe}) are varied while keeping the fuel and oxidizer mass flow rates constant. 13 different geometric configurations are simulated with the SLFM. The resulting flame length and peak adiabatic wall temperature data were fitted with 2^{nd} order polynomial response surfaces (PRS). A fairly monotonic increase of the flame length with increased R_{oe} was observed while it was less sensitive to variations in N_{oe}. The low order trend for the peak adiabatic wall temperature observed from the PRS suggests a monotonic decrease with decreased N_{oe}, and an insensitivity to R_{oe}. This is in contrast to the behavior of the flame length. However, large non-monotonic variations of the peak wall temperature with R_{oe} occur. These are not represented by the PRS and apparent from the large fitting errors associated with it. Non-monotonic dependence of the peak wall temperature (see Figure 4.15 and Table 4.2) is linked to two competing effects:

1. Flame surface to wall proximity with increased R_{oe},
2. Angling of the outer jet towards the wall (effect of the interaction with central jet) with decreased R_{oe}.

Both result in increased wall temperature, suggesting that an optimum R_{oe} location exists. Increased number of simulation points in the DOE together with either a higher order PRS or other fitting methodologies such as Kriging [126] are needed to accurately determine the optimum location.

CHAPTER V

Multi-Scale Thermo-Fluid Transport in Porous Media

Porous materials are often used for the injector face plate of liquid rocket engines. Fuel bleeds through the porous plate to aid in cooling of the injector face by transpiration. In P&W's RL10 engine and the Space Shuttle Main Engine (SSME), Rigimesh porous material is used [127]. Rigimesh can qualitatively be classified as a dense, non-uniform, fibrous porous media (See Figure 5.1). In the case of SSME, a 0.25" thick plate with about 9% void space is used. Our ultimate goal in this study is accurate simulations of fluid flow and heat transfer through the Rigimesh material. To achieve this, detailed knowledge of the material's internal structure is needed.

Fluid flows and associated heat and mass transfer through such porous media are

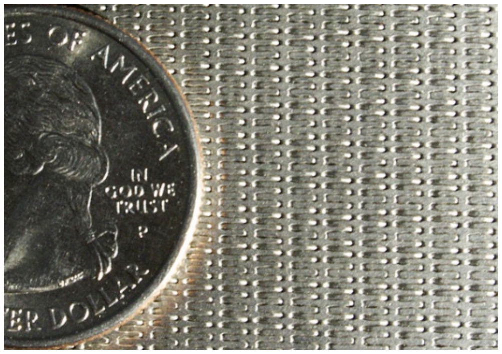

Figure 5.1: Surface features of the Rigimesh material used in SSME.

two-phase phenomena where one of the phases is solid and stationary. To simulate such flows, interaction of fluid and solid phases at the scales as small as individual pores of the material needs to be accounted for. Considering typically wide range of length scales and complex geometries involved in porous media, analysis of each individual pore can be very costly or even impossible. Thus, the modeling efforts in this area dating back to Darcy's [128] experimental study in 1856 have mostly aimed at empirically correlating the pore level flow effects to the bulk fluid motion. Darcy experimented with gravity driven flow of water through a porous medium of loosely packed, uniform sized particles. He related the pressure gradient to the average fluid velocity, introducing an empirical factor called permeability:

$$-\nabla p = \frac{\mu}{K} u_D \tag{5.1}$$

The permeability, K, with the dimension of $length^2$ is a measure of fluid flow conductivity of the porous media. The filter velocity, u_D, is defined as:

$$u_D = \frac{\dot{m}}{\rho A} \tag{5.2}$$

Equation 5.1 is of first order and as such it only allows one condition to be applied at a given boundary. This becomes a problem when the porous matrix is bounded by walls or adjacent to an open flow domain. Typical practice for walls is to apply a slip boundary condition by setting only the velocity component normal to the wall as zero. For the open/porous domain interface, an empirical boundary condition is derived by Beavers and Joseph [129].

An alternative formulation governing the fluid flow through porous media is suggested by Brinkman [130; 131] by adding a viscous diffusion term to the Darcy's Law, obtaining a second order equation:

$$-\frac{\partial p}{\partial x_i} = \frac{\mu}{K} u_{D,i} + \mu' \frac{\partial^2 u_{D,i}}{\partial x_j^2} \tag{5.3}$$

where μ' is termed as effective viscosity. Lundgren [132] studied and justified the Brinkman equation and connected the effective viscosity, μ' , to the porosity of the solid matrix. Porosity, ε, is defined as the volume fraction of the void space in a given porous media. Brinkman equation was derived for a dilute arrangement of spheres and thus deemed valid for high porosities [133], i.e. $\varepsilon > 0.8$. For lower porosity cases, the Darcian contribution dominates and the viscous diffusion term serves the purpose of raising the order of the equation so that the no-slip condition can be applied at bounding walls. Therefore, it is a common practice to set the effective viscosity, μ', equal to the fluid viscosity, μ.

The linear relationship represented by Darcy's Law fails when the flow Reynolds number is high enough for inertial effects to become comparable to Darcian effects. Macdonald et al. [134] examined several experimental results and concluded that the inertial flow regime starts roughly when a Reynolds number based on permeability, $Re_{\sqrt{K}} = \rho u_D \sqrt{K}/\mu$, is unity. At higher Reynolds numbers, inertial effects become comparable to Darcian effects. A correction for this flow regime is suggested by Forchheimer [135] and presented in the following form by Ward [136]:

$$-\frac{\partial p}{\partial x_i} = \frac{\mu}{K} u_{D,i} + \frac{C_E}{\sqrt{K}} \rho |u_{D,i}| u_{D,i} \tag{5.4}$$

Where C_E is called the Ergun coefficient [137]. It is also widely used as C_F which stands for Forchheimer coefficient.

Equation 5.4 involves two parameters; permeability, K, and Ergun coefficient, C_E, which need to be found experimentally for a specific type of porous media. Various methods have been suggested to relate these parameters to the geometrical properties of the porous material such as the porosity and a length scale. Dullien [138] suggested modeling the porous media as a network of conduits. Using the Hagen-Poiseuille solution, Darcy's Law (Equation 5.1), and total pressure drop, he related the permeability to porosity and the conduit volumes and diameters. In a similar approach, porous media is modeled as periodic arrangements of cylinders [139; 140] or spheres [140] so that the creeping flow solution is benefited in relating the permeability to the porosity, particle diameters and inter-particle gaps. Dullien [138] also suggested a widely used permeability model based on the Carman-Kozeny hydraulic radius theory [141]. In this model, permeability is related to the porosity, hydraulic radius and Kozeny constant which depends on the pore shape. For the Ergun coefficient, Ward [136] suggested a universal constant value of 0.55. These heuristic approaches summarized here are mostly limited in range of porous media types and suffer from a common underlying assumption of permeability and Ergun coefficient being pure geometric parameters. We will show later that this is in fact not the case. Detailed summary on this kind of approaches can be found in [138; 142; 143].

The modeling approaches mentioned so far have been empirical, semi-empirical or ad-hoc. A more fundamental approach has been developed by Slattery [144; 145] and Whitaker [146; 147] by averaging the governing equations over local volume elements that contain both fluid and solid phases. Although this will reduce the complexity of the problem, the information lost by filtering the fine scale flow structures will cause an unclosed set of governing equations. Whitaker [147] and Nozad et al. [148] also offered closure methodologies for the averaged momentum and energy equations respectively. Local volume averaging method has gained widespread popularity in modeling fluid flow and heat transfer through porous media. Conventionally, the resulting closure terms in the averaged momentum equations are heuristically linked [149] to the relations proposed by Darcy and Ergun which require empirical determination of the parameters K and C_E.

Cheng and Minkowycz [150], on the other hand, developed another rigorous formulation by introducing a similarity solution for Darcian free convection along a boundary layer developing in a fluid saturated porous medium adjacent to a heated vertical wall. This approach is later extended to combined free and forced convection about inclined walls [151], non-Darcian (inertial) regime [152], mixed convection-conduction problems [153] and many other boundary layer type flows. An inclusive coverage of these methods can be found in Nield and Bejan [143].

To develop non-empirical predictive capabilities for porous media problems, we follow a first principle based, multi-scale strategy. In our approach, the effect of porous structure on the global fluid flow is accounted for via local volume averaged governing equations. The resulting set of transport equations contains closure terms representing the statistical flow characteristics around the pores. Most porous media can be thought of as a matrix of repeating pore patterns. So, the closure terms can be deduced beforehand by direct computation of the fluid flow in individual, representative pore samples for varying flow speeds. Thus, excessive computational cost of a direct simulation approach can be avoided while producing accurate numerical predictions completely free of empiricism.

In this chapter, we first describe the issues related to the characterization of the Rigimesh material. Then, we review derivation of local volume averaged governing equations as well as closure methodologies. The developed model is incorporated into Navier-Stokes solvers [95; 24; 96] and assessed using a recent experiment by Tully et al. [154] motivated by the liquid rocket engine applications.

5.1 Rigimesh Characterization

Rigimesh is a porous material with sintered multiple layers of stainless steel woven-wire-meshes. Bonding of fibers at each contact point due to the sintering process provides rigidity and thus allows finer fiber diameters to be employed. Finer fiber diameters in effect mean more surface area for a given volume or porosity. These

Figure 5.2: Rigimesh cross section after bending fracture.

properties make Rigimesh an appropriate fit for the applications that demand high cooling efficiency and rigidity. One such area is the injector face plate of liquid propellant rocket engines.

In order to develop high fidelity models for the simulation of flow and heat transfer through the Rigimesh media, precise understanding of the inner topology as well as the inner dimensions is essential.

In order to characterize the Rigimesh structure, a plate sample of $5.8mm$ thickness is examined. Although the surface was hinting a woven structure, examining the cross section was needed to identify the orientation of layers. In order to get a clean cross sectional view of the material, a plate sample is fractured by bending. Although the bending process caused elongation and distortion of the fibers, the cross section view obtained (see Figure 5.2) gave valuable clues about the inner topology.

A Rigimesh specimen was analyzed using CT scan. Unfortunately, the CT images did not have enough resolution to offer more information about the material. The surface properties of the Rigimesh were also examined by the contact profilometer measurement technique. A sensitive needle is traversed along the surface of the Rigimesh plate while maintaining contact. Position of the needle tip is recorded every $0.5\mu m$ for a $10mm$ span. Lin and Hu [155] have conducted the measurements. Their results show that the average distance between the peaks is $0.42mm$ which is a measure of the distance between fiber axes on the surface. The outcome is presented

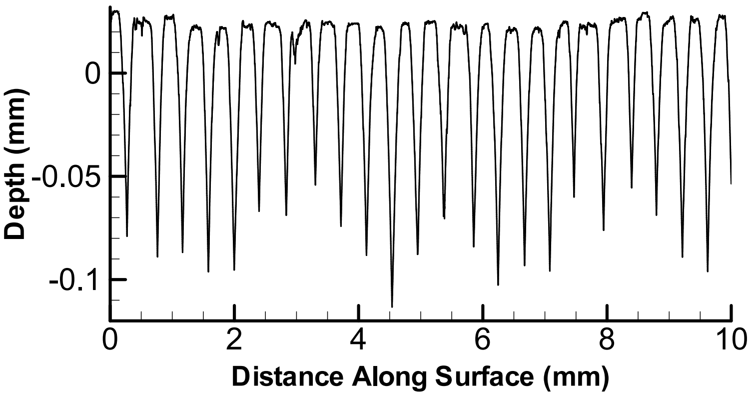

Figure 5.3: Rigimesh surface characterization by Lin and Hu [155].

in Figure 5.3.

The information obtained thus far about the detailed Rigimesh structure helps illustrate some aspects of Rigimesh; more efforts are needed to fully characterize the three-dimensional geometric structures.

5.2 Multi-Scale Porous Media Model

5.2.1 Local Volume Averaging

In the context of averaging the governing equations, first a sensible scale for an averaging volume needs to be defined. An averaging volume should be sized small enough in order to not filter global flow structures but it should be large enough so as to guarantee containing both fluid and solid phases at all times. Such a volume is called a Representative Elementary Volume (REV) (see Figure 5.4). In our multi-scale methodology, we further require an REV to be a repeated pattern over a portion of the porous media.

The porosity, ε, is defined as the volume fraction of fluid phase in a porous media:

$$\varepsilon = \frac{V_f}{V} \tag{5.5}$$

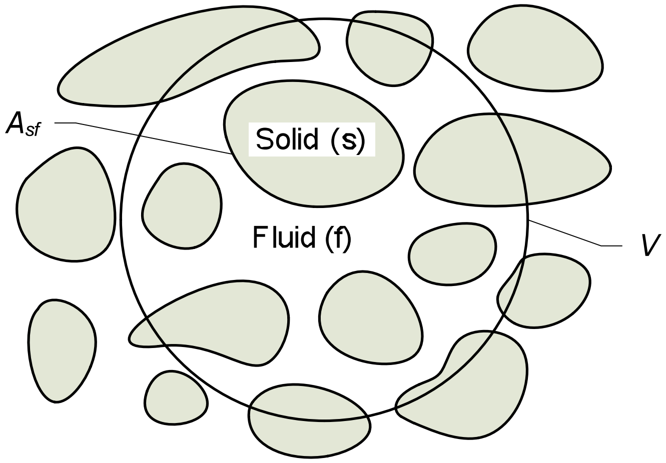

Figure 5.4: Schematic of a representative elementary volume (REV).

Note that the porosity might be defined locally or globally depending on the scale that the volume fraction is calculated. In this study, however, we will assume that the porosity is uniform over the porous media. For an arbitrary property ψ defined for the fluid phase, volume averaging can be carried out as follows [147]:

Intrinsic Averaging:

$$< \psi >^f = \frac{1}{V_f} \int\limits_{V_f} \psi dV \tag{5.6}$$

Superficial Averaging:

$$< \psi > = \frac{1}{V} \int\limits_{V_f} \psi dV = \varepsilon < \psi >^f \tag{5.7}$$

5.2.2 Averaging of the Continuity Equation

The local volume averaged continuity equation can be written as:

$$\frac{\partial < \rho >}{\partial t} + \left\langle \frac{\partial}{\partial x_i}(\rho u_i) \right\rangle = 0 \tag{5.8}$$

Note that we want to solve for volume averaged flow quantities. So we need to express the second term in Equation 5.8 in terms of $< \rho >$ and $< u_i >$. The necessary transformation can be achieved via the volume averaging theorem [144; 146]:

$$\left\langle \frac{\partial \psi}{\partial x_i} \right\rangle = \frac{\partial < \psi >}{\partial x_i} + \frac{1}{V} \int\limits_{A_{sf}} \psi n_i dA \tag{5.9}$$

Here, n_i is the area normal pointing from the fluid phase towards the solid phase. Using Equation 5.9, Equation 5.8 becomes:

$$\frac{\partial < \rho >}{\partial t} + \frac{\partial < \rho u_i >}{\partial x_i} + \frac{1}{V} \int\limits_{A_{sf}} \rho u_i n_i dA = 0 \tag{5.10}$$

Since the fluid will be at rest at the solid-fluid interface due to the no-slip condition, the last term in Equation 5.10 vanishes, and we get:

$$\frac{\partial < \rho >}{\partial t} + \frac{\partial < \rho u_i >}{\partial x_i} = 0 \tag{5.11}$$

For incompressible flows:

$$\frac{\partial < u_i >}{\partial x_i} = 0 \tag{5.12}$$

Thus, the form of the continuity equation is unchanged by local volume averaging for incompressible flows. In the case of compressible flows, we need to have a special treatment for averaging of the product of the density and the velocity component.

The derivations hereafter assume incompressible flow with constant properties. We further consider that the porosity is constant throughout the porous media. These aspects can be generalized.

5.2.3 Averaging of the Momentum Equation

Averaging the momentum equation with no body forces yields:

$$\rho\frac{\partial < u_i >}{\partial t} + \rho\left\langle\frac{\partial u_i u_j}{\partial x_j}\right\rangle = \left\langle\frac{\partial T_{ij}}{\partial x_j}\right\rangle \tag{5.13}$$

Once again, we need to transform the inertial and the stress terms using Equation 5.9 so that only the averages of the primitive flow variables are left in the final form instead of averages of their combinations or derivatives.

Inertial Term

Following the approach of Gray [156], we decompose the velocity as:

$$u_i =< u_i >^f + u_i' \tag{5.14}$$

where $(\quad)'$ represents local deviation from the intrinsic averaged values. Applying Equation 5.14 to the volume-averaged convective term:

$$\begin{aligned}\left\langle\frac{\partial u_i u_j}{\partial x_j}\right\rangle &= \left\langle\frac{\partial}{\partial x_j}\left((u_i' + < u_i >^f)(u_j' + < u_j >^f)\right)\right\rangle \\ &= \left\langle\frac{\partial < u_i >^f < u_j >^f}{\partial x_j}\right\rangle + \left\langle\frac{\partial u_i' u_j'}{\partial x_j}\right\rangle \\ &+ \left\langle\frac{\partial < u_i >^f u_j'}{\partial x_j}\right\rangle + \left\langle\frac{\partial u_i' < u_j >^f}{\partial x_j}\right\rangle\end{aligned} \tag{5.15}$$

Using Equation 5.9:

$$\begin{aligned}\left\langle\frac{\partial u_i u_j}{\partial x_j}\right\rangle = \frac{\partial << u_i >^f < u_j >^f >}{\partial x_j} + \frac{1}{V}\int\limits_{A_{sf}} < u_i >^f < u_j >^f n_j dA \\ + \left\langle\frac{\partial u_i' u_j'}{\partial x_j}\right\rangle + \left\langle\frac{\partial < u_i >^f u_j'}{\partial x_j}\right\rangle + \left\langle\frac{\partial u_i' < u_j >^f}{\partial x_j}\right\rangle\end{aligned} \tag{5.16}$$

The third and the fourth terms can also be treated similarly:

$$\left\langle \frac{\partial < u_i >^f u'_j}{\partial x_j} \right\rangle = \frac{\partial << u_i >^f u'_j >}{\partial x_j} + \frac{1}{V} \int\limits_{A_{sf}} < u_i >^f u'_j n_j dA \tag{5.17}$$

Noting that $< u'_j >= 0$ and $u'_j = u_j - < u_j >^f$:

$$\left\langle \frac{\partial < u_i >^f u'_j}{\partial x_j} \right\rangle = \frac{1}{V} \int\limits_{A_{sf}} < u_i >^f u_j n_j dA - \frac{1}{V} \int\limits_{A_{sf}} < u_i >^f < u_j >^f n_j dA \tag{5.18}$$

Since the velocity is zero at the solid-fluid interface due to no-slip condition, the first integral term vanishes:

$$\left\langle \frac{\partial < u_i >^f u'_j}{\partial x_j} \right\rangle = -\frac{1}{V} \int\limits_{A_{sf}} < u_i >^f < u_j >^f n_j dA \tag{5.19}$$

Thus, Equation 5.16 becomes:

$$\left\langle \frac{\partial u_i u_j}{\partial x_j} \right\rangle = \frac{\partial << u_i >^f < u_j >^f >}{\partial x_j} - \frac{1}{V} \int\limits_{A_{sf}} < u_i >^f < u_j >^f n_j dA + \left\langle \frac{\partial u'_i u'_j}{\partial x_j} \right\rangle \tag{5.20}$$

For the first term on the right hand side of Equation 5.20, note that $< u_i >^f < u_j >^f$ is a constant over the REV and average of a constant quantity is identical to itself. We choose to retain the integral term in Equation 5.20 as it is not identically zero unless the pore geometry is symmetric. The inertial term now becomes:

$$\left\langle \frac{\partial u_i u_j}{\partial x_j} \right\rangle = \frac{\partial < u_i >^f < u_j >^f}{\partial x_j} + \left\langle \frac{\partial u'_i u'_j}{\partial x_j} \right\rangle - \frac{< u_i >^f < u_j >^f}{V} \int\limits_{A_{sf}} n_j dA \tag{5.21}$$

Here, the second and the third terms on the right hand side cannot be evaluated with the sole knowledge of averaged flow quantities. These are two of the closure terms we will encounter in the final averaged form of the momentum equation. It is useful to note here that the integral term is identically zero for symmetric REV geometries.

Stress Term

For a Newtonian fluid, the stress tensor can be written as:

$$T_{ij} = -p\delta_{ij} + \mu \left(\frac{\partial u_j}{\partial x_i} + \frac{\partial u_i}{\partial x_j} \right) \tag{5.22}$$

Averaging the stress term of the momentum equation by making use of the volume averaging theorem (Equation 5.9):

$$\left\langle \frac{\partial T_{ij}}{\partial x_j} \right\rangle = -\frac{\partial < p >}{\partial x_i} + \mu \frac{\partial}{\partial x_j} \left\langle \frac{\partial u_j}{\partial x_i} + \frac{\partial u_i}{\partial x_j} \right\rangle + \frac{1}{V} \int\limits_{A_{sf}} T_{ij} n_j dA \tag{5.23}$$

For the second term on the right hand side, the volume averaging theorem needs to be applied once more:

$$\frac{\partial}{\partial x_j} \left\langle \frac{\partial u_j}{\partial x_i} + \frac{\partial u_i}{\partial x_j} \right\rangle = \frac{\partial^2 < u_j >}{\partial x_i \partial x_j} + \frac{\partial^2 < u_i >}{\partial x_j^2} + \frac{\partial}{\partial x_j} \left(\frac{1}{V} \int\limits_{A_{sf}} (u_i n_i + u_j n_j) dA \right) \tag{5.24}$$

For incompressible flows, $\frac{\partial < u_j >}{\partial x_j} = 0$ through the volume averaged continuity equation (Equation 5.12). Also note that the integral term is identically zero due to the fact that the fluid velocity is zero at the solid-fluid interface. Thus the stress term becomes:

$$\left\langle \frac{\partial T_{ij}}{\partial x_j} \right\rangle = -\frac{\partial < p >}{\partial x_i} + \mu \frac{\partial^2 < u_i >}{\partial x_j^2} + \frac{1}{V} \int\limits_{A_{sf}} T_{ij} n_j dA \tag{5.25}$$

Using Equations 5.13, 5.21 and 5.25, the averaged momentum equation becomes:

$$
\begin{aligned}
\rho\frac{\partial < u_i >}{\partial t} + \frac{\rho}{\varepsilon^2}\frac{\partial < u_i >< u_j >}{\partial x_j} = & -\frac{\partial < p >}{\partial x_i} + \mu\frac{\partial^2 < u_i >}{\partial x_j} \\
& - \rho\left\langle \frac{\partial u_i' u_j'}{\partial x_j} \right\rangle + \frac{1}{V}\int\limits_{A_{sf}} T_{ij} n_j dA \\
& + \frac{\rho < u_i >^f < u_j >^f}{V}\int\limits_{A_{sf}} n_j dA
\end{aligned}
\tag{5.26}
$$

All the terms of Equation 5.26 except the last three on the right hand side are expressed in terms of averaged velocity components. So, the knowledge of the bulk fluid motion will suffice in evaluating them. However, the remaining three terms require a closure methodology.

Closure of Momentum Equation

Direct computation of Equation 5.26 necessitates complete knowledge of fluid flow throughout the porous media. Most porous media applications require a high number of pores for effective cooling or filtering. Therefore, the direct computation approach is rarely feasible. Answer to this problem has conventionally been to link the closure terms in Equation 5.26 to the Ergun relation (Equation 5.4) as [149]:

$$
\begin{aligned}
\rho\frac{\partial < u_i >}{\partial t} + \frac{\rho}{\varepsilon^2}\frac{\partial < u_i >< u_j >}{\partial x_j} = & -\frac{\partial < p >}{\partial x_i} + \mu\frac{\partial^2 < u_i >}{\partial x_j} \\
& - \frac{\mu}{K} < u_i > - \frac{C_E}{\sqrt{K}}\rho| < u_i > | < u_i >
\end{aligned}
\tag{5.27}
$$

While Equation 5.4 only relates the bulk pressure drop to the total mass flow rate, the solution of Equation 5.27 provides local volume averaged flow field information throughout the porous media. Equation 5.27 is very similar in form to the Navier-Stokes equations. This enables easy handling of conjugate open flow (without porous media) and porous flow problems and permits application of no-slip conditions at the solid walls bounding the solid matrix. By this treatment, the problem is reduced to determination of two parameters, namely, permeability, K, and Ergun coefficient, C_E. Note that there is no fundamental reason for Equation 5.27 to be correct. Both experimental and heuristic methods of estimating the permeability and the Ergun coefficient use the Darcy's Law (Equation 5.1) or Ergun relation (Equation 5.4) as basis, making the rest of the terms in Equation 5.27 stand out as error terms. However, in most tightly packed porous media, momentum loss is largely due to the pore scale flow structures. In these cases, porous source terms are dominant over the other terms in the averaged momentum equation. Thus, generally, Equation 5.27 is expected to closely follow Equation 5.4.

In closing the local volume averaged momentum equation, Whitaker [147] developed a more rigorous method. With the help of a series of scaling arguments, he derived governing equations for the velocity and pressure deviations from the local averaged value. He then developed boundary value problems for permeability and Forchheimer tensors to be solved over a representative, periodic unit-cell of the porous media geometry.

In our multi-scale method, we take a similar but more basic route and directly compute the closure terms appearing in local volume averaged momentum equation (Equation 5.26). We take advantage of the fact that most porous media consist of a matrix of repeating pore patterns. So, instead of computing the flow field in each pore, we try to get away with modeling a single one of each repeating pore patterns observed in a given porous media. The closure terms for each pore model can then be computed for a range of flow speeds, allowing us to construct the closure terms accurately as functions of position and flow speed:

$$\rho\frac{\partial < u_i >}{\partial t} + \frac{\rho}{\varepsilon^2}\frac{\partial < u_i >< u_j >}{\partial x_j} = -\frac{\partial p}{\partial x_i} + \mu\frac{\partial^2 < u_i >}{\partial x_j} + S(x_j, u_j) \tag{5.28}$$

where $S(x_j, u_j)$ is the closure functional established via the multi-scale method. Note that the closure functional acts as a source term in the local volume averaged momentum equation. Thus, existing Navier-Stokes solvers can be used to compute this kind of problems with very little modification for the porous zones. Computational cost associated with this multi-scale approach strongly depends on the level of uniformity and complexity of the pores. For a uniform porous media, only one pore model is needed. In our method, we don't need to refer to the concepts of permeability and the Ergun coefficient. Nonetheless, we can easily derive the expressions for these by comparing Equations 5.26 and 5.27:

$$K = -\mu < u_i > \left[\frac{1}{V} \int\limits_{A_{sf}} T_{ij} n_j dA \right]^{-1} \tag{5.29}$$

$$C_E = \frac{\sqrt{K}}{| < u_i > | < u_i >} \left[\left\langle \frac{\partial u_i' u_j'}{\partial x_j} \right\rangle - \frac{< u_i >^f < u_j >^f}{V} \int\limits_{A_{sf}} n_j dA \right] \tag{5.30}$$

5.2.4 Averaging of the Energy Equation

Consider the fluid phase energy equation with constant specific heat and no heat sources:

$$(\rho c_p)_f \left(\frac{\partial T_f}{\partial t} + \frac{\partial u_i T_f}{\partial x_i} \right) = \lambda_f \frac{\partial^2 T_f}{\partial x_j^2} \tag{5.31}$$

Applying local volume averaging:

$$(\rho c_p)_f \left(\frac{\partial < T_f >}{\partial t} + \left\langle \frac{\partial u_i T_f}{\partial x_i} \right\rangle \right) = \lambda_f \left\langle \frac{\partial^2 T_f}{\partial x_j^2} \right\rangle \tag{5.32}$$

Using Equation 5.9, the diffusive term can be expressed as:

$$\begin{aligned}\lambda_f \left\langle \frac{\partial^2 T_f}{\partial x_j^2} \right\rangle &= \lambda_f \frac{\partial}{\partial x_j} \left\langle \frac{\partial T_f}{\partial x_j} \right\rangle + \frac{\lambda_f}{V} \int\limits_{A_{sf}} n_j \frac{\partial T_f}{\partial x_j} dA \\ &= \lambda_f \frac{\partial^2 < T_f >}{\partial x_j} + \frac{\lambda_f}{V} \frac{\partial}{\partial x_j} \int\limits_{A_{sf}} n_j T_f dA + \frac{\lambda_f}{V} \int\limits_{A_{sf}} n_j \frac{\partial T_f}{\partial x_j} dA\end{aligned} \tag{5.33}$$

Defining a local temperature deviation as:

$$T_f =< T_f >^f + T'_f \tag{5.34}$$

and employing the divergence theorem, the first integral term in Equation 5.33 becomes:

$$\begin{aligned}\int\limits_{A_{sf}} n_j T_f dA &= \int\limits_{A_{sf}} n_j < T_f >^f dA + \int\limits_{A_{sf}} n_j T'_f dA \\ &= \int\limits_{V} \frac{\partial < T_f >^f}{\partial x_j} dV + \int\limits_{A_{sf}} n_j T'_f dA\end{aligned} \tag{5.35}$$

Noting that the variation of an averaged quantity within the averaging volume itself is zero, the first integral vanishes. We then arrive at the averaged diffusion term:

$$\lambda_f \left\langle \frac{\partial^2 T_f}{\partial x_j^2} \right\rangle = \lambda_f \frac{\partial^2 < T_f >}{\partial x_j^2} + \frac{\lambda_f}{V} \frac{\partial}{\partial x_j} \int\limits_{A_{sf}} n_j T'_f dA + \frac{\lambda_f}{V} \int\limits_{A_{sf}} n_j \frac{\partial T_f}{\partial x_j} dA \tag{5.36}$$

Averaging of the convection term yields:

$$\left\langle \frac{\partial u_i T_f}{\partial x_i} \right\rangle = \frac{\partial < u_i T_f >}{\partial x_i} + \frac{1}{V} \int\limits_{A_{sf}} u_i T_f n_i dA \tag{5.37}$$

The integral term on the right hand side vanishes due to no-slip condition at the solid-fluid walls. Using Equation 5.34, we decompose the convection term as:

$$\begin{aligned}\left\langle \frac{\partial u_i T_f}{\partial x_i} \right\rangle &= \frac{\partial}{\partial x_i}\left\langle (< u_i >^f + u'i)(< T_f >^f + T'_f) \right\rangle \\ &= \frac{\partial}{\partial x_i}\left\langle < u_i >^f < T_f >^f + < u_i >^f T'_f + u'_i < T_f >^f + u'_i T'_f \right\rangle\end{aligned} \tag{5.38}$$

Knowing that $< \psi' >= 0$, the volume averaged convection term is obtained:

$$\left\langle \frac{\partial u_i T_f}{\partial x_i} \right\rangle = \frac{\partial < u_i >^f < T_f >^f}{\partial x_i} + \varepsilon \frac{\partial < u'_i T'_f >^f}{\partial x_i} \tag{5.39}$$

Substituting Equation 5.39 and Equation 5.36 in Equation 5.32, we obtain the volume averaged energy equation for the fluid phase:

$$\begin{aligned}&\varepsilon(\rho c_p)_f \left(\frac{\partial < T_f >^f}{\partial t} + \frac{1}{\varepsilon}\frac{\partial < u_i >^f < T_f >^f}{\partial x_i} + \frac{\partial < u'_i T'_f >^f}{\partial x_i} \right) \\ &\quad = \varepsilon \lambda_f \frac{\partial^2 < T_f >^f}{\partial x_j^2} + \frac{\lambda_f}{V}\frac{\partial}{\partial x_j}\int\limits_{A_{sf}} n_j T'_f dA + \frac{\lambda_f}{V}\int\limits_{A_{sf}} n_j \frac{\partial T_f}{\partial x_j} dA\end{aligned} \tag{5.40}$$

Similarly, for the solid phase, the volume-averaged energy equation is:

$$\begin{aligned}&(1-\varepsilon)(\rho c_p)_s \frac{\partial < T_s >^s}{\partial t} \\ &\quad = (1-\varepsilon)\lambda_s \frac{\partial^2 < T_s >^s}{\partial x_j^2} + \frac{\lambda_s}{V}\frac{\partial}{\partial x_j}\int\limits_{A_{fs}} n_j T'_s dA + \frac{\lambda_s}{V}\int\limits_{A_{fs}} n_j \frac{\partial T_s}{\partial x_j} dA\end{aligned} \tag{5.41}$$

In many practical problems, the temperature difference between the solid and fluid phases inside an REV is much smaller than the global scale temperature variation. This condition is met if the REV is much smaller compared to global length scale, there is no heat generation or loss inside the REV and temperature distribution does not vary or vary slowly over time. Under these conditions, we can assume Local

Thermodynamic Equilibrium (LTE) which grants:

$$< T_f >^f = < T_s >^s = < T > \tag{5.42}$$

At the solid-fluid interface, the following boundary conditions apply:

$$T'_f\big|_{A_{sf}} = T'_s|_{A_{sf}} \tag{5.43}$$

$$\lambda_f \frac{\partial T_f}{\partial x_j}\bigg|_{A_{sf}} = \lambda_s \frac{\partial T_s}{\partial x_j}\bigg|_{A_{sf}} \tag{5.44}$$

Also noting that $\mathbf{n}_{sf} = -\mathbf{n}_{fs}$, and adding Equations 5.40 and 5.41, we obtain the local volume averaged energy equation:

$$\begin{aligned}\left[\varepsilon(\rho c_p)_f + (1-\varepsilon)(\rho c_p)_s\right] \frac{\partial < T >}{\partial t} &+ \frac{1}{\varepsilon}(\rho c_p)_f \frac{\partial < u_i >< T >}{\partial x_i} \\ &= \left[\varepsilon \lambda_f + (1-\varepsilon)\lambda_s\right] \frac{\partial^2 < T >}{\partial x_j^2} \\ &+ \frac{\lambda_f - \lambda_s}{V} \frac{\partial}{\partial x_j} \int\limits_{A_{sf}} n_j T'_f dA - \varepsilon(\rho c_p)_f \frac{\partial < u'_i T'_f >^f}{\partial x_i}\end{aligned} \tag{5.45}$$

Equation 5.45 introduces two additional closure terms for non-isothermal problems. Nozad et al. [148] derived governing equations for T'_f and T'_s and introduced constitutive relationships between these temperature deviations and local volume averaged temperature gradient via transformation vectors such as:

$$\begin{aligned} T'_f &= f_i \frac{\partial < T >}{\partial x_i} + \psi \\ T'_s &= g_i \frac{\partial < T >}{\partial x_i} + \xi \end{aligned} \tag{5.46}$$

They then developed boundary value problems for f_i and g_i to be solved over a representative unit-cell.

Amiri and Vafai [157] treated the closure terms in Equation 5.45 as an interfacial heat transfer term between fluid and the solid phases. They used empirical correlations for the specific surface area and heat transfer coefficient to close the energy equation.

We handle the energy closure terms the same way as the momentum equation counterparts with the multi-scale method. The last two terms on the right hand side of Equation 5.45 can be computed over the chosen sample pore models for a range of temperature values. Thus, we can avoid any constitutive or empirical relations by taking a direct approach.

In the current work, we will focus on an isothermal problem. However, we presented the derivation of the local volume averaged energy equation for completeness and as a step towards our goal of simulating the transpiration cooling of the liquid rocket engine injector face plate.

5.3 Numerical Method and Assessment of the Present Porous Media Model

We have shown that the local volume averaged continuity equation is unchanged and momentum equation is very similar in form to the regular Navier-Stokes equations with additional momentum source terms and the convection term modified by a factor of porosity squared, ε^2. Thus a Navier-Stokes solver can easily be modified to account for porous media. The proposed formulation has been implemented in the Loci-Stream code [24]. Porous zones are designated by coordinate ranges and the previously calculated source terms are added to the momentum equation components.

5.3.1 Isothermal Flow through a Drilled Orifice Plate

This test case consists of a porous plate placed in a cylindrical channel as shown in Figure 5.5. The porous material used herein is a metallic plate with an array of

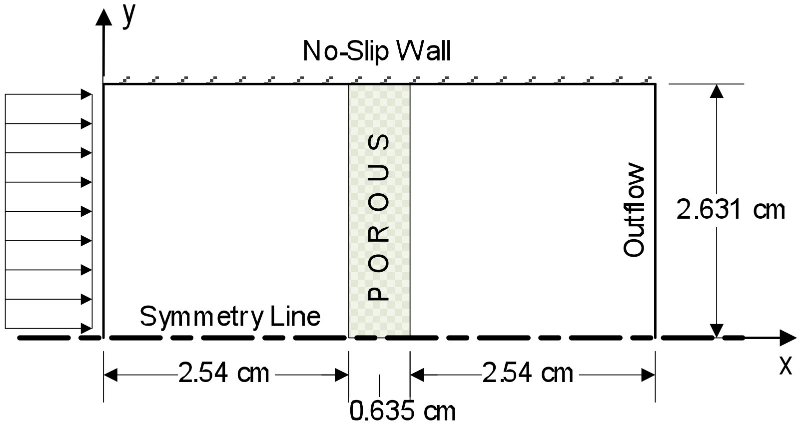

Figure 5.5: Problem domain.

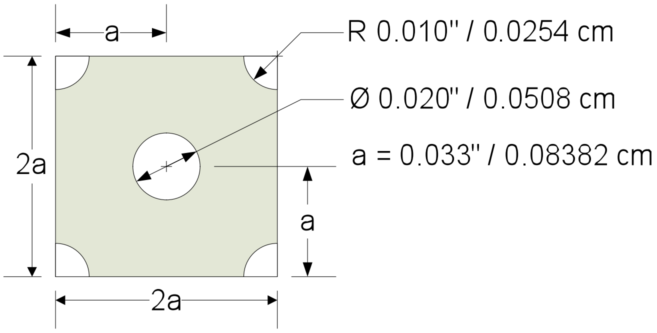

Figure 5.6: Hole pattern details.

uniform and evenly distributed drilled holes. Due to its simple and well defined pore geometry, this case is attractive for testing the multi-scale method developed here. The hole pattern details are shown in Figure 5.6.

This problem was studied before by Tully et al. [154] both numerically and experimentally. The porous plate was inserted in a cylindrical channel test section and pressure drop values were recorded for a range of average flow speeds as summarized in Table 5.1.

Table 5.1: Summary of experimental conditions.

Fluid properties (Air @ 24.2 °C)			Inlet Filter Velocities (m/s)	
Density (ρ)	1.1875	kg/m^3	u_{D_1}	13.1
Dynamic Viscosity (μ)	1.8048E-5	$kg/m.s$	u_{D_2}	16.3
Specific Heat (c_p)	1006.2	$J/kg.K$	u_{D_3}	18.1
Thermal Conductivity (λ)	0.025913	$W/m.K$	u_{D_4}	20.1
			u_{D_4}	20.1
			u_{D_5}	23.3
			u_{D_6}	25.8

Table 5.2: Pore-scale analysis results.

$u_D\,(m/s)$	Re_D	$K\,(m^{-2})$	C_E
13.1	438	2.29×10^{-10}	1.38×10^{-2}
16.3	545	1.92×10^{-10}	1.26×10^{-2}
18.1	605	1.76×10^{-10}	1.21×10^{-2}
20.1	672	1.61×10^{-10}	1.15×10^{-2}
23.3	779	1.43×10^{-10}	1.08×10^{-2}
25.8	862	1.30×10^{-10}	1.03×10^{-2}

Pore Model

The porous metallic plate has a uniform array of circular through holes distributed along its surface. Therefore, the pore shape is simply a circular tube. In order to account for the momentum loss as the flow adjusts to enter the pores, we extend the pore domain for 3 hole diameters towards upstream direction.

Isothermal fluid flow through the pore is computed for the range of flow speeds listed in Table 5.1. Equations 5.29 and 5.30 are evaluated to find the permeability and the Ergun coefficient for each flow speed in conjunction with Equation 5.27 for the global domain. Results of the pore-scale analysis are listed in Table 5.2 which clearly shows that in contrast to the conventional assumption, permeability and the Ergun coefficient vary significantly with changing flow speeds and are not material properties.

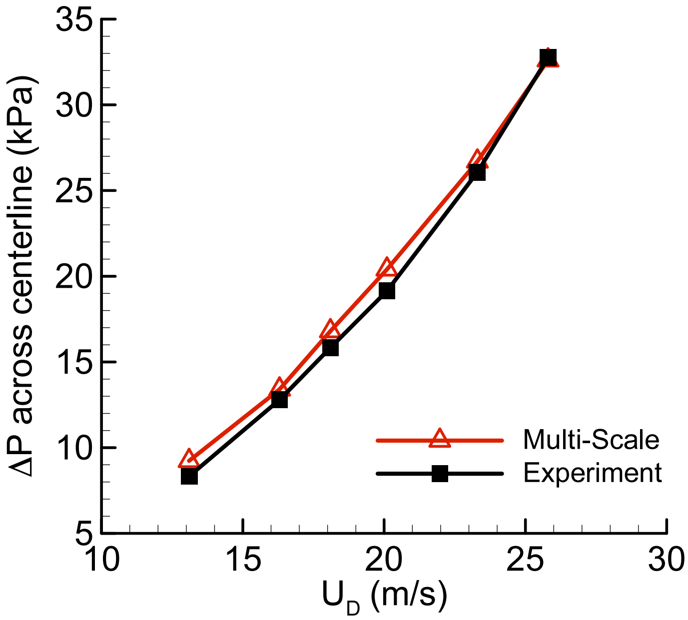

Figure 5.7: Pressure drop across centerline vs. filter velocity.

Global Domain

With the closure parameters obtained via the pore-scale analysis, flow through the global domain as shown in Figure 5.5 is computed. In the porous zone, Navier-Stokes equations are replaced with Equation 5.27. Pressure drop values across the centerline are plotted in comparison to the experimental results by Tully et al. [154] in Figure 5.7.

Figure 5.7 shows that the experimental data is closely reproduced by the multi-scale method. The error relative to the experimental data ranges between 11% and 1% for the lowest and highest flow speeds respectively.

5.4 Summary and Conclusions

A first principle based, multi-scale method is developed for numerical simulations of fluid flow and heat transfer through porous media. In the present model, the effect of porous structures on the global fluid flow is accounted for via local volume averaged governing equations, while the closure terms are accounted for via averaging flow characteristics around the pores. Hence, empirical dependence of simulations is removed without requiring excessive computational cost. The performance of the model has been tested for an isothermal flow case. Both the permeability and Ergun coefficient are shown to be flow properties as opposed to the empirical approach which typically results in constant values of these parameters independent of the flow conditions. Hence, the present multi-scale approach is more versatile and can account for the possible changes in flow characteristics.

For integration of the proposed porous media model into analysis of liquid rocket combustors such as those shown in Chapters 3 and 4, a complete characterization of the Rigimesh material pore structure, as well as validation of the model proposed herein for non-isothermal flows through more complicated porous media is needed.

CHAPTER VI

Conclusions

6.1 Assessment of Computational Fluid Dynamics as an Injector Design Tool

Traditional low fidelity engineering tools have been used for decades for liquid rocket injector design. However, these methods are not always readily applicable to new injector designs or propellant types. Furthermore, they are generally geared towards determining performance and stability characteristics and they offer limited information about the detailed thermal environment within the combustion chamber. As mentioned in Chapter 1, material failure of the combustion chamber and the face plate due to the harsh thermal environment constitute a large part of the engine failure reasons to date [8].

Design by experiments, on the other hand, is a costly and time consuming process. Limited number of cold-flow and hot-fire experiments conducted on subscale, simplified injectors can lead to suboptimal designs and excessive development costs.

Despite increasing popularity of computatioal fluid dynamics (CFD) tools as an aid in the design process, following criteria needs to be met in order to establish CFD as a viable design tool:

1. CFD simulations must have a reasonable turn-around time to enable evaluation

of a large number of design variations.

2. Fidelity and the geometrical complexity/resolution of the CFD model must yield sufficient representation of the physical phenomena.
3. Accuracy of the simulations must be demonstrated and the regimes of applicability must be well understood through validation studies.

Following a review of present turbulent combustion modeling approaches in Chapter 2, a RANS based framework along with two commonly used combustion models, namely the laminar finite-rate chemistry (LFRC) model and the steady laminar flamelet model (SLFM), were adopted consistent with the first goal. The SLFM and the LFRC model represent different compromises between the physics accounted for as well as the computational cost. The LFRC model has no limitation regarding the chemistry speed and it accounts for wall heat transfer and multi-component species diffusion but it disregards the effect of turbulent fluctuations on reaction rates. The SLFM, on the other hand, accounts for these turbulence-chemistry interactions (TCI) at the expense of assumptions such as fast chemistry, adiabatic walls and equal species and thermal diffusivities. These are described in detail in Chapter 2 and summarized in Table 2.2.

Through systematic examination of the simulations performed with these models and validation against experimental data, quantititave characterization of individual modeling aspects such as the turbulence-chemistry interactions, chemical non-equilibrium and near wall turbulence treatment is achieved. Two different experimental H_2/O_2 single element shear coaxial injectors due to Vaidyanathan et al. [117] and Pal et al. [116] as well as a 7-element experimental injector due to deRidder et al. [122; 123; 124] were used as benchmark cases.

CFD simulations of liquid rocket combustors, such as those presented herein, offer greater fidelity, generality and detailed data compared to the traditional engineering analyses which in general either incorporate simplified physics and/or are based on previously tested design configurations. While it may not replace the experimentation entirely, CFD could change the paradigm of design by experimentation to the one where tests are used to validate the CFD aided designs.

This thesis contributes to the achievement of the goals listed above by:

- Evaluating modeling strategies that yield reasonable computational cost and hence allow a practical CFD based design approach,
- Assessing the grid resolution requirements and quantifying the importance of individual physical and numerical phenomena such as chemical reaction mechanism choice, chemical non-equilibrium, turbulence-chemistry interactions and turbulence wall treatment in the context of several different experimental injectors,
- Developing new methodologies which represent increased fidelity, generality and improved accuracy (e.g. multi-scale porous media model presented in Chapter 5, zonal turbulence wall treatment presented in Chapter 3),
- Validating the CFD results against experimental measurements and discussing the reasons for shortcomings while pointing out future directions toward overcoming those.

The main findings are summarized in Table 6.1 and discussed in more detail below.

Chemistry Mechanism and Non-equilibrium Effects

Four different H_2/O_2 chemistry mechanisms were selected and tested for the Vaidyanathan et al. [117] injector whereas two of them were evaluated for the Pal et al. [116] injector. The simulation results were identical for the former injector whereas a minimal difference was observed for the latter one. To analyze the time

Table 6.1: Main findings.

Chemical Non-Equilibrium

- For the high pressure injectors with H_2/O_2 propellants such as those analyzed herein, the chemical-non-equilibrium effects were found to be unimportant.
- Due to the fast chemistry, chemical equilibrium is attained within a fluid flow time scale.
- Assumed PDF/equilibrium combustion models can be used in favor of computational cost savings.

Turbulence-Chemistry Interactions (TCI)

- TCI effect is substantial in regions with large gradients in composition such as near the injector element exit and the stoichiometric flame surface.
- In single element injectors, near wall field, hence the wall heat flux distributions are only slightly affected by TCI.
- In multi-element injectors, due to closer wall-injector proximity, TCI may alter the near wall field significantly.
- TCI effect should not be disregarded (as in the LFRC model) in the analysis of such flows.

Near Wall Turbulence Treatment

- Has a major impact in wall heat transfer prediction accuracy.
- Low-Re model performs better in separated flow regions.
- Law-of-the-wall method performs better in attached flow regions.
- A zonal approach blending the two models based on flow attachment improves overall performance.

Numerical Choices

- With the lack of chemical non-equilibrium effects, solutions are insentitive to the choice of different chemistry mechanisms, as demonstrated for the single element injector test cases.
- Increased grid resolution, until the grid insensitive level is reached, causes the flame to shift downstream (slower mixing). Wall heat flux distribution predictions are less sensitive to grid refinement.
- In CFD simulations of new injector designs, chamber wall temperature distribution is not known a-priori. An isothermal boundary condition for the chamber wall is found to be acceptable.

Validation

- In light of the findings listed above, good agreement between the experimental wall heat flux measurements and the results of the current modeling framework was obtained for the single element injector test cases.
- The heat flux predictions were also comparable to the highest fidelity/resolution method results presented in Tucker et al. [115]
- The validation for the multi-element injector case is inconclusive. The use of the zonal wall treatment and correct equation of state to represent liquid oxygen density at the injector exit need to be assessed.

scales associated with each mechanism, thermodynamic state and mixture composition at a local near-flame point from the Vaidyanathan et al. [117] injector solution was sampled. O_2 mass fraction in the fuel-rich mixture was perturbed and the time history of the response of each mechanism while reaching a new equilibrium state was observed. The time scale for the chemistry was found to be much smaller than the local convective and diffusive time scales.

With the SLFM, the scalar dissipation rate distribution offers a global look into chemical non-equilibrium effects. For both the Pal et al. [116] injector and the multi-element injector, the non-equilibrium chemistry effects were found to be constrained to a small region near the injector exit. Furthermore, in that region, quenching limit was not approached. Thus the following is concluded for the high pressure H_2/O_2 injector type problems such as those presented herein:

- Due to the fast nature of H_2/O_2 chemistry, non-equilibrium effects are minimal.
- In steady state analysis, assumed PDF/equilibrium models can be used in favor of cost savings.

On the other hand, for analysis of transient phenomena such as ignition and combustion stability, or for hydrocarbon flames where slow processes exist and radical prediction is targeted, chemical non-equilibrium effects need to be accounted for.

Turbulence-Chemistry Interactions

The effect of turbulent fluctuations on chemical reaction rates are neglected in the LFRC model. In contrast, the SLFM offers an implicit account of the turbulence-chemistry interaction (TCI) effects through the use of presumed shape PDF's. For the Pal et al. [116] injector, following simulation results were compared:

- LFRC with adiabatic walls
- SLFM with β PDF for Z and lognormal PDF for χ (TCI on, non-equilibrium)

- SLFM with β PDF for Z and $\chi \rightarrow 0$ (TCI on, equilibrium)
- SLFM with Dirac-δ PDF for Z and Dirac-δ PDF for χ (TCI off, non-equilibrium)
- SLFM with Dirac-δ PDF for Z and $\chi \rightarrow 0$ (TCI off, equilibrium)

These comparisons provided a quantitative look into the extent of TCI effect over the whole flow field. The effect was shown to be significant near the flame surface (in regions where the mixture composition is close to stoichiometric conditions). It was especially more pronounced near the injector exits where the shear layer between the fuel and oxidizer streams is stronger. Temperature was reduced significantly in these regions due to TCI. For the Pal et al. [116] case, near wall PDF distributions of the mixture fraction and scalar dissipation rate resulting from the SLFM simulations were examined. In this single element injector setup, the fuel-rich near wall mixture composition field exhibited slow spatial variations corresponding to narrow mixture fraction PDF's with mean values away from the stoichiometric conditions towards the rich side. Therefore the near wall temperature field was not directly altered by TCI effects.

In the multi-element injector case based on the experimental configuration of deRidder et al. [122; 123; 124], the near wall composition variations were steeper due to closer proximity of the outer row flame surface to the wall (in comparison to the single element injector setup of Pal et al. [116]). This corresponds to wider near wall mixture fraction PDF's but the mean values were in this case even further away from the stoichiometric value. As a result, local near wall TCI effect was negligible. Note that this is only a localized look. In a global sense, near flame alterations of the mixture composition and temperature may affect the overall flow structure and hence the thermal field. For example, in the multi-element injector simulations, the LFRC model and the SLFM predicted the phenomena of a near wall fuel-rich stream slightly differently. As a result, the SLFM prediction of the wall heat flux distribution along the inline plane (the symmetry plane crossing an outer row element) was in significantly better agreement with the experimentally measured distribution.

In summary:

- TCI effect alters the flow and thermal fields significantly. The effect is especially pronounced near the flame surface.
- In the single element injector setups, where the injector element to wall distance is usually large, near wall flow fields were slightly affected by TCI.
- In more realistic multi-element injectors, closer flame-wall promixity increases the impact of TCI on wall heat flux predictions.
- In the tested single element injector problem, the non-equilibrium chemistry effect was unimportant regardless of TCI. As noted before, this is due to the fast nature of the H_2/O_2 chemistry and the high pressure combustion chamber.

Turbulence Wall Treatment

An assessment of the alternative turbulence wall treatment choices, namely the Low-Reynolds number modification of the turbulence model and the law-of-the-wall method, was performed for the Pal et al. [116] injector. Although the choice was shown to have little impact on the overall flow and thermal fields, the localized near wall changes caused largely different wall heat flux distributions. The turbulence wall treament was by far the most influential factor in determining the accuracy of the wall heat flux predictions in comparison to the experimental results.

The low-Re modification of the turbulence model mimics the damping of near wall turbulence via what boils down to a reduction in computed eddy viscosity based on the distance to the wall. This damping of the eddy viscosity is empirically calibrated with the hope of applicability to a large number of different cases.

Law-of-the-wall approach has a fundamental limitation in regions where a recirculating flow structure or large streamline curvatures exist near the wall. The end result was shown to be a significant under prediction of the wall heat flux values in these scenarios, typically occurring in upstream portions of the wall in the injector type problems. However, the law-of-the-wall approach yielded improved accuracy elsewhere compared to the low-Re model results whereas the latter performed better near the recirculation zones. A zonal treatment based on flow attachment was shown to significantly improve the prediction.

Wall Thermal Boundary Conditions

In CFD predictions of a combustor concept for which experimental data is not available, the temperature distribution at the wall is not known a-priori. For the Pal et al. [116] injector, sensitivity of computed wall heat flux distribution to the choice of either imposing the experimentally measured wall temperature distribution or imposing a uniform temperature was tested. While slight differences on the heat flux distributions, particularly in peak locations, were observed, the overall agreement was acceptable. Furthermore, total heat transfer to the wall was unchanged.

Laminar Finite-Rate Chemistry (LFRC) Model versus Steady Laminar Flamelet Model (SLFM)

Overall, the simulations with the two models yielded consistent results. In fact, it was shown that the two models produced nearly identical results when the differences in underlying assumptions and capabilities of the two models were eliminated by:

- Using Dirac-δ PDF's for Z and χ in the SLFM model in order to turn-off the TCI effect,

- Using adiabatic wall boundary conditions for the LFRC model,

- Matching species and thermal transport properties between the two models.

Compared to the SLFM, the LFRC model offers generality in terms of the chemistry speed, boundary conditions and the species transport. The first was shown to be unimportant for the current problem types of interest. In cases where the wall heat loss is small compared to the total heat generated via the chemical reactions (which was the case for the multi-element injector test case), the adiabatic wall limitation of the SLFM can also be overcome by utilizing the proposed method of post estimation of the wall heat flux. On the other hand, the SLFM accounts for the TCI unlike the LFRC model and offers large savings in computational cost. Thus, the SLFM, or the assumed PDF/equilibrium model for even further computational cost savings, is seen suitable for CFD based injector design tasks where a large number of design variations need to be tested.

6.2 Element-to-Element Interactions in Multi-element Injector Configurations

Based on the experimental 7-element injector due to deRidder et al. [122; 123; 124], a parametric study was performed using the SLFM. In the experimental setup, 6 injector elements were placed in a circular arrangement surrounding a central element. The number of elements on the outer row (N_{oe}) and the radius of the outer row (R_{oe}) were varied while keeping the total mass flow rates of fuel and oxidizer constant. Corresponding effects on flame length and adiabatic wall temperature, providing measures of performance and reliability respectively, were observed for a total of 13 different injector configurations. The resulting flame length and peak adiabatic wall temperature data were fitted with 2^{nd} order polynomial response surfaces (PRS).

A fairly monotonic increase of the flame length with increased R_{oe} was observed while it was less sensitive to variations in N_{oe}. However, for the test case with the smallest R_{oe} and the largest N_{oe} (representing the smallest circumferential distance between outer row elements), flame surfaces of the two subsequent elements in the outer row merged, causing an extension of the flame length.

The low order trend for the peak adiabatic wall temperature observed from the PRS suggests a monotonic decrease with decreased N_{oe}, and relative insensitivity to R_{oe}. This is in contrast to the behavior of the flame length. However, large non-monotonic variations of the peak wall temperature with R_{oe} occur. This non-monotonic dependence of the peak wall temperature is linked to two competing effects: flame surface to wall proximity with increased R_{oe} and angling of the outer jet towards the wall (result of the interaction with central jet) with decreased R_{oe}. Both result in increased wall temperature, suggesting that an optimum R_{oe} location exists. Increased number of simulation points in the DOE together with either a higher order PRS or other fitting methodologies such as Kriging [126] are needed to accurately determine the optimum location.

6.3 Proposed Methodologies

6.3.1 Zonal Near Wall Treatment of Turbulence

Depending on the near wall flow structure, alternative near wall turbulence treatment approaches, i.e. the low-Re model and the law-of-the-wall formulation, exhibited improved accuracy over the other in predicting the wall heat flux distribution. A blend of the two based on flow attachment to the wall was explored in Chapter 3 and this zonal wall treatment approach was shown to improve the overall agreement with experimental wall heat flux measurements significantly.

6.3.2 Estimation of Wall Heat Flux for the Flamelet Model

Strictly speaking, heat loss through the walls is not allowed in the SLFM as explained in Chapter 2. However, the LFRC simulation results for the multi-element injector revealed that the total heat loss to the wall is only about 1% of the heat generated through the chemical reactions. Assuming that the heat loss effects are contained within a thin layer near the wall, a methodology for obtaining wall heat flux distribution as a post processing step was described in Chapter 4. The methodology is based on the law-of-the-wall formulation and hence it is strictly only valid in regions where the flow is attached to the wall and no significant streamline curvatures or wall normal pressure gradients exist.

6.3.3 A Multi-Scale Model for Flows through Porous Media

Modeling efforts for porous media flows to date mostly aimed at empirically correlating the pore level flow effects to the bulk fluid motion. The empirical constants, permeability and Ergun coefficient, involved in a widely used model are commonly assumed to be constant properties for a given porous material.

In Chapter 4, a multi-scale methodology which eliminates the empiricism from the simulations was developed. Local volume averaged equations governing the bulk flow were derived. Resulting closure terms were directly calculated for representative pore shapes via pore-level simulations conducted for a varying range of flow rates. The method was validated against experimental data for an iso-thermal flow through a metallic plate with evenly distributed drilled holes. Close agreement with the experimental data of pressure drop vs. mean flow speed was achieved. In addition, both the permeability and Ergun coefficient were shown to be flow dependent.

6.4 Future Work

- The zonal near wall treatment is a promising concept. But currently, the reattachment point location is detected manually via inspection of a simulation using either the low-Re model or the law-of-the-wall. The near wall grid is then re-adjusted for split treatment as explained in Chapter 3. This procedure needs to be automated and incorporated into the Loci-Stream [22] code for direct application.

- A methodology to estimate wall heat flux distribution using the law-of-the-wall formulation as post processing step to the flamelet model simulations was presented in Chapter 4. The methodology relies on the flow properties at a chosen near wall reference point. In the current analyses, the reference point at all axial locations was at a uniform distance from the wall. An automated, local selection of this point based on the velocity boundary layer height is suggested for future applications.

- In the multi-element injector test case analyzed in Chapter 4, O_2 enters the injector nozzle in liquid phase. The ideal gas law utilized in the current analyses yield to gross under prediction of the inlet oxygen density. While the total O_2 mass flux is fixed as a boundary condition, the injection velocity would be largely different if the liquid phase of the O_2 was accounted for. Usage of a real fluid equation state preserving accuracy at both the cryogenic liquid and high temperature supercritical states is needed.

- Current experimental studies utilized herein for validation concentrate largely on the wall heat transfer data. More comprehensive validation data probing the detailed flow field and flame structure is desirable for more conclusive analyses.

- The development of the multi-scale porous media model was intended for the analysis of fuel flow through porous materials used for the injector face plate in some liquid rocket engines. In the case of SSME and P&W RL10 engine, Rigimesh material is used [127]. A complete characterization of the Rigimesh material pore structure, as well as validation of the proposed model for non-isothermal flows through more complicated porous media are needed.

BIBLIOGRAPHY

BIBLIOGRAPHY

[1] Sutton, G. P. and Biblarz, O., *Rocket Propulsion Elements*, Wiley-Interscience, 7th ed., 2000.

[2] Huzel, D. K. and Huang, D. H., *Modern Engineering for Design of Liquid-Propellant Rocket Engines*, AIAA Progress in Astronautics and Aeronautics, 1992.

[3] Quinn, J. E., "Cost Trade-Off for a Pressure Fed Liquid Rocket to LEO," *AIAA Paper 1999-2622*, 1999.

[4] Cotta, R. B., Eckmann, J. B., and Matuszak, L. W., "Upper Stage Options for Reusable Launch Vehicles," *AIAA Paper 1996-3015*, 1996.

[5] Krach, A. E. and Sutton, A. M., "Another Look at the Practical and Theoretical Limits of an Expander Cycle, LOX/H2 Engine," *AIAA Paper 2000-3287*, 2000.

[6] Parsley, R. C. and Crocker, A. M., "The RL200 - Incorporating a Balanced Approach for Reusable Propulsion Safety," *AIAA Paper 2000-3287*, 2000.

[7] Sutton, G. P., *History of Liquid Propellant Rocket Engines*, AIAA, 2006.

[8] Tucker, P. K., Rybak, J. A., Hulka, J. R., Jones, G. W., Nesman, T., and West, J. S., "The NASA Constellation University Institutes Project: Thrust Chamber Assembly Virtual Institute," 42nd AIAA/ASME/SAE/ASEE Joint Propulsion Conference, AIAA-2006-4524, 2006.

[9] Gill, G. S., "Liquid Rocket Engine Injectors," *NASA/SP-8089*, 1976.

[10] Bittker, D. A., "An Analytical Study of Turbulent and Molecular Mixing in Rocket Combustion," *NACA TN 4321*, 1958.

[11] Priem, R. J. and Heidmann, M. F., "Propellant Vaporization as a Design Criterion for Rocket-Engine Combustion Chambers," *NASA-TR-R-67*, 1959.

[12] Pavli, A. L., "Design and Evaluation of High Performance Rocket Engine Injectors for Use with Hydrocarbon Fuels," *NASA TM-79319*, 1979.

[13] Knuth, W. H., Gramer, D. J., and St. Clair, C. P., "Premixing Rocket Engine Injectors for High Pressure Gaseous Oxygen and Hydrogen," *AIAA Paper 1999-2491*, 1999.

[14] Rupe, J., "An Experimental Correlation of the Nonreactive Properties of Injection Schemes and Combustion Effects in a Liquid-Propellant Rocket Engine," *NASA TR 32-255*, 1965.

[15] Burick, R. J., "Space Storable Propellant Performance Program Coaxial Injector Characterization," *NASA-CR-120936*, 1972.

[16] Zinner, W., Haeseller, D., Mäding, C., Rubinskji, V., Gorochov, V., Hrisanfov, S., and Nikulin, G., "Development of Advanced Technologies for Future Cryogenic Thrust Chamber Applications," *AIAA Paper 1997-3312*, 1997.

[17] Vaidyanathan, R., Tucker, P. K., Papila, N., and Shyy, W., "CFD-Based Design Optimization for a Single Element Rocket Injector," *Journal of Propulsion and Power*, Vol. 20, No. 4, 2004, pp. 705–717.

[18] Myers, R. H. and Montgomery, D. C., *Response Surface Methodology Process and Product Optimization Using Designed Experiment*, John Wiley & Sons, 1995.

[19] Mack, Y., Haftka, R., Segal, C., Queipe, N., and Shyy, W., "Computational Modeling and Sensitivity Evaluation of Liquid Rocket Injector Flow," 43rd AIAA/ASME/SAE/ASEE Joint Propulsion Conference & Exhibit, AIAA-2007-5592, 2007.

[20] Luke, E. A. and George, T., "Loci : A Rule-based Framework for Parallel Multidisciplinary Simulation Synthesis," *Journal of Functional Programming*, Vol. 15, No. 3, 2005, pp. 477–502.

[21] Luke, E. and Cinnella, P., "Numerical Simulations of Mixtures of Fluids Using Upwind Algorithms," *Computers and Fluids*, Vol. 36, No. 10, 2007, pp. 1547–1566.

[22] Thakur, S., Wright, J., and Shyy, W., "An Algorithm for Chemically Reacting Flows on Generalized Grids Using a Rule-Based Framework," 43rd AIAA Conference, Paper No. 2005-0875, 2005.

[23] Thakur, S. and Wright, J., "Validation of a Pressure-based Combustion Simulation Tool for a Single Element Injector Test Problem," 3rd International Workshop on Rocket Combustion Modeling, Paris, France, 2006.

[24] Kamakoti, R., Thakur, S., Wright, J., and Shyy, W., "Validation of a New Parallel All-Speed CFD Code in a Rule-Based Framework for Multidisciplinary Applications," 36th AIAA Fluid Dynamics Conference and Exhibit, AIAA 2006-3063, 2006.

[25] Poinsot, T. and Veynante, D., *Theoretical and Numerical Combustion*, Edwards, 2001.

[26] Hirschfelder, J. O., Buehler, R. J., McGee, H. A., and Sutton, J. R., "Generalized Equation of State for Gases and Liquids," *Ind Eng Chem*, Vol. 50, 1958, pp. 375–385.

[27] Hirschfelder, J. O., Buehler, R. J., McGee, H. A., and Sutton, J. R., "Correction: Generalized Equation of State for Gases and Liquids," *Ind Eng Chem Fundam*, Vol. 1, 1962, pp. 224.

[28] Chase, M. W. J., *NIST-JANAF Thermochemical Tables*, 4th ed.

[29] Kee, R. J., Rupley, F. M., and Miller, J. A., "Chemkin II: A Fortran Chemical Kinetic Package for Modeling Well-stirred Reactors," *Sandia National Laboratories, SAND 89-8009B*, 1989.

[30] Pope, S. B., *Turbulent Flows*, Cambridge University Press, 2000.

[31] Favre, A., *Statistical Equations of Turbulent Gases*, SIAM, Philadelphia: In SIAM, editor, Problems of Hydrodynamics and Continuum Mechanics, 1969.

[32] Kuo, K. K., *Principles of Turbulent Combustion*, Wiley, 2nd ed., 2005.

[33] Wilcox, D. C., *Turbulence Modeling for CFD*, DCW Ind., La Canada, CA, 1998.

[34] Spalart, P. R., "Strategies for Turbulence Modelling and Simulations," *International Journal of Heat and Fluid Flow*, Vol. 21, 2000, pp. 252–263.

[35] Launder, B. E., Reece, G. J., and Rodi, W., *Progress in the Development of a Reynolds-stress Turbulence Closure*, Journal of Fluid Mechanics Digital Archive, Cambridge Univ. Press, 2006.

[36] Smagorinsky, J., "General Circulation Experiments with the Primitive Equations: I. The Basic Equations," *Mon. Weather Rev.*, Vol. 91, 1963, pp. 99–164.

[37] Lilly, D. K., "The Representation of Small Scale Turbulence in Numerical Simulation Experiments," *H. H. Goldestine (Ed), Proc. IBM Scientific Computing Symp. In Environmental Sciences*, 1967, pp. 195–210.

[38] Deadorff, J. W., "A Numerical Study of Three-dimensional Turbulent Channel Flow at Large Reynolds Numbers," *J. Fluid Mech.*, Vol. 41, 1970, pp. 453–480.

[39] Bilger, R. W., Pope, S. B., Bray, K. N. C., and Driscoll, J. F., "Paradigms in Turbulent Combustion Research," *Proceedings of the Combustion Institute*, Vol. 30, 2005, pp. 21–42.

[40] Jones, W. P. and Launder, B. E., "The Prediction of Laminarization with a Two-equation Model of Turbulence," *International Journal of Heat and Mass Transfer*, Vol. 15, 1972.

[41] Wilcox, D. C., "Re-assesment of the Scale-determining Equation for Advanced Turbulence Models," *AIAA Journal*, Vol. 26, 1988, pp. 1414–1421.

[42] Menter, F. R., "Influence of freestream values on $k-\omega$ turbulence model predictions," *AIAA Journal*, Vol. 30, No. 6, 1992.

[43] Menter, F. R., "Zonal Two Equation $k-\omega$ Turbulence Models for Aerodynamic Flows," *AIAA Paper 93-2906*, 1993.

[44] Kestin, J. and Richardson, P. D., "Heat Transfer Across Turbulent, Incompressible Boundary Layers," *Int. J. Heat Mass Transfer*, Vol. 6, 1963, pp. 147–189.

[45] Spalding, D. B., "A Single Formula for the Law of the Wal," *Transactions of the ASME, Series E: Journal of Applied Mechanics*, Vol. 5, No. 17, 1961.

[46] Nichols, R. H. and Nelson, C. C., "Wall Function Boundary Conditions Including Heat Transfer and Compressibility," *AIAA Journal*, Vol. 42, 2004, pp. 1107–1114.

[47] White, F. M. and Christoph, G. H., "A Simple Analysis of Compressible Turbulent Two-dimensional Skin Friction Under Arbitrary Conditions," *AFFDL-TR-70-133, Wright Patterson AFB, OH*, 2004.

[48] Cox, C., *An Efficient Solver for Flows in Local Chemical Equilibrium*, PhD thesis, Mississippi State University, 1992.

[49] Luke, E. A., *A Rule-Base Specification System for Computational Fluid Dynamics*, PhD thesis, Mississippi State University, 1999.

[50] Vincenti, W. G. and Kruger, C. H., *Introduction to Physical Gas Dynamics*, Krieger Publishing Company, 1965. Reprinted, 1986.

[51] Lewis, B. and Von Elbe, G., *Combustion, Flames and Explosions of Gases*, Academic Press, 1987.

[52] Peters, N., *Turbulent Combustion*, Cambridge University Press, 2000.

[53] Lundgren, T. S., "Distribution Function in the Statistical Theory of Turbulence," *Phys. Fluids*, Vol. 10, 1967.

[54] O'Brien, E. E., "The Probability Density Function (PDF) Approach to Reacting Turbulent Flows," *in Libby P. A., Williams, F. A., editors, Turbulent Reacting Flows,Springer-Verlag, Berlin*, 1980, pp. 185–218.

[55] Pope, S. B., "PDF Methods for Turbulent Reactive Flows," *Prog. Energy Combust. Sci.*, Vol. 11, 1985, pp. 119–192.

[56] Pope, S. B., "Computations of Turbulent Combustion: Progress and Challenges," *23rd Symposium (International) on Combustion, The Combustion Institute, Pittsburg*, 1990, pp. 591–612.

[57] Dopazo, C., "Recent Developments in PDF Methods," *in Libby P.A., Williams, F.A., editors, Turbulent Reacting Flows, Academic Press, London, 1994*, 1994, pp. 375–474.

[58] Bilger, R. W., "Turbulent Flows with Nonpremixed Reactants," *in Libby P. A., Williams, F. A., editors, Turbulent Reacting Flows, Springer-Verlag, Berlin*, 1980, pp. 65–113.

[59] Gibson, C. H. and Masiello, P. J., "Observations of the Variability of Dissipation Rates of Turbulent Velocity and Temperature Fields," *Lecture Notes in Physics, Springer-Verlag*, Vol. 12, 1972, pp. 427–448.

[60] Antonia, R. A. and Sreenivasan, K. R., "Log-normality of Temperature Dissipation in a Turbulent Boundary Layer," *Phys. Fluids*, Vol. 20, 1977, pp. 1800.

[61] Peters, N., "Local Quenching Due to Flame Stretch and Non-Premixed Turbulent Combustion," *Combust. Sci. Technol.*, Vol. 30, 1983, pp. 1–17.

[62] Peters, N., "Laminar Diffusion Flamelet Models in Non-premixed Turbulent Combustion," *Prog. Energy Combust Sci.*, Vol. 10, 1984, pp. 319–339.

[63] Klimenko, A. Y., "Multicomponent Diffusion of Various Scalars in Turbulent Flows," *Fluid Dyn.*, Vol. 25, 1990, pp. 327–334.

[64] Bilger, R. W., "Conditional Moment Closure for Turbulent Reacting Flows," *Phys. Fluids A5*, 1990, pp. 436–444.

[65] Burke, S. P. and Schumann, T. E. W., "Diffusion flames," *Ind. Eng. Chem.*, Vol. 20 (10), 1980, pp. 998–1004.

[66] White, W. B., Johnson, S. M., and Dantzig, G. B., "Chemical Equilibrium in Complex Mixtures," *J. Chem. Phys.*, Vol. 28, 1958, pp. 751.

[67] Janicka, J. and Kollman, W., "A Two-variable Formalism for the Treatment of Chemical Reactions in Turbulent H2-Air Diffusion Flames," *17th Symposium (International) on Combustion, The Combustion Institute, Pittsburg*, 1979, pp. 421–431.

[68] Correa, S. M. and Shyy, W., "Computational Models and Methods for Continuous Gaseous Turbulent Combustion," *Prog. Energy Combust. Sci.*, Vol. 13, 1987, pp. 249–292.

[69] Libby, P. A. and Williams, F. A., *Turbulent Reacting Flows*, Academic Press, 1994.

[70] Veynante, D. and Vervisch, L., "Turbulent Combustion Modeling," *Progress in Energy and Combustion Science*, Vol. 28, 2002, pp. 193–266.

[71] Janicka, J. and Peters, N., "Prediction of Turbulent Jet Diffusion Flame Lift-off Using a PDF Transport Equation," *19th Symp. (Int.) on Combustion, The Combustion Institute, Pittsburg*, 1982, pp. 367–374.

[72] Meyers, R. E. and O'Brien, E. E., "The Joint PDF of a Scalar and Its Gradient at a Point in a Turbulent Fluid," *Combust. Sci. Technol.*, Vol. 26, 1981, pp. 123–134.

[73] Effesberg, E. and Peters, N., "Scalar Dissipation Rates in Turbulent Jets and Jet Diffusion Flames," *22nd Symp. (Int.) on Combustion, The Combustion Institute, Pittsburg*, 1988, pp. 693–700.

[74] Pitsch, H., Chen, M., and Peters, N., "Unsteady Flamelet Modeling of Turbulent Hydrogen-Air Diffusion Flames," *Proc. Combust. Inst.*, Vol. 27, 1998, pp. 1057–1064.

[75] Pitsch, H., "Unsteady Flamelet Modeling of Differential Diffusion in Turbulent Jet Diffusion Flames," *Combustion and Flame*, Vol. 123, No. 3, 2000, pp. 358–374.

[76] Pierce, C. D. and Moin, P., "Progress-variable Approach for Large Eddy Simulation of Non-Premixed Turbulent Combustion," *J. Fluid Mech.*, Vol. 504, 2004, pp. 73–97.

[77] Ihme, M., Cha, C. M., and Pitsch, H., "Prediction of Local Extinction and Re-ignition Effects in Non-premixed Turbulent Combustion Using a Flamelet/Progress Variable Approach," *Proc. Comb. Inst.*, Vol. 30, 2005, pp. 793.

[78] Cuenot, B. and Poinsot, T. J., "Effects of Curvature and Unsteadiness in Diffusion Flames. Implications for Turbulent Diffusion Combustion," *25th Symp. (Int.) on Combustion, The Combustion Institute, Pittsburg*, 1994, pp. 1383–1390.

[79] Buriko, Y. Y., Kuznetsov, V. R., Volkov, D. V., Zaitsev, S. A., and Uryvsky, A. F., "Test of a Flamelet Model for Turbulent Non-premixed Combustion," *Combustion and Flame*, Vol. 96, 1994, pp. 104–120.

[80] Mauss, F., Keller, D., and Peters, N., "A Lagrangian Simulation of Flamelet Extinction and Re-ignition in Turbulent Jet Diffusion Flames," *23rd Symp. (Int.) on Combustion, The Combustion Institute, Pittsburg*, 1990, pp. 693–698.

[81] Bray, K. N. C. and Peters, N., "Laminar Flamelets in Turbulent Flames," *in Libby P.A., Williams, F.A., editors, Turbulent Reacting Flows, Academic Press, London*, 1994, pp. 63–113.

[82] Marracino, B. and Lentini, D., "Radiation Modeling in Non-luminous Non-premixed Turbulent Flames," *Combust. Sci. Technol.*, Vol. 128, 1997, pp. 23–48.

[83] Hossain, M., Jones, J. C., and Malalasekera, M., "Modeling of Bluff-body Nonpremixed Flame Using a Coupled Radiation/Flamelet Combustion Model," *Flow. Turbul. Combust.*, Vol. 67, 2001, pp. 217–234.

[84] Pitsch, H., "Large-eddy Simulation of Turbulent Combustion," *Annual Review of Fluid Mechanics*, Vol. 38, 2006, pp. 453–482.

[85] Ihme, M. and Pitsch, H., "Modeling of Radiation and Nitric Oxide Formation in Turbulent Nonpremixed Flames Using Flamelet/Progress Variable Formulation," *Physics of Fluids*, Vol. 20,055110, 2008.

[86] di Madre, F., Jones, W. P., and Menzies, K. R., "Large Eddy Simulation of a Model Gas Turbine Combustor," *Combust. Flame*, Vol. 137, 2004, pp. 278.

[87] Renfro, M. W., Chaturved, A., King, G. B., Laurendeau, N. M., Kempf, A., Dreizler, A., and Janicka, J., "Comparison of OH Time-series Measurements and Large-eddy Simulations in Hydrogen Jet Flames," *Combust. Flame*, Vol. 139, 2004, pp. 142.

[88] Kempf, A., Flemming, F., and Janicka, J., "Investigation of Lengthscales, Scalar Dissipation, and Flame Orientation in a Piloted Diffusion Flame by LES," *Proc. Combust. Inst.*, Vol. 30, 2005, pp. 557.

[89] Stein, O. and Kempf, A., "LES of the Sydney Swirl Flame Series: A Study of Vortex Breakdown in Isothermal and Reacting Flows," *Proc. Combust. Inst.*, Vol. 31, 2007, pp. 1755.

[90] Blazek, J., *Computational Fluid Dynamics: Principles and Applications*, Elsevier Ltd., The Netherlands, 2001.

[91] Venkatakrishnan, V., "On the Accuracy of Limiters and Convergence to Steady State Solutions," *AIAA paper No. 93-0880*, 1993.

[92] Walters, R. W., Cinella, P., Slack, D. C., and Halt, D., "Characteristic-based Algorithms for Flows in Thermodynamic Nonequilibrium," *AIAA Journal*, Vol. 30, 1992, pp. 1304–1313.

[93] Einfeldt, B., "On Godunov-type Method for Gas Dynamics," *SIAM Journal on Numerical Analysis*, Vol. 25, 1988, pp. 294–318.

[94] Patankar, S. V., *Numerical Heat Transfer and Fluid Flow*, Hemisphere, Washington, DC, 1980.

[95] Thakur, S., Wright, J., and Shyy, W., *Stream: A Computational Fluid Dynamics and Heat Transfer Navier-Stokes Solver. Theory and Applications*, Streamline Numerics, Inc. and Computational Thermo-Fluids Laboratory, Department of Mechanical and Aerospace Engineering Technical Report, Gainesville, Florida, 2002.

[96] Shyy, W., *Computational Modeling for Fluid Flow and Interfacial Transport*, Elsevier, Amsterdam, The Netherlands, 1994.

[97] Shyy, W., Thakur, S., and Wright, J., "Second-Order Upwind and Central Difference Schemes for Recirculating Flow Computation," *AIAA Journal*, Vol. 30, 1992, pp. 923–932.

[98] Rhie, C. L. and Chow, W. L., "A Numerical Study of the Turbulent Flow Past an Isolated Airfoil with Trailing Edge Separation," *AIAA Journal*, Vol. 21, 1983, pp. 1525–1532.

[99] Foust, M. J., Deshpande, M., Pal, S., Ni, T., Merkle, C. L., and Santoro, R. J., "Experimental and Analytical Characterization of a Shear Coaxial Combusting GO2/GH2 Flowfield," 34th AIAA Aerospace Sciences Meeting and Exhibit, Reno, NV, AIAA-96-0646, 1996.

[100] Venkateswaran, S., Weiss, J. M., Merkle, C. L., and Choi, Y.-H., "Propulsion-related Flowfields Using the Preconditioned Navier-Stokes Equations," 28th AIAA/ASME/SAE/ASEE Joint Propulsion Conference and Exhibit, Nashville, TN, AIAA-92-3437, 1992.

[101] Schley, C.-A., Hagemann, G., Tucker, K. P., Venkateswaran, S., and Merkle, C. L., "Comparison of Computational Codes for Modeling Hydrogen-Oxygen Injectors," 33rd AIAA/ASME/SAE/ASEE Joint Propulsion Conference and Exhibit, Seattle, WA, AIAA-1997-3302, 1997.

[102] Schley, C.-A., Hagemann, G., and Golovitchev, V., "Comparison of High Pressure H2/O2 Rocket Model Engine Reference Simulations," 31st AIAA/ASME/SAE/ASEE Joint Propulsion Conference and Exhibit, Monterey, CA, AIAA-95-2429, 1995.

[103] Chen, Y. S., "Compressible and Incompressible Flow Computations with a Pressure Based Method," 27th AIAA Aerospace Sciences Meeting and Exhibit, Reno, NV, AIAA-89-0286, 1989.

[104] Oefelein, J. C. and Yang, V., "Modeling High-pressure Mixing and Combustion Processes in Liquid Rocket Engines," *Journal of Propulsion and Power*, Vol. 14, No. 5, 1998.

[105] Mayer, W. and Tamura, H., "Propellant Injection in a Liquid Oxygen/Gaseous Hydrogen Rocket Engine," *Journal of Propulsion and Power*, Vol. 12, 1998, pp. 1137–1147.

[106] Ivancic, B. and Mayer, W., "Time- and Length Scales of Combustion in Liquid Rocket Thrust Chambers," *Journal of Propulsion and Power*, Vol. 18, No. 2, 2002.

[107] Lin, J., West, J. S., Williams, R. W., and Tucker, K. P., "CFD Code Validation of Wall Heat Fluxes for a GO2/GH2 Single Element Combustor," 41st AIAA/ASME/SAE/ASEE Joint Propulsion Conference and Exhibit, Tucson, AZ, AIAA-2005-4524, 2005.

[108] Marshall, W. M., Pal, S., Woodward, R. D., and Santoro, R., "Benchmark Wall Heat Flux Data for a GO2/GH2 Single Element Combustor," 41st AIAA/ASME/SAE/ASEE Joint Propulsion Conference and Exhibit, Tucson, AZ, AIAA-2005-3572, 2005.

[109] Oefelein, J. C., "Numerical Mixing and Combustion of Cryogenic Oxygen-Hydrogen Shear-coaxial Jet Flames at Supercritical Pressure," *Combust. Sci. and Tech.*, Vol. 178, 2006, pp. 229–252.

[110] Oschwald, M., Smith, J. J., Branam, R., Hussong, J., and Schik, A., "Injection of Fluids into Supercritical Environments," *Combust. Sci. and Tech.*, Vol. 177, 2005, pp. 2087–2138.

[111] Cheng, G. C. and Farmer, R., "Real Fluid Modeling of Multiphase Flows in Liquid Rocket Engine Combustors," *Journal of Propulsion and Power*, Vol. 22, No. 6, 2006.

[112] Vingert, L. and Habiballah, M., "Test Case RCM 2: Cryogenic Spray Combustion at 10 bar at Mascotte," *Proceedings of the 2nd International Workshop on Rocket Combustion Modeling, Deutsches Zentrum fur Luft-und Raumfahrt (DLR), Lampoldshausen, Germany*, 2001.

[113] Thomas, J. L. and Zurbach, S., "Test Case RCM 3: Supercritical Spray Combustion at 60 bar at Mascotte," *Proceedings of the 2nd International Workshop on Rocket Combustion Modeling, Deutsches Zentrum fur Luft-und Raumfahrt (DLR), Lampoldshausen, Germany*, 2001.

[114] Conley, A., Vaidyanathan, A., and Segal, C., "Heat Flux Measurements in a GH2/GO2 Single-element Injector," 42nd AIAA/ASME/SAE/ASEE Joint Propulsion Conference and Exhibit, Sacramento, CA, AIAA-2006-5048, 2006.

[115] Tucker, P. K., Menon, S., Merkle, C. L., Oefelein, J. C., and Yang, V., "Validation of High-fidelity CFD Simulations for Rocket Injector Design," 44th AIAA/ASME/SAE/ASEE Joint Propulsion Conference and Exhibit, Hartfrod, CT, AIAA-2008-5226, 2008.

[116] Pal, S., Marshall, W., Woodward, R., and Santoro, R., "Wall Heat Flux Measurements for a Uni-element GO2/GH2 Shear Coaxial Injector," Third International Workshop on Rocket Combustion Modeling, Paris, France, 2006.

[117] Vaidyanathan, A., Gustavson, J., and Segal, C., "Heat Fluxes/OH PLIF Measurements in a GO2/GH2 Single-element, Shear Injector," 43rd AIAA/ASME/SAE/ASEE Joint Propulsion Conference and Exhibit, Cincinnati, OH, AIAA-2007-5591, 2007.

[118] Evans, J. S. and Schexnayder, C. J., "Influence and Chemical Kinetics and Unmixedness on Burning in Supersonic Hydrogen Flames," *AIAA Journal*, Vol. 18, No. 2, 1980, pp. 188–193.

[119] Gontkovskaya, V. T., Gordopolova, I. S., and Ozerkovskaya, N. I., "Hydrogen Oxidation at Non-isothermal Conditions," *J. Phys. Combust. Explosions*, Vol. 28, No. 1, 1988.

[120] Ó Conaire, M., Curran, H. J., Simmie, J. M., Pitz, W. J., and Westbrook, C. K., "A Comprehensive Modeling Study of Hydrogen Oxidation," *International Journal of Chemical Kinetics*, Vol. 36, 2004, pp. 603–622.

[121] Barlow, R. S., Dibble, R. W., Chen, J.-Y., and Lucht, R. P., "Effect of the Damkohler Number on Super-equilibrium OH Concentration in Turbulent Nonpremixed Jet Flames," *Combustion and Flame*, Vol. 82, 1990, pp. 235–251.

[122] deRidder, M. A., Helderman, D. A., Nugent, N. J., and Anderson, W. E., "Measurement and Analysis of Heat Transfer in a Multi-Element Hydrogen/Oxygen Rocket Combustor," 44th AIAA/ASME/SAE/ASEE Joint Propulsion Conference & Exhibit, Hartford, CT, AIAA-2008-5031, 2008.

[123] deRidder, M. A., *Measurement and Analysis of Heat Transfer in a Multi-Element Hydrogen/Oxygen Rocket Combustor*, PhD., Purdue University, 2009.

[124] deRidder, M. A. and Anderson, W. E., "Heat Flux and Pressure Profiles in a Hydrogen /Oxygen Multielement Rocket Combustor," *To be published.*

[125] Box, G. E. P. and Wilson, K. B., "On the Experimental Attainment of Optimum Conditions," *Journal of the Royal Statistical Society, Series B (Methodological)*, Vol. 13, 1951, pp. 1–45.

[126] Matheron, G., "Principles of Geostatistics," *Economic Geology*, Vol. 58, 1963, pp. 1246–1266.

[127] Sutton, G. P., "History of Liquid Propellant Rocket Engines in the United States," *Journal of Propulsion and Power*, Vol. 19, No. 6, 2003, pp. 978–1007.

[128] Darcy, H., *Les Fontaines Publiques de la ville de Dijon*, Dalmont, Paris, 1856.

[129] Beavers, G. S. and Joseph, D. D., "Boundary Conditions at a Naturally Permeable Wall," *The Journal of Fluid Mechanics*, Vol. 30, 1967, pp. 197–207.

[130] Brinkman, H. C., "A Calculation of the Viscous Force Exerted by a Flowing Fluid on a Dense Swarm of Particles," *Applied Scientific Research*, 1947, pp. 27–34.

[131] Brinkman, H. C., "On the Permeability of Media Consisting of Closely Packed Porous Particles," *Applied Scientific Research*, 1948, pp. 81–86.

[132] Lundgren, T. S., "Slow Flow Through Stationary Random Beds and Suspension of Spheres," *The Journal of Fluid Mechanics*, Vol. 51, 1972, pp. 273–299.

[133] Rubinstein, J., "Effective Equations for Flow in Random Porous Media with a Large Number of Scales," *The Journal of Fluid Mechanics*, Vol. 170, 1982, pp. 379–383.

[134] Macdonald, I. F., El-Sayed, M. S., Mow, K., and Dullien, F. A. L., "Flow Through Porous Media-Ergun Equation Revisited," *Industrial and Engineering Chemistry Fundamentals*, Vol. 18, 1979, pp. 199–208.

[135] Forchheimer, P., "Wasserbewegung durch Boden," *Z Ver Deutsch Ing*, Vol. 45, 1901, pp. 1782–1788.

[136] Ward, J. C., "Turbulent Flow in Porous Media," *Journal of Hydraulic Division ASCE*, Vol. 90, 1964, pp. 1–12.

[137] Ergun, S., "Fluid Flow Through Packed Column," *Chemical Engineering Progress*, Vol. 48, 1952, pp. 89–94.

[138] Dullien, F. A. L., *Porous Media: Fluid Transport and Pore Structure*, Academic Press, New York, 1979.

[139] Sparrow, E. M. and Loeffler, A. L. J., "Longitudinal Laminar Flow Between Cylinders Arranged in Regular Array," *AIChE Journal*, Vol. 5, 1959, pp. 328–330.

[140] Happel, J. and Brenner, H., *Low Reynolds Number Hydrodynamics*, Martinus Nijhoff Publishers, Dordrecht, 1986.

[141] Carman, P. C., "The Determination of the Specific Surface Area of Powder I," *Journal of the Society of Chemical Industry*, Vol. 57, 1937, pp. 225–234.

[142] Kaviany, M., *Principles of Heat Transfer in Porous Media*, Springer-Verlag, New York, 1991.

[143] Nield, D. A. and Bejan, A., *Convection in Porous Media*, Springer-Verlag, New York, 1992.

[144] Slattery, J. C., "Single-phase Flow through Porous Media," *AIChE Journal*, Vol. 15, 1969, pp. 866–872.

[145] Slattery, J. C., *Momentum, Energy and Mass Transfer in Continua*, R. F. Krieger Publishing, Huntington, NY, 2nd ed., 1981.

[146] Whitaker, S., "Advances in Theory of Fluid Motion in Porous Media," *Ind. Eng. Chem.*, Vol. 61, 1969, pp. 14–28.

[147] Whitaker, S., "The Forchheimer Equation: A Theoretical Development," *Transport in Porous Media*, Vol. 25, 1996, pp. 27–61.

[148] Nozad, I., Carbonell, R. G., and Whitaker, S., "Heat Conduction in Multi-Phase Systems I: Theory and Experiments for Two-Phase Systems," *Chemical Engineering Science*, Vol. 40, 1985, pp. 843–855.

[149] Vafai, K. and Tien, C.-L., "Boundary and Inertia Effects on Flow and Heat Transfer in Porous Media," *International Journal of Heat and Mass Transfer*, Vol. 24, 1981, pp. 195–203.

[150] Cheng, P. and Minkowycz, W. J., "Free Convection About a Vertical Flat Plate Embedded in a Porous Medium with Application to Heat Transfer From a Dyke," *Journal of Geophysical Research*, Vol. 82, 1977, pp. 2040–2044.

[151] Cheng, P., "Combined Free and Forced Boundary Layer Flows About Inclined Surfaces in a Porous Medium," *International Journal of Heat and Mass Transfer*, Vol. 20, 1977, pp. 807–814.

[152] Bejan, A. and Poulikakos, D., "The Non-Darcy Regime for Vertical Boundary Layer Natural Convection in a Porous Medium," *International Journal of Heat and Mass Transfer*, Vol. 27, 1984, pp. 717–722.

[153] Liu, J. Y., Minkowycz, W. J., and Cheng, P., "Conjugated, Mixed Convection-Conduction Heat Transfer Along a Cylindrical Fin in a Porous Medium," *International Journal of Heat and Mass Transfer*, Vol. 29, 1986, pp. 769–775.

[154] Tully, L. R., Omar, A., Chung, J. N., and Carroll, B. F., "Fluid Flow and Heat Transfer in a Liquid Rocket Fuel Injector," 41st AIAA/ASME/SAE/ASEE Joint Propulsion Conference & Exhibit, AIAA-2005-4127, 2005.

[155] Lin, G. and Hu, J., Department of Mechanical Engineering, University of Michigan, Private Communication, 2007.

[156] Gray, W. G., "A Derivation of the Equations for Multiphase Transport," *Chemical Engineering Science*, Vol. 30, 1975, pp. 229–233.

[157] Amiri, A. and Vafai, K., "Analysis of Dispersion Effects and Non-Thermal Equilibrium, Non-Darcian, Variable Porosity Incompressible Flow Through Porous Media," *International Journal of Heat and Mass Transfer*, Vol. 37, 1994, pp. 939–954.